

Journal of Electrochemical Science and Engineering

J. Electrochem. Sci. Eng. 9(4) 2019, 223-323





Open Access: ISSN 1847-9286

www.jESE-online.org

Original scientific paper

Formation and reduction of anodic film on polycrystalline Bi electrode in pure methanol solutions

Anastos G. Anastopoulos[™] and Athanasios A. Papaderakis

Laboratory of Physical Chemistry, Department of Chemistry Aristotle University of Thessaloniki, 54124 Thessaloniki, Greece

Corresponding author: [™]anasto@chem.auth.gr

Received: April 2, 2019; Revised: May 4, 2019; Accepted: May 20, 2019

Abstract

The processes of film formation and reduction of bismuth in pure methanol are phenomenologically studied by means of cyclic voltammetry, ac voltammetry and electrochemical impedance spectroscopy methods. Film formation takes place under low electrode potentials within the potential range from -0.1 to about 0.2 V vs. Ag|AgCl resulting in the development of $Bi(CH_3O)_{ads}$ layer. The scan rate effect on the anodic current profile is interpreted in terms of a gradual variation of uncompensated resistance, accompanying the processes of film formation and reduction. Phase sensitive ac voltammetry measurements suggest leaky insulating character of a thin anodic film in agreement with the results of electrochemical impedance experiments.

Keywords

Anodic film formation; bismuth; methanol, methoxylation

Introduction

Electrochemical studies have confirmed that in pure methanol solutions methoxy anions, resulting from the solvent self-dissociation, interact with various electrode materials *viz*. Cu, Ni, Zn, Fe Ti, Si and the valve metal Al. This interaction leads to the formation of anodic surface films of the general type M-(CH₃O)_n, where M is the electrode material and n depends on the dissolution reaction of the electrode material and the specific reaction of film formation [1-3]. It is surprising that up to now, there is nothing reported in the literature about the electrochemical study of another valve metal Bi in pure methanol solutions. On the contrary, long-lasting systematic electrochemical research has been devoted to the system Bi/H₂O. In aqueous solutions, Bi₂O₃ is anodically formed on Bi surface by diffusion and field assisted migration of Bi³⁺ ions through the film under the influence of the so-called high field mechanism [4], resulting in both thickening and spreading of oxide islets. The cathodic reduction of Bi₂O₃ [5] involves development of a metallic Bi

film at the oxide/electrolyte interface, which is extended towards the interior of Bi_2O_3 layer. Two possible reduction mechanisms are usually suggested, the first involving electron transfer in the film and reduction at the film/solution interface and the second one, involving ion transfer in the film and reduction at the metal/film interface [6]. Bi_2O_3 oxide can be completely reduced by electrochemical means. Bi_2O_3 anodic oxide films present electrical rectification by acting as insulators under anodic potentials and conductors under cathodic ones, respectively [7,8]. Another important feature of Bi_2O_3 layers is their photoconductivity in the visible region. Bi_2O_3 layers present photocurrents of n- and p-type, thus being characterized as amphoteric semiconductors. The query as to whether Bi/CH_3OH system possesses similar or different properties than Bi/H_2O has motivated us to get involved in the present work.

Experimental

Electrodes and Chemicals

A polycrystalline Bi rod (Alfa Aesar, 99.99 %) embedded in a glass cylinder, sealed by suitable adhesive and covered with thermoplastic tube to leave a free disk shaped surface of 8 mm diameter at its end, was used as a working electrode. Pt foil auxiliary electrode and Ag|AgCl reference electrode saturated with aqueous KCl, both placed in a single compartment of double walled electrochemical cell kept at 298 K, were used in all measurements.

0.1 M LiClO₄ in methanol is used as the base solution in all measurements.

The working electrode was mechanically polished by emery paper of decreasing grain size. After that it was set for several minutes in an ultrasonic bath containing distilled water. Then it was washed with the working solution and transferred rapidly to the electrochemical cell.

The chemical reagents used without further purification are anhydrous LiClO₄ (Aldrich 99.99 %) and methanol (Lab-Scan, purity >99 %, maximum water content 0.05 %).

Methods and Instrumentation

Cyclic voltammetry and electrochemical impedance spectroscopy (EIS) measurements were carried out by Autolab PGSTAT302N electrochemical system connected to a PC running the Autolab software.

Bi electrode activation was proved necessary to improve the reproducibility of all electrochemical measurements. Therefore, Bi electrode was activated by cyclic voltammetry, scanning the potential from -1.6 to 0.2 V and back to -1.6 V vs. Ag | AgCl with a rate of 0.025 V s⁻¹. EIS measurements were carried out within the frequency range of 10 kHz to 0.1 Hz with 4 mV ac signal amplitude at selected dc potentials. The reproducibility of all electrochemical impedance measurements was checked by the comparison of three successive measurements at the same potential. The linearity-stability conditions for EIS measurements were checked by the Kramers-Kronig test incorporated in the AUTOLAB software. By this procedure, the sum of squares of differences (chi-square) between measured and calculated complex impedance values, i.e. real and imaginary impedance values were found to be of the order of 10⁻² in all systems studied within the frequency range from 10 kHz to 0.5 Hz. At frequencies below 0.5 Hz some EIS measurements were omitted because the corresponding chi-square values were found not better than 10⁻¹. Phase selective ac voltammetric measurements were carried out by an experimental setup [9] comprising a lock-in amplifier (model SR830 from Stanford Research) and a potentiostat (model Potentioscan Wenking POS73 from Bank Elektronik), interfaced to a PC running LabVIEW 6.1. Negative dc potential scan was applied in steps of 25 mV from 0.20 to -1.60 V vs. Ag AgCl. Each measurement was taken after 10 s of stopover at each potential. The amplitude and the frequency of the *ac* signal were set to 4 mV and 80 Hz respectively. The standard deviation between at least three successive measurements, expressed on a percent basis, was found equal to about 5 %.

Results and discussion

Cyclic voltammetry

The cyclic voltammetry response of a polycrystalline Bi electrode in pure methanol solution of 0.1M LiClO₄, obtained with an electrode potential scan rate ranging from 0.025 to 0.4 V/s is shown in Figure 1.

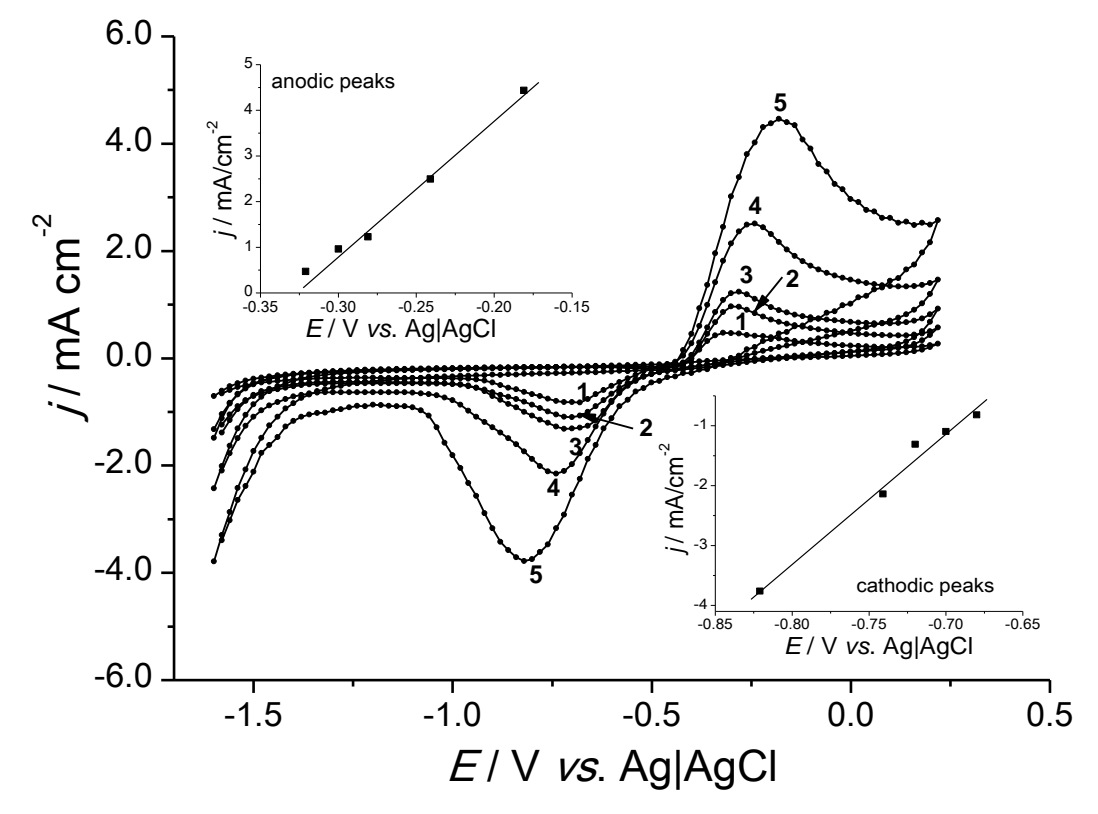


Figure 1. Cyclic voltammetry curves of Bi in methanol solution of 0.1 M LiClO₄ at various scan rates: (1) 0.025, (2) 0.05, (3) 0.10, (4) 0.20, (5) 0.40 V/s. Insets: Anodic and cathodic peak currents vs. corresponding peak current potentials.

During the anodic scan, the characteristic features of voltammetry curves are the following: At potentials positive to -0.40 V vs. Ag|AgCl, the anodic current increases leading to a single anodic current peak, which depending on the scan rate is located within the potential range (-0.25 \pm 0.07) V vs. Ag|AgCl. This peak marks the formation of initial nuclei of the anodic film. The absence of multiple anodic peaks indicates that successive layers are not developed. At potentials positive to the anodic peaks, the current vs. potential dependence presents a narrow and ill-defined plateau which tends to a new increase of anodic current at electrode potentials, $E \ge 0.20 \text{ V vs. Ag}|AgCl$. This current increase is presumed to be related to the methanol oxidation on Bi, the exact mechanism of which is neither known nor the subject of the present work. However, it can be reasonably assumed that $E \approx 0.20 \text{ V vs. Ag}|AgCl$ is the positive limit of anodic film formation in the neutral methanol solution of 0.1 M LiClO₄. During the cathodic scan, the characteristic features of voltammetric curves are the following: The single cathodic current peak observed at

(-0.75±0.07) V vs. Ag|AgCl is presumed to be related to the reduction process of the anodically developed film. At potentials negative to -1.40 V vs. Ag|AgCl, however, the hydrogen evolution manifests itself by increase of the cathodic current.

The observed single anodic and cathodic peaks suggest that formation and reduction processes of the anodic film in the case of the system Bi/CH₃OH represent one step reactions. At potentials from about -0.1 V to 0.2 V vs. Ag | AgCl, where ill-defined anodic plateau of the curves of Figure 1 is observed, anodic films of Bi in methanol are developed. Although the decomposition of methanol is a rather complicated process resulting in various ionic species of the general type CH_xO [1], the process of its self-dissociation can be simply described as:

$$2CH_3OH \leftrightarrow CH_3O^- + CH_3OH_2^+ \tag{1}$$

Combination with the simple picture of voltammetric curves of Figure 1, suggests that the process of anodic film formation of bismuth in pure methanol is presumably its surface methoxylation. At low positive and negative electrode potentials CH₃O⁻ ions are electrosorbed on the Bi surface, which undergoes a single step anodic dissolution, as deduced by the single anodic peak. Formation of Bi⁺ is, similarly to that suggested for Al [1], carried out according to the reaction:

$$Bi \rightarrow Bi^{+} + e$$
 (2)

Presumably, a thin film of the form Bi(CH₃O)_{ads} is developed on the bare metal Bi. Single anodic peaks also suggest that Bi⁺ is the final dissolution product and that further dissolution of bismuth is not detected in pure methanol. Therefore, the anodic film formation of Bi in pure methanol can be described by means of the following one-electron reaction [1]:

$$Bi^{+} + CH_{3}O^{-} \rightarrow Bi(CH_{3}O)_{ads} + e^{-}$$
(3)

Correspondingly, during the cathodic scan, the reduction of Bi(CH₃O)_{ads} film is reasonably expected to take place by means of the inverse reaction (3).

According to the literature [10-13], a mechanistic interpretation of the nucleation and thickening of anodic films can be formulated by means of the relation between the anodic current profile and the electrode potential scan rate. In Figure 1 we see that with increasing the scan rate, peak currents increase, and anodic peaks shift to more positive potentials, while cathodic peaks shift to more negative ones. Peak potential and peak current values are linearly dependent on the square root of the scan rate as indirectly indicated by linear j peak vs. E peak plots shown in the insets of Figure 1. Such linear dependencies involving peak currents and peak potentials were already reported [14] for Bi_2O_3 anodic film developed on Bi surface in aqueous solutions. The formation and reduction mechanisms of Bi_2O_3 include the occurrence of a solid state diffusion process [13,14] operating only in the case of thick films developed under high positive electrode potentials. This would not be the case for the thin anodic layer $Bi(CH_3O)_{ads}$ formed in pure methanol. In this case the linear dependence of E peak and j peak values on the square root of scan rate may be the result of a gradual variation of uncompensated resistance, accompanying the film formation and reduction according to the so called passivation model of Müller, where the process of film formation is under the control of ohmic resistance [10].

Phase selective ac voltammetry

Information about the structural characteristics of an electrochemical interface can be also acquired from differential capacitance measurements.

However, over the whole potential range studied from 0.2 to -1.6 V vs. Ag|AgCl, the interface between the polycrystalline Bi electrode and methanol solution may be not identified with the

model of ideal capacitor, because at the extremes of this range Bi/methanol interface is not ideally polarizable. It must also be indicatively recalled that capacitance studies of single crystal Bi electrodes in LiClO₄ containing methanol solution performed by Estonian electrochemists [15], were carried out at electrode potentials ranging from -0.4 to -1.4 V vs. SCE leaving outside the potentials where film formation and hydrogen evolution occur. In this respect, it is useful to look at the structural characteristics of Bi/CH₃OH interface by means of the phase selective ac voltammetry technique in terms of the potential dependence of the out of phase ac current, j_{90} , decoupled from the in phase j_0 component. j_{90} vs. E curves are typically free from faradaic contributions and describe the potential dependence of the resident interfacial charge, providing thus a picture of the structural condition of the interface. In Figure 2, j_{90} vs. E dependence clearly shows potential regions where the anodic film is present and those where it is absent.

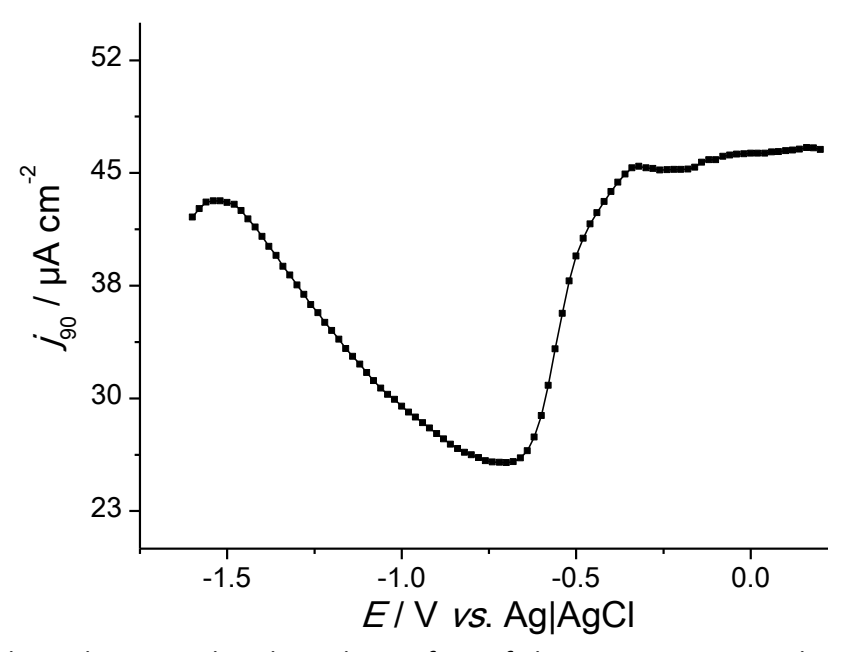


Figure 2. Electrode potential, E, dependence of out of phase current, j_{90} , at polycrystalline Bi electrode in 0.1 M LiClO₄ methanolic solution.

At potentials positive to -0.50 V vs. Ag|AgCl where the anodic film is present, j_{90} values show a weak potential dependence. According to the literature [16], potential independent capacitance may be expected for insulating films having thicknesses of about $(1.5\pm0.5)x10^{-7}$ cm. Thus, the weak potential dependence of j_{90} current values shown in Figure 2 may be considered as an indication for the presence of a leaky insulating film prior than passive or semiconductive layer of oxide nature.

The minimum of j_{90} vs. E curve in Figure 2 falls into the same potential range as cathodic peaks of cyclic voltammetric curves shown in Figure 1. Therefore, it may be assumed that the potential dependence of j_{90} from about -0.50 V to -0.85 V vs. Ag|AgCl represents a transition from the Bi(CH₃O)_{ads} covered electrode to the bare metal Bi.

Electrochemical impedance spectroscopy

The elucidation of processes involved in the formation and reduction of Bi(CH₃O)_{ads} surface film can be further assisted by electrochemical impedance measurements, carried out at selected electrode potentials. As shown in Figure 3, all Nyquist plots obtained at the vicinity of the anodic and cathodic peaks *i.e.* at -0.4 V and -0.68 V and also at -1.4 V vs. Ag | AgCl where hydrogen evolution is presumed, exhibit the form of flattened semicircles.

-Z'' vs. Z' plots of Figure 3 can be approximated by the Randles circuit of the type $R_s(R_{ct}Q_{dl})$ according to the circuit description code of Boukamp [17]. This circuit incorporates solution and charge transfer resistances (R_s and R_{ct}) and the parameter Q_{dl} of the constant phase element which resembles the contribution of double layer capacitance to the overall impedance.

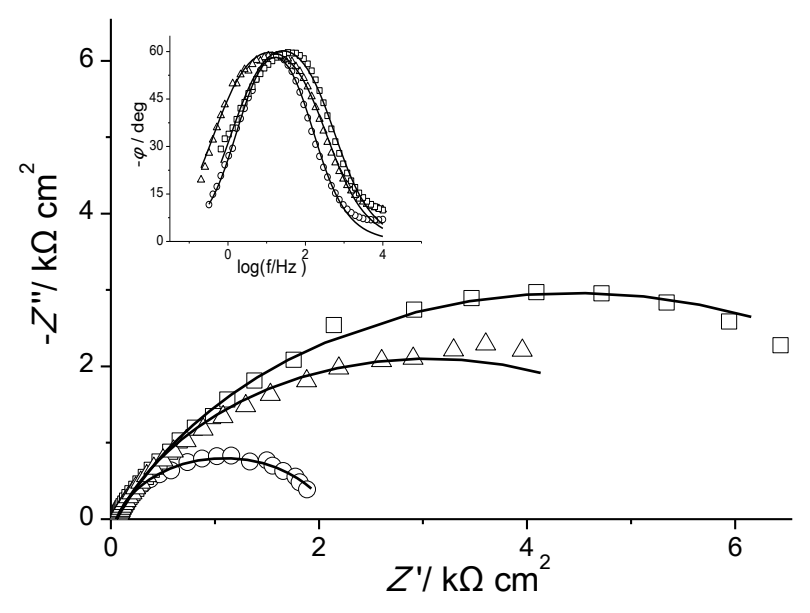


Figure 3. Nyquist plots of Bi in methanol solution of 0.1 M LiClO₄, at various electrode potentials in V vs. Ag|AgCl: \triangle -0.4, \square -0.68, \bigcirc -1.4. Inset: Bode phase diagrams at the same potentials. Lines represent simulated responses fitted to experimental points.

The corresponding Bode phase diagrams shown in the inset of Figure 3 clearly show a single *RC* time constant, with phase angles hardly approaching -60°. This is characteristic of a significant deviation from pure capacitive behavior, thus justifying the use of constant phase element instead of conventional capacitor. The results of circuit fitting to -Z" vs. Z" data of Figure 3 are provided in Table 1.

Table 1. Results of CNLS fitting of circuit $R_s(R_{ct} Q_{dl})$ to -Z" vs Z' data

E / V vs. Ag AgCl	R_s/Ω cm ²	$R_{\rm ct}$ / $k\Omega$ cm ²	$Q_{\rm dl}$ / Ω^{-1} cm ⁻² s ⁿ	n	χ^2	-
-0.40	55.5	8.8	0.54 10 ⁻⁴	0.75	0.085	
-0.68	52.9	6.0	0.35 10 ⁻⁴	0.78	0.072	
-1.40	54.7	2.1	0.63 10 ⁻⁴	0.83	0.067	

The calculated values of R_s and Q_{dl} are weakly dependent on electrode potential. The decrease of R_{ct} with increasing negative potential from -0.40 to -0.68 V vs. Ag|AgCl denotes the acceleration of the inversed reaction (3). This is not the case of the even lower value of R_{ct} at -1.4 V vs. Ag|AgCl because at this potential the more probable reaction is hydrogen evolution. The values of CPE exponent, n, point up to the significant deviation from the model of ideal capacitance.

The validity of R(RQ) circuit suggests the occurrence of reactions with a single electron transfer step as reaction (3) and its reverse.

Within the potential range -0.1 V to 0.2 V vs. Ag|AgCl, where the anodic film Bi(CH₃O)_{ads} is present, Nyquist plots obtained at various electrode potentials do not show noticeable features.

However, at these potentials Bode phase diagrams shown by the inset of Figure 4 reveal two partially overlapping time constants. This is the most clearly seen in the Bode plot measured at $E = 0.15 \text{ V } vs. \text{ Ag} \mid \text{AgCl}$, showing a deep at the frequency of 6.87 Hz.

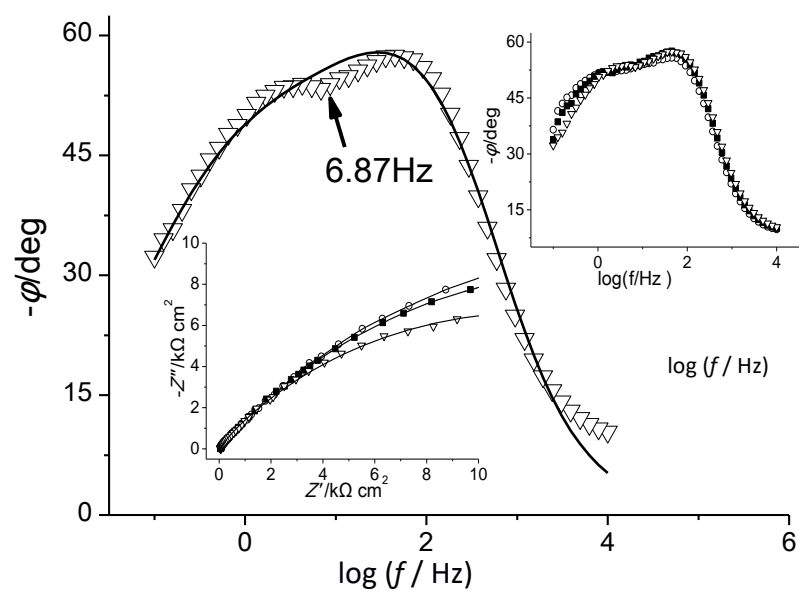


Figure 4. Bode phase diagram of Bi in methanol solution of 0.1 M LiClO₄, at E = 0.15 V vs. Ag/AgCl. Insets: Nyquist and Bode plots at potentials $\circ - 0.05$, $\blacksquare - 0.10$ and $\nabla - 0.15 \text{ V}$. Lines are fitting results of R(Q[R(RQ)]) equivalent circuit to experimental points.

Among several equivalent circuits already used for the EIS study of anodic oxides, the circuit $R_s(Q_{dl}[R_{ct}(R_{ad}\ Q_{ad})])$ shown in Figure 5, which has been suggested for the description of charge transfer process in the presence of adsorbed species [18], was applied.

The results obtained after fitting the circuit in Figure 5 to experimental impedance plots in Figure 4, are presented in Table 2.

Table 2. Results of CNLS fitting of circuit $R_s(Q_{dl}[R_{ct}(R_{ad} Q_{ad})])$ to -Z" vs. Z' data

E / V vs. Ag AgCl	$R_{\rm s}/\Omega{\rm cm}^2$	$R_{\rm ct}$ / $k\Omega$ cm ²	$Q_{\rm dl}$ / Ω^{-1} cm ⁻² s ⁿ	$R_{\rm ad}$ / $k\Omega$ cm ²	$Q_{\rm ad}$ / Ω^{-1} cm ⁻² s ⁿ	n_{dl}	n_{ad}	χ^2
-0.05	52.3	5.9	0.93 10 ⁻⁴	28.6	0.86 10-4	0.78	0.62	0.081
-0.10	52.5	7.4	0.67 10 ⁻⁴	23.8	0.61 10-4	0.890	0.75	0.088
-0.15	53.2	5.6	0.65 10-4	18.9	0.49 10-4	0.79	0.74	0.090

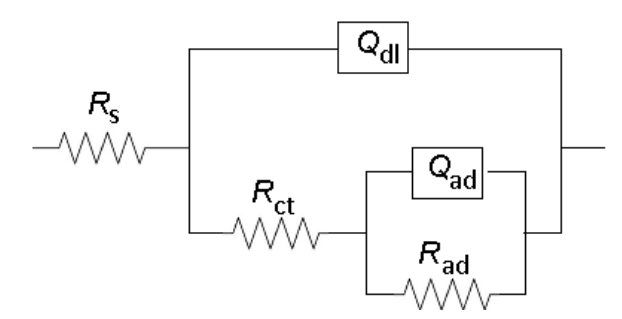


Figure 5. Electrical equivalent circuit used to fit impedance spectrum at potentials: 0.05, 0.10 and 0.15 V vs. Ag/AgCl. R_S = solution resistance, R_{ct} = charge transfer resistance, R_{ad} = anodic film resistance. Q_{ad} and Q_{dl} are parameters of constant phase elements corresponding to the anodic film $Bi(CH_3O)_{ads}$ and Bi/solution interface.

In view of the Bode plots of Figure 4 and the circuit of Figure 5, one of the two time constants may be related to the presence of $Bi(CH_3O)_{ads}$ film by means of anodic film resistance and the other to the electron transfer associated with reactions (2) and (3) by means of charge transfer resistance. The results of Table 2 reveal a high value of film resistance R_{ad} in agreement with the predicted leaky insulating character of the $Bi(CH_3O)_{ads}$ layer. As expected, R_{ct} values are lower and of similar

magnitude with those of Table 1. The values of CPE exponents, n_{dl} and n_{ad} again point up to the significant deviation of both capacitor responses from that of ideal capacitance.

Conclusions

The process of anodic film formation of bismuth in pure methanol is identified with its surface methoxylation. A single step dissolution of Bi surface to Bi⁺ is suggested. Voltammetric results suggest that anodic film formation takes place within a narrow zone of low electrode potentials ranging from -0.1 V to 0.2 V vs. Ag|AgCl, by adsorption of -CH₃O⁻ groups, resulting in Bi(CH₃O)_{ads} film. Weak potential dependence of the out of phase *ac* current within the above potential range suggests that this film is of leaky insulating character, which is also confirmed by the relatively high value of film resistance resulting from circuit fitting to EIS measurements.

References

- [1] J. Banas, B. Stypula, K. Banas, J. Światowska-Mrowiecka, M. Starowicz, U. Lelek-Borkowska, *Journal of Solid State Electrochemistry* **13** (2009) 1669-1679.
- [2] J. Światowska-Mrowiecka, J. Banas, Electrochimica Acta 50 (2005) 1829-1840.
- [3] A. Papaderakis, A.G. Anastopoulos, S. Sotiropoulos, *Journal of Electroanalytical Chemistry* **783** (2016) 217-225.
- [4] J. W. Schultze, M. M. Lohrengel, *Electrochimica Acta* **45** (2000) 2499-2513.
- [5] D. E. Williams, G. A. Wright, *Electrochimica Acta* **22** (1977) 505-508.
- [6] B. V. Tilak, R. S. Perkins, H. A. Kozlowska, B.E.Conway, Electrochimica Acta 17 (1972) 1447-1469.
- [7] M. Metikoš-Huković, Electrochimica Acta 26 (1981) 989-1000.
- [8] M. Metikoš-Huković, Z. Grubac, The Journal of Physical Chemistry B 102 (1998) 7406-7412.
- [9] A. Bozatzidis, A.G. Anastopoulos, T. Laopoulos, *Electroanalysis* **19** (2007) 1711-1718.
- [10] A. J. Calandra, N. R. de Tacconi, R. Pereiro, A.J. Arvia, *Electrochimica Acta* 19 (1974) 901-905.
- [11] S. Kapusta, N. Hackerman, *Electrochimica Acta* **25** (1980) 949-955.
- [12] M. Šeruga, M. Metikoš-Huković, Journal of Electroanalytical Chemistry **334** (1992) 223-240.
- [13] Z. Grubač, M. Metikoš-Huković, *Electrochimica Acta* **43** (1998) 3175-3181.
- [14] D. E. Williams, G. A. Wright, *Electrochimica Acta* **21** (1976) 1009-1019.
- [15] K. Lust, M. Väärtnõu, E. Lust, Electrochimica Acta 45 (2000) 3543-3554.
- [16] U. Stimming, J. W. Schultze, *Berichte der Bunsengesellschaft für physikalische Chemie* **80** (1976) 1297-1302
- [17] B. A. Boukamp, *Solid State Ionics* **18-19** (1986) 136-140.
- [18] A. Lasia, *Electrochemical Impedance Spectroscopy and its Applications*, Springer, New York, USA, 2014.

©2019 by the authors; licensee IAPC, Zagreb, Croatia. This article is an open-access article distributed under the terms and conditions of the Creative Commons Attribution license (http://creativecommons.org/licenses/by/4.0/)



Open Access: ISSN 1847-9286

www.jESE-online.org

Original scientific paper

Simultaneous determination of trace levels of Cd(II) and Pb(II) in tap water samples by anodic stripping voltammetry with 2-mercaptobenzothiazole modified electrode

Sophy Phlay¹, Weena Aemaeg Tapachai², Supunnee Duangthong¹, Puchong Worattananurak¹ and Pipat Chooto^{1,⊠}

¹Analytical Chemistry Division, Department of Chemistry, Faculty of Science, Prince of Songkla University, Hatyai, Songkhla, 90112, Thailand

²Inorganic Chemistry Division, Department of Chemistry, Faculty of Science, Prince of Songkla University, Hatyai, Songkhla, 90112, Thailand

Corresponding author: [™]pipat.c@psu.ac.th

Received: December 12, 2018; Revised: May 7, 2019; Accepted: May 9, 2019

Abstract

Glassy carbon electrode (GCE) modified by 2-mercaptobenzothiazole (MBT), mesoporous silica (Meso) and bismuth was developed to determine Cd(II) and Pb(II) simultaneously by square wave anodic stripping voltammetry (SWASV). In-situ preparation was found to work best in optimum conditions of acetate buffer pH 6, accumulation potential of -1.1 V, deposition time of 300 s and scan rate of 200 mV/s. SW peaks revealed the linear range of 5-50 µg/L Cd(II) and 5-50 µg/L Pb(II). LOD and LOQ for Cd(II) and Pb(II) were determined as 0.56, 0.80, 1.87 and 2.66 µg/L, respectively. The interaction of metals with bismuth and MBT, as well as higher surface area due to mesoporous silica, support beneficial performance of the modified electrode. Insignificant interferences from other regularly present metal ions were found. With SRM1640 standard, the SWASV results are found comparable to those obtained by inductive coupled plasma optical emission spectrometry (ICP-OES). The method was used to analyze the metals in tap water by standard addition method with the satisfactory recovery of 100.7 % for Cd(II) and 100.8 % for Pb(II).

Keywords

Modified electrodes; 2-mercaptobenzothiazole; Square wave anodic stripping voltammetry

Introduction

Among heavy metals with high potential in contamination of water for daily consumptions are Cd(II) and Pb(II). At present, the contamination problems from both metals are still found in a number of areas all over the world. The main source of Cd(II) is from discarded batteries, whereas

Pb(II) can contaminate water *via* dyes, paints, pipes and solders. It has been known that these metals can occur together and cause more damage especially to the brain [1,2]. The limits set by USEPA are 0.005 mg/L for Cd(II) and 0.015 mg/L for Pb(II) [3]. The techniques which are cost-effective, fast, simple and sensitive are therefore required in testing water samples. Even though there are a number of possibilities, a reference technique that can be applied for simultaneous determination of Pb(II) and Cd(II) in problematic areas around the world is still a matter of challenge. Traditional methods with high sensitivity have usually been used in laboratory conditions for the detection of Pb(II) and Cd(II), such as UV–vis spectrophotometry [4], fluorescence method [5], ion-selective electrode [6], graphite furnace atomic absorption spectrometry [7], atomic emission spectroscopy [8,9] and inductively coupled plasma mass spectrometry [10]. However, these techniques have the drawbacks of being time-consuming, complex, expensive and not suitable for onsite analysis.

With electrode modification by organic compounds, polymers and nanomaterials, electrochemical methods, especially anodic stripping voltammetry (ASV), can provide some advantages including speed, accuracy, sensitivity, selectivity, reproducibility and stability [11]. Boron doped diamond electrode (BDD) [12] was found to work well with Pb(II) and its modification with 4aminomethyl benzoic acid provided figures of merits for Cd(II) analysis [13]. For simultaneous determination of Cd(II) and Pb(II), the most widely investigated is the use of bismuth which forms alloys with both metals [14,15]. Satisfactory LOD values were especially obtained when Bi was coupled with various materials such as carbon nanotubes in order to facilitate formation of larger surface areas. A variety of compounds such as graphene [16], Co₃O₄ [17], polymers [18,19] and crown ether [20,21] were also found to be successful in pre-concentrating both metal ions. Organic ligands with electron rich atoms including phytic acid oxygen [22,23], phenolic oxygen and nitrogen [24], cysteine sulfur [25,26] and lysine nitrogen [27] were found to implement better analytical performances for simultaneous determination of Cd(II) and Pb(II). MBT is an alternative ligand containing nitrogen and sulfur [28] which was used in the extraction of both metals before analysis by flame atomic absorption spectroscopy (FAAS) [29], as a biosensor for pesticides [30] and in forming polymeric structure to accommodate more complexing sites [31].

This paper reports an investigation of using MBT modified electrode for the first time to analyze Pb(II) and Cd(II) simultaneously by an ASV technique. The method is optimized, verified and then applied to the real samples.

EXPERIMENTAL

Reagents and samples

All reagents were used as received without any further treatment. Cd(II) and Pb(II) standards were prepared in-house from their nitrate salts as an atomic spectroscopy standard solution. Tetrabutylammonium hexafluorophosphate with the purity of ≥ 98.0 % and bismuth (III) nitrate pentahydrate were obtained from Fluka, whereas 2-mercaptobenzothiazole and mesoporous silica were from Sigma-Aldrich. Other reagents and metal salts for interference studies were of the highest purity commercially available. All subsequent solutions were prepared with deionized water (resistivity not less than 18 M Ω cm, ELGA water purification system, England) and purged by nitrogen gas (99.99 %) for 2 min before use. Laboratory glassware was cleaned with 10 % (v/v) nitric acid solution and then rinsed with deionized water. Cd(II) and Pb(II) standard solutions were prepared by diluting the respective stock solutions with the high purity deionized water and stored in polyethylene bottles before use.

NIST (National Institute of Standards and Technology) SRM 1640 composed of natural fresh water from Clear Creek, Colorado USA, was used as a reference with the certified value of 22.79 \pm 0.96 μ g/L Cd(II) and 27.89 \pm 0.14 μ g/L Pb(II).

Tap water samples were collected in different spots within the city of Hatyai, Songkhla, Thailand, digested by mixing the aliquot of 500 mL with 2 mL of concentrated HNO_3 and 2 mL of KNO_3 , put in cleaned polyethylene bottles and kept at 4 °C before analysis.

Instrumentation

A PowerLab 2/20 with Potentiostat (ADInstrument, Australia) and EChem software was used for cyclic voltammetry (CV) and square wave anodic stripping voltammetry (SWASV), whereas Metrohm AUTOLAB PGSTAT 302N with NOVA software was used for EIS measurements. An Ag/AgCl, 3 M KCl reference electrode (Metrohm), a platinum counter electrode (Metrohm) and a modified glassy carbon electrode (Windsor Scientific Ltd., UK) with an inner diameter of 3 mm put in 50 mL cell were used for electrochemical measurements. All voltages were reported versus Ag/AgCl reference electrode. pH was measured by pH meter Model 510 (Eutech Instruments, USA) and inductively coupled plasma optical emission spectrometer (ICP-OES) Optima 4300 DV (Perkin-Elmer, USA) was used for the comparison of methods.

Preparation of modified electrode and starting procedure

The modified electrodes with different compositions and different orders of mixing were tested to select the one with the best sensitivity enhancement. Differential pulse (DP) and square wave (SW) results, as well as electrodes modified by in-situ and ex-situ Bi deposition were also compared. The following starting procedure was designed for further optimization:

Three electrodes were put in 50 mL cell containing 50 mL of 0.1 M acetate buffer pH 6. Then, 0.1 μ g/L Cd(II) and Pb(II), 200 μ g/L Bi(III), 1000 mg/L Meso and 1000 mg/L MBT were added into solution. The metals were then deposited under the initial conditions of -1.4 V for 300 s with stirring. After the equilibration time of 30 s, SWASV potential was scanned from -1.0 to -0.2 V with the scan rate of 250 mV/s, frequency of 50 Hz, amplitude of 75 mV and potential step of 160 mV to obtain the stripping current signals for analysis. Optimization was conducted by varying a number of parameters (*vide infra*) for the best analytical performance to be used in real sample analysis.

Results and discussion

Electrode modification and voltammograms of Cd(II) and Pb(II)

A number of modification experiments has been conducted to figure out the most suitable materials and methods. Ex-situ Bi deposition was found to result in a lower current value and unsymmetrical peak shape. As shown in Figure 1, the best sensitivity was obtained for in-situ modified GCE in the order of Bi + Meso + MBT. The results reflect the role of Meso in increasing surface areas and sites, and role of Bi and MBT in alloy forming and complexation, respectively. Within the potential range of -1.0 to -0.2 V applied after the starting procedure, two well defined stripping peaks at Bi + Meso + MBT modified electrode were observed at -0.72 V for Cd(II) and -0.58 V for Pb(II), and the enhancement of stripping currents can be clearly seen for both metal ions. This kind of electrode modification was therefore used for further optimization, verification and analysis.

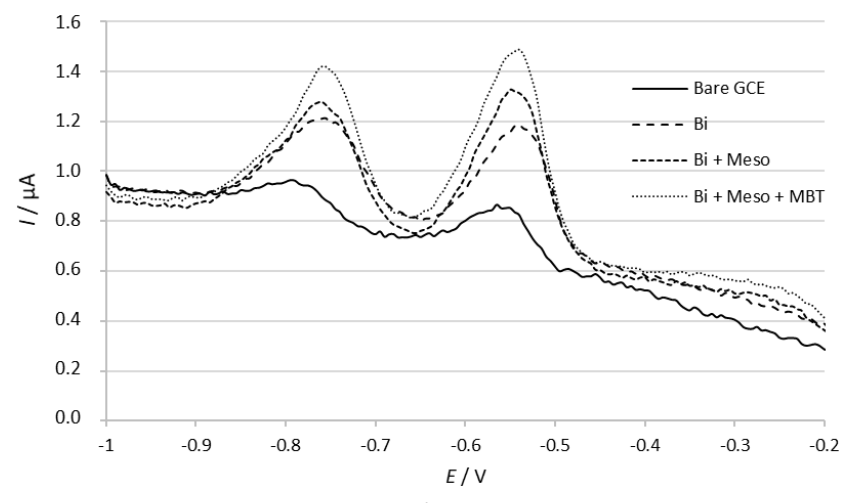


Figure 1. Comparison of stripping currents of 0.1 mg/L Cd(II) and Pb(II) at differently modified electrodes in conditions of 0.1 M acetate buffer pH 6, deposition potential -1.4 V, deposition time 300 s, equilibration time 30 s and concentrations of Meso 1000 mg/L, MBT 1000 mg/L and Bi 0.2 mg/L.

CV and EIS for electrode characterizations

Figure 2 shows the cyclic voltammetry (CV) results of differently modified GCEs in acetate buffer solution containing $Ru(NH_3)6^{3+}$ (a) and $Fe(CN)6^{4-}$ (b). It is clear that each modification step of GCE supports the electron transfer well for both inner and outer spheres by maintaining reversibility and increasing the current.

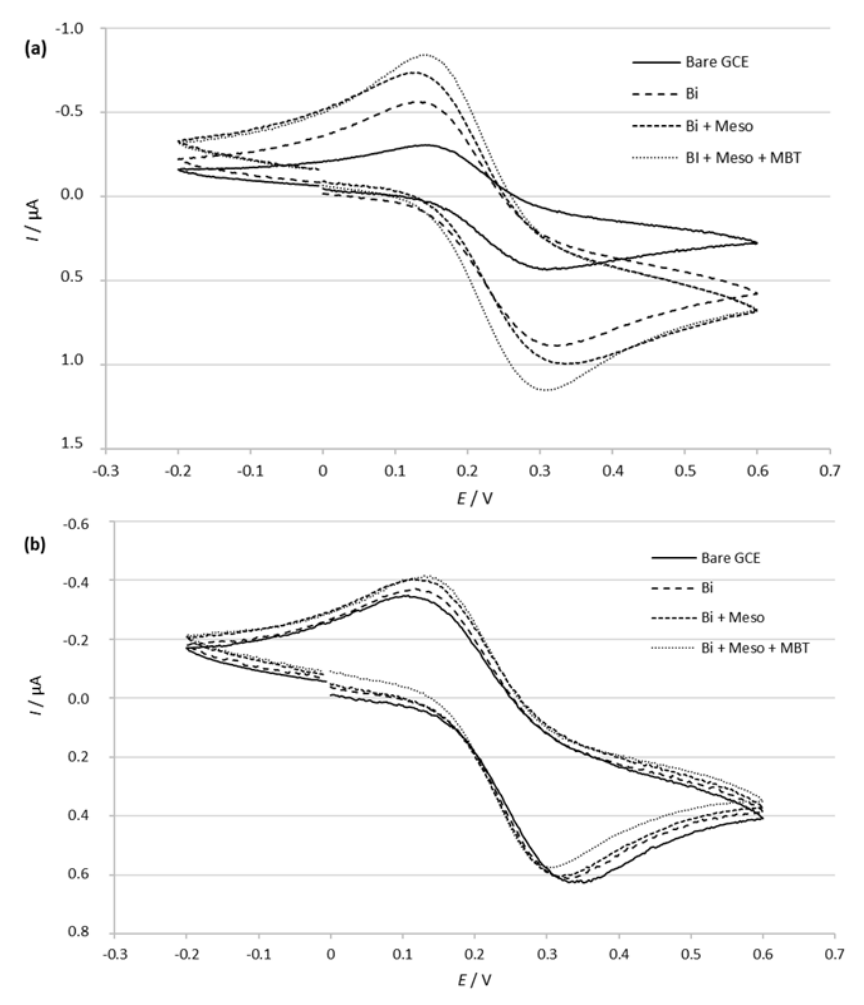


Figure 2. Cyclic voltammetry for bare GCE, Bi/GCE, Meso-Bi/GCE and Bi-Meso-MBT/GCE, with scan rate 100 mV/s in 0.1 M acetate buffer containing 2.5 mM Ru(NH₃) $_6^{3+}$ (a) and Fe(CN) $_6^{4-}$ (b).

The electron transfer capacities of modified electrodes were characterized by electrochemical impedance spectroscopy (EIS). Less curvature in an impedance spectrum is well known to represent less resistance to electron transfer. Therefore, Figure 3 reveals that addition of each modifying agent facilitates the electron transfer exhibiting less resistance, and the effect is highest after addition of MBT.

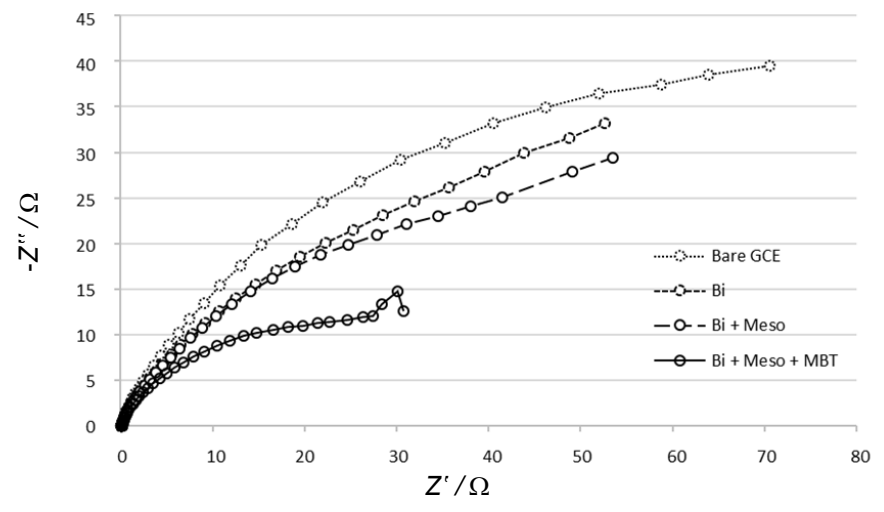


Figure 3. Impedance spectra of the bare GCE, Bi/GCE, Bi-Meso/GCE, Bi-Meso-MBT/GCE.

Optimization

Comparison of SWASV and DPASV

SWASV and DPASV parameters are summarized in Table 1. Comparison of corresponding stripping currents is presented in Figure 4, showing higher current enhancement in the case of SWASV. Hence, SWASV technique is selected for the following experiments.

Parameter	SWASV	DPASV
Accumulation step		
Deposition potential	-1000 mV	-1000 mV
Deposition time	400 s	800 s
Equilibration time	30 s	30 s
Measuring Step		
Frequency	50 Hz	-
Step potential	160 mV	100 mV
Amplitude	75 mV	75 mV

Table 1. SWASV and DPASV parameters

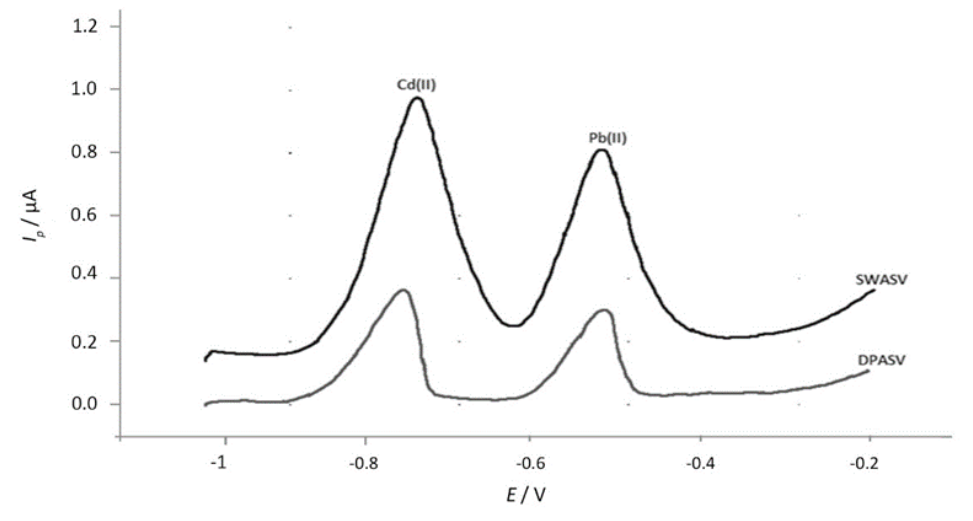


Figure 4. Comparison of stripping currents of 0.1 mg/L Cd(II) and Pb(II) from SWASV and DPASV.

Effect of pH

Within the experimental pH range of 1 to 7, the maximum peak current for both metals was obtained at pH 6 as shown in Figure 5(a) and this value was used for the next investigations. pH 6 is suitable for the formation of sulfide anions of MBT to form complexes with metal ions corresponding with pKa of 6.93 [32]. If pH is lower than 6, protonation causes the formation of sulfhydryl groups which make complex formation more difficult. At pH higher than 6, the metals are probably susceptible to form hydroxides.

Deposition potential

The influence of deposition potentials was investigated over the potential range of -0.1 to -1.5 V. As shown in Figure 5(b), the current firstly increased steeply up to -1.1 V and then became almost constant. This is due to the greater extent of metal accumulation until the potential was high enough for deposition of both metals. Beyond -1.4 V, the current started to drop, possibly because greater thickness slows down the mass transfer and higher negative potential is susceptible to side reactions. The highest current for both metals is found at -1.1 V which was fixed for metal electrodeposition for the following study.

Deposition time

The deposition time was varied from 100 to 500 s. As shown in Figure 5(c), the current values gradually increased with time up to 300 s because greater accumulation of bismuth facilitated formation of alloys until surface saturation was reached. However, the current dropped before it went up again, reflecting that certain time is needed for alloy rearrangement. The highest peak current was found at 300 s and this was used for further optimizations and applications.

Effect of Bi concentration

The concentration of Bi was varied from 100 to 500 μ g/L. Figure 5(d) reveals firstly a normal trend of increasing current which is due to the increase of film thickness and then the current decreased because greater thickness can inhibit the mass transfer during the stripping step [33]. The concentration of 200 μ g/L provided the greatest peak current for both metals and was therefore selected for the following experiments.

Effect of Meso concentration

As shown in Figure 5(e), similar trend is obtained when Meso concentrations were changed from 100 to 600 μ g/L. Similar to previous explanation of the effect of Bi concentration, the excess of Meso can result in less current due to the obstruction of mass transfer. The concentration of 300 μ g/L showing the greatest current was chosen for further investigations.

Effect of MBT concentration

As shown in Figure 5(f), within the studied range of 100 to 600 μ g/L, the stripping current increased with MBT concentration up to 100 μ g/L and then decreased for both metals. This is due to the fact that high concentration of MBT could block the mass transfer of metal ions at electrodeposition sites. The MBT concentration of 200 μ g/L was therefore selected for further experiments.

Scan rate

The stripping scan rate was changed from 50 to 300 mV/s. The stripping peak height was found to increase with the scan rate from 50 to 250 mV/s as shown in Figure 6. Under the criteria of peak shapes, 250 mV/s is chosen for the further study.

For equilibration time, step potential and pulse amplitude, the optimization value based on the greater current was selected.

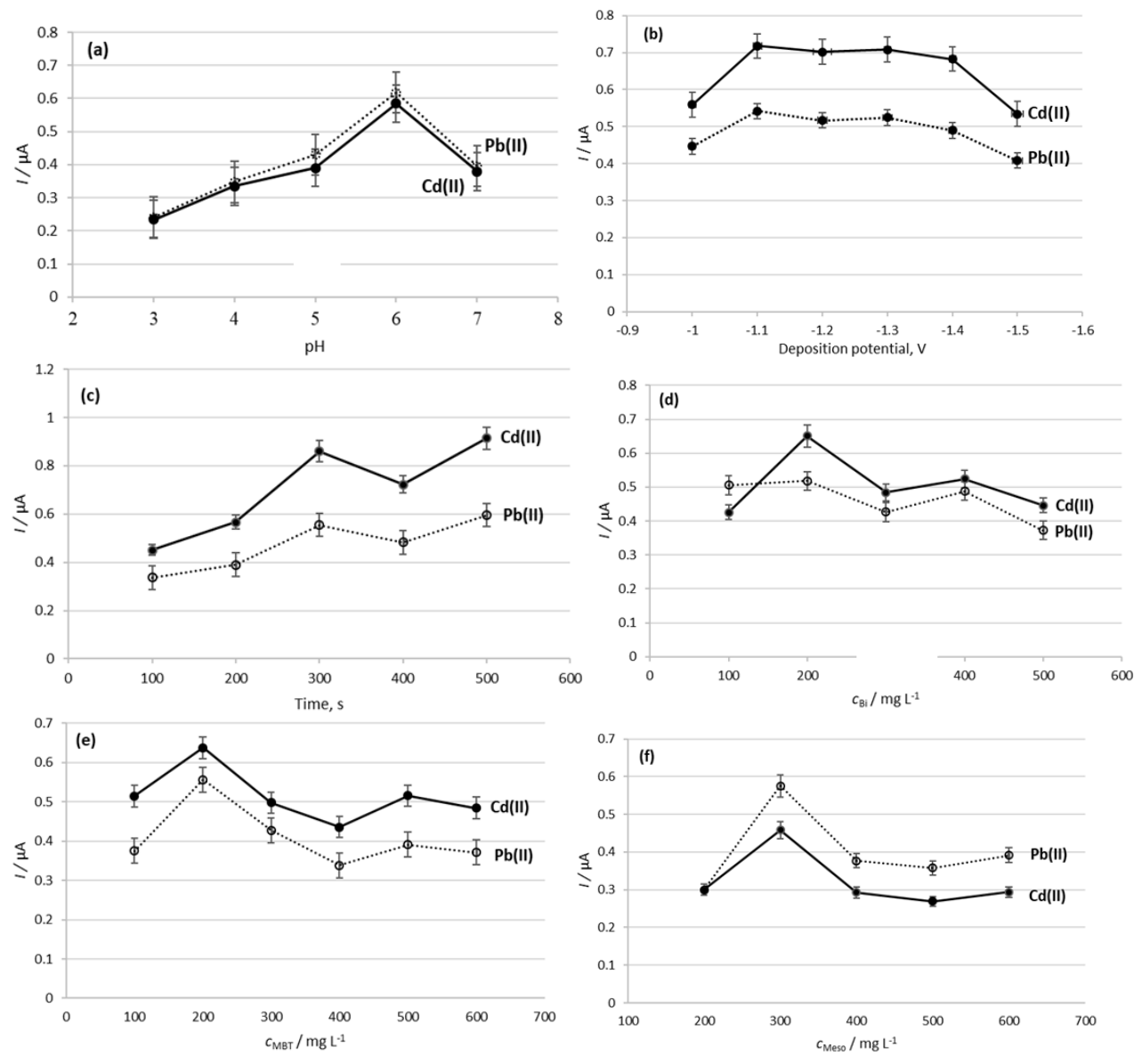


Figure 5. Effects of pH (a), deposition potential (b), deposition time (c), Bi concentration (d), Meso concentration (e) and MBT concentration (f) on stripping peak currents of 20 μ g/L Cd(II) and Pb(II).

All aforementioned optimized parameters are summarized in Table 2 and used in further experiments.

Table 2. Summary of optimized operating conditions

Parameter	Studied Range	Optimum Value
Deposition potential, V	-0.1 – -1.5	-1.1
Deposition time, s	100 – 500	300
рН	3 – 7	6
Bi concentration, μg/L	100 – 500	200
MBT concentration, μg/L	100 – 600	200
Meso concentration, μg/L	100 – 600	300
Equilibration time, s	10 – 50	30
Step potential, mV	1 – 20	5
Pulse amplitude, mV	25 – 80	75
Scan rate, mV / s	50 – 300	250

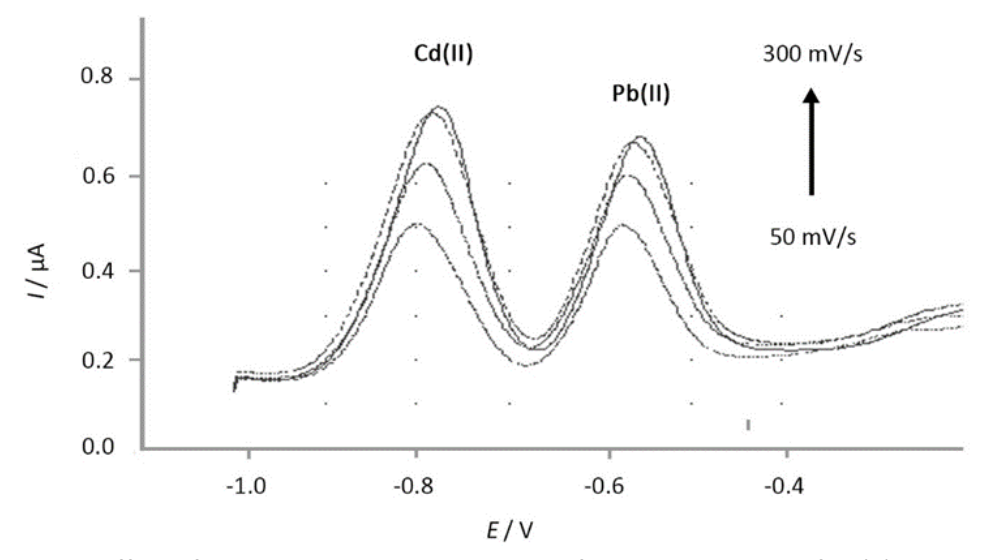


Figure 6. Effect of scan rate on stripping currents for concentrations of Pb(II) and Cd(II) 0.1 mg/L, Bi 200 μ g/L, MBT 200 μ g/L, Meso 300 μ g/L.

Analytical performance

SWASV was used for simultaneous determination of Cd(II) and Pb(II) with the modified electrode Bi-Meso-MBT/GCE performed under optimized conditions to obtain current signals. The results for certain typical concentrations of Cd(II) and Pb(II) are shown in Figure 7 and the corresponding calibration curves are presented in Figure 8. The linearity in the range of 5-50 μ g/L is observed for both metals with the correlation coefficient of 0.9978 for Cd(II) and 0.9960 for Pb(II), respectively. The linear regression equations of i_p = 0.0142x + 0.0372 (i_p : μ A, x: μ g/L) for Cd(II) and i_p = 0.0113x - 0.0699 for Pb(II) are defined. The limits of detection are found to be 0.56 μ g/L for Cd(II) and 0.80 μ g/L for Pb(II) by 3N/m, where N is the standard deviation of replicate (n=10) responses of 5 μ g/L of both metals taken as blank and m is the slope of the calibration curve. The limits of quantification, LOQ, defined as 10 N/m, are determined as 1.87 μ g/L for Cd(II) and 1.66 μ g/L for Pb(II). The relative standard deviations were 2.97 % for Cd(II) and 2.04 % for Pb(II) with repetitive determinations (n=10) of 20.0 μ g/L. All prove that the proposed method is satisfactorily reproducible and reliable for simultaneous determination of Cd(II) and Pb(II) at trace level and can be applied to real samples.

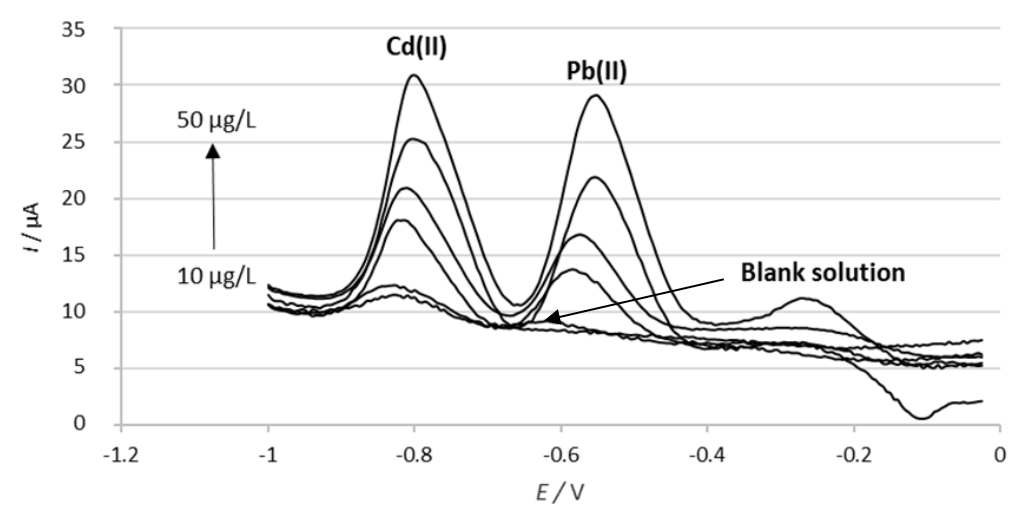


Figure 7. Typical SWASV voltammograms of water samples after spiking with 5 (as a blank) to 50 μg/L of both Cd(II) and Pb(II) standard solutions. Conditions: accumulation potential -1.1 V, accumulation time 300 s, acetate buffer solution pH 6, and scan rate 250 mV/s.

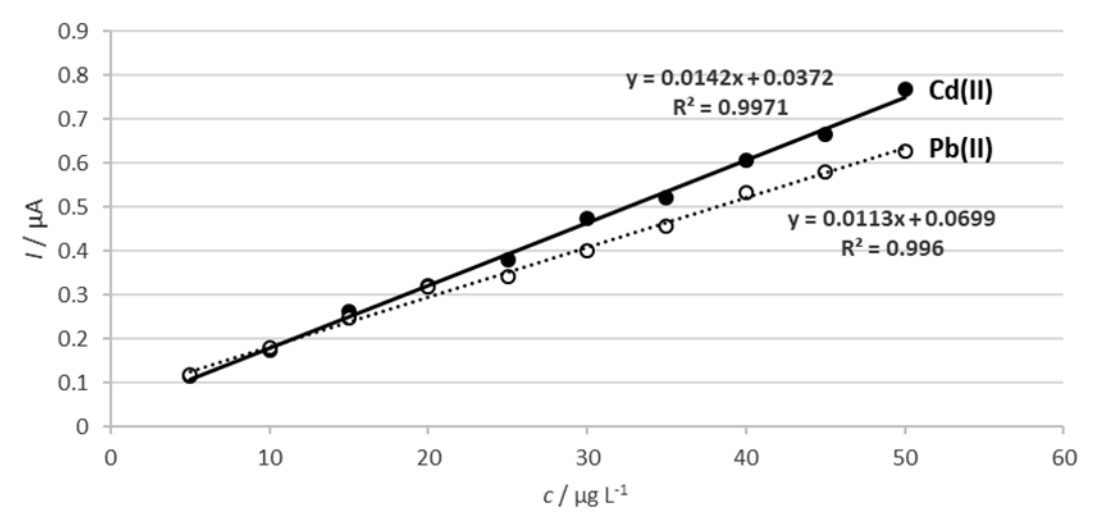


Figure 8. Calibration curves for Cd(II) and Pb(II) obtained by the proposed method.

Effect of other ions

Due to the capability of MBT to coordinate with a number of metal ions, the level of interference both from each other and other metal ions was investigated by the developed method under optimized conditions and the results are shown in Table 3. With the increase of Pb(II) concentration, no significant interference was observed for Cd(II) peak current. Other ions including Ca(II), Mg(II), Zn(II), Mn(II), Fe(II), Cu(II) and Al(III) at 1000 μ g/L were found to provide not high contributions for both metals. The most interfering ions here if present at high concentration are Cu(II) and Co(II) which normally can be masked by using a suitable and effective complexing agent such as ferrocyanide before analysis.

Table 3. Interference study of the stripping current measurements of 20 μ g/L Cd(II) and Pb(II) at Bi/Meso-MBT/GCE in the absence and presence of interfering metal ions

Interference	Contribution, $%^a(I_p(Cd(II)) = 100 \%)$	Contribution, $%^a(I_p(Pb(II)) = 100 \%)$
Cu(II)	-47.17	-21.78
Zn(II)	-16.68	-13.44
Mg(II)	37.49	14.98
Ca(II)	0.48	-3.68
Al(III)	2.34	-7.63
Mn(II)	13.36	0.65
Co(II)	-34.68	-40.14
Fe(III)	5.29	7.51
Ni(II)	-4.37	-5.87

^aContribution = [(I_p with interferent - I_p without interferent) / I_p without interferent] \times 100

Certified reference material determination, method comparison and real sample analysis

The proposed method was applied to a certified reference material, natural water SRM 1640 from the National Institute of Standards and Technology (NIST), USA. As shown in Table 4, satisfactory recoveries, of 98.02 % for Cd(II) and 97.74 % for Pb(II) were obtained.

The proposed method was then used in the analysis of Cd(II) and Pb(II) in tap water samples collected from 11 sites in Hatyai city. Typical results of 5th and 6th regions are compared with ICP-OES results and summarized in Table 5, reflecting good agreement between here proposed and standard methods.

Table 4. Recovery of Cd(II) and Pb(II) for certified reference material determination

	Erro	or 0/	Posov	(or) (0/			
Certified		ed Determined ^a		EIIC	or, %	Recov	ery, %
Cd(II)	Pb(II)	Cd(II)	Pb(II)	Cd(II)	Pb(II)	Cd(II)	Pb(II)
22.79±0.96	27.89±0.14	22.34±0.010 (RSD = 2.97 %)	27.26±0.005 (RSD = 2.04 %)	1.97	2.25	98.02	97.74

^a Mean \pm Standard deviation (n = 5)

Table 5. Determination of Cd(II) and Pb(II) in tap water samples (n = 4)

Sample	Concentration of spiked	Concentration from the proposed method, µg/L ^b		Recovery, %		Concentration from ICP-OES, μg/L ^b		Difference, %d	
	solution, μg/L	Cd(II)	Pb(II)	Cd(II)	Pb(II)	Cd(II)	Pb(II)	Cd(II)	Pb(II)
	0	ND^c	ND	-	-	ND	ND	ND	ND
Tan	5	5.11±0.003	5.12±0.005	-	-	5.10±0.1	5.30±0.12	1.00	3.45
Tap Water 5ª	10	10.19±0.010	10.20±0.007	100.8	100.8	10.15±0.12	10.50±0.20	0.4	2.9
water 5	20	20.40±0.012	20.35±0.010	101.4	101.1	20.35±0.021	20.50±0.25	0.25	0.7
	30	30.50±0.022	30.47±0.016	101.3	101.2	30.40±0.023	30.60±0.19	0.33	0.42
	0	ND	ND	-	-	ND	ND	ND	ND
Tan	5	5.16±0.004	5.15±0.006	-	-	5.10±0.02	5.03±0.400	1.17	2.36
Tap Water 6 ^a -	10	10.23±0.006	10.22±0.01	100.7	100.7	10.11±0.100	10.5±0.120	1.18	2.70
	20	20.36±0.012	20.33±0.01	101	100.9	20.01±0.002	20.04±0.05	0.15	0.14
	30	30.5±0.012	30.40±0.01	101.1	100.8	30.40±0.020	30.20±0.06	0.32	0.66

^aWater sample from 5^{th} and 6^{th} regions were selected for standard addition test; ^bMean \pm Standard deviation (n = 4); ^cNot detected; ^dDifference of the concentration from the proposed method and that from ICP-OES

For real sample analysis with water from the 1st, 5th and 6th regions used as typical samples, the recoveries values were found to be 100.7-101.4 % for Cd(II) and 100.8-101.2 % for Pb(II) as shown in Table 6.

Table 6. Recovery test for the proposed method using tap water samples (n = 3)

Sample	Concentration of spiked solution, μg/L	Concentration	Concentration found, μg/L		
		Cd(II)	Pb(II)	Cd(II)	Pb(II)
	0	ND	ND	-	-
Tap water	5	5.15±0.07	5.19±0.067	-	-
1 st region	10	10.23±0.002	10.25±0.008	100.8	100.6
	20	20.31±0.015	20.27±0.011	100.8	100.4
_	30	30.35±0.011	30.36±0.015	100.4	100.5
	0	ND	ND	-	-
Tanwatar	5	5.11±0.003	5.12±0.005	-	-
Tap water - 5 th region -	10	10.19±0.01	10.20±0.007	100.8	100.8
5 region -	20	20.40±0.012	20.35±0.010	101.4	101.1
_	30	30.50±0.022	30.47±0.016	101.3	101.2
	0	ND	ND	-	-
Tantustan	5	5.16±0.004	5.15±0.006	-	-
Tap water - 6 th region -	10	10.23±0.006	10.22±0.01	100.7	100.7
o region -	20	20.36±0.012	20.33±0.01	101.0	100.9
-	30	30.50±0.012	30.40±0.01	101.1	100.8

Mean \pm S.D. (n = 3); ND: Not detected

As shown in Table 7, the results obtained with here proposed method are comparable with the results obtained by other anodic stripping voltammetric based methods. It is clear, however, that



here proposed method has the advantage of wider linear range, lower detection limits and greater simplicity. The only disadvantage could be a little longer deposition time, which can be adjusted according to the required accuracy. Other very recent methods without using bismuth are also included (Entry 1-6) as references to show that here proposed method is reasonably satisfactory.

Table 7. Comparison of the proposed method for determination of Cd(II) and Pb(II) in water sample with other recent anodic stripping voltammetric methods

Entry	Electrodes	Method	Deposition	Linear range of concentration, µg/L		LOD, μg/L		Ref
			time, s	Cd(II)	Pb(II)	Cd(II)	Pb(II)	-
1	HMgFe-EDG/G	SWASV	180	11.2 – 207	11.2 – 207	1.22	0.304	[34]
2	ST PANI NTs	SWASV	600	0.207 - 24.84	1.12 - 19.04	0.02	0.03	[35]
3	CA/RGO/GCE	SWASV	1500	0.0207 - 2.07	0.112 - 13.44	0.004	0.002	[36]
4	Nafion/CLS/PGR/GCE	SWASV	140	10.35 – 1035	5.60 – 560	2.06	0.336	[37]
5	GO/k-Car/L-Cys/GCE	SWASV	120	1.03 – 10.35	0.56 - 5.60	0.12	0.12	[38]
6	NCQDs-GO	DPASV	300	10.35 – 20.7	0.112 - 11200	1.16	7.4	[39]
7	In situ Bi/Graphite/Epoxy	SWASV	120	41.4 – 352	56 – 280	14.5	5.60	[40]
8	Bi-Meso-MBT/GCE	SWASV	300	5 - 50	5 – 50	0.56	0.80	This work

HMgFe-EDH/G: Hierarchical MgFe-layered double hydroxide microsphere graphene composite

ST PANI NTs: Size-tunable polyaniline nanotube-modified electrode CA/RGO/GCE: calixarene functionalized reduced graphene oxide

CLS/PGR: calcium lignosulphonate functionalized porous graphene nanocomposite

GO/ κ -Car/L-Cys/GCE: graphene oxide κ -carrageenan L-cysteine nanocomposite NCQDs-GO: N-doped carbon quantum dots graphene oxide hybrid in situ Bi/Graphite/Epoxy: in situ bismuth film on graphite dispersed in epoxy resin

Bi-Meso-MBT/GCE: Bismuth mesoporous silica 2-mercaptobenzothiazole modified GCE

Conclusions

GCE was modified with Bi, Meso and MBT and applied to simultaneous determination of Cd(II) and Pb(II) in trace levels, using square wave anodic stripping voltammetry (SWASV). The method provides satisfactory advantages of speed, simplicity, sensitivity and selectivity. Good recoveries of Cd(II) (100.7 %) and Pb(II) (100.8 %) were obtained for the real sample, along with LOD of 0.56 μ g/L for Cd(II) and 0.80 μ g/L for Pb(II), respectively. The method can be used satisfactorily for the analysis of tap water in local areas and the results were found in good agreement with those obtained by ICP-OES.

References

- [1] V. Karri, M. Schuhmacher, V. Kumar, *Environmental Toxicology and Pharmacology* **48 (**2015) 203-213.
- [2] C. Yvonne H, M. P. Wilkie, *Aquatic Toxicology* **161** (2015) 176-188.
- [3] United States Environmental Protection Agency, http://water.epa.gov/drink/contaminants/index/cfm (13th September 2017)
- [4] Q. Hu, G. Yang, Y. Zhao, J. Yin, Analytical and Bioanalytical Chemistry 375 (2003) 831-835.
- [5] S. Xu, S. Xu, Y. Zhu, W. Xu, P. Zhou, C. Zhou, B. Dong, H. Song, *Nanoscale* **6** (2014) 12573-12579.
- [6] M. Fouskaki, N. A. Chaniotakis, *Analytical Chemistry* 77 (2005) 1780-1784.
- [7] R. Liu, P. Liang, *Journal of Hazardous Materials* **152** (2008) 166–171.
- [8] G. Abbasse, B. Ouddane and J. C. Fischer, *Journal of Analytical Atomic Spectrometry* **17** (2002) 1354-1358.
- [9] N. Pourreza, S. Rastegarzadeh, A. Larki, *Journal of Industrial and Engineering Chemistry* **20** (2014) 2680-2686.

- [10] D. V. Biller, K. W. Bruland, *Marine Chemistry* **130-131** (2012) 12-20.
- [11] P. Chooto, Modified electrodes for determining trace metal ions. In: Application of the Voltammetry. M. Stoytcheva, R. Zlatev, Ed(s)., Intech, Rijeka, Croatia: InTech; 2017 p. 129
- [12] P. Chooto, P. Wararatananurak, C. Innuphat, ScienceAsia 36 (2010) 150-156.
- [13] C. Innuphat, P. Chooto, *ScienceAsia* **43** (2017) 33-41.
- [14] S. Cerovac, V. Guzsvány, Z. Kónya, A. M. Ashrafi, I. Švancara, S. Rončević, Á. Kukovecz, B. Dalmacija, K. Vytřas, *Talanta* **134** (2015) 640-649.
- [15] D. Li, J. Jia, J. Wang, Talanta 83 (2010) 332-336.
- [16] L. Xiao, B. Wang, L. Ji, F. Wang, Q. Yuan, G. Hu, A. Dong, W. Gan, *Electrochimica Acta* **222** (2016) 1371-1377.
- [17] Y. Zuo, J. Xu, F. Jiang, X. Duan, L. Lu, H. Xing, T. Yang, Y. Zhang, G. Ye, Y. Yu, *Journal of Electroanalytical Chemistry* **801** (2017) 146-152.
- [18] M. Arab Chamjangali, H. Kouhestani, F. Masdarolomoor, H. Daneshinejad, *Sensors and Actuators B Chemical* **216** (2015) 384-393.
- [19] Y. Wu, N. B. Li, H. Q. Luo, Sensors and Actuators B **133** (2008) 677-681.
- [20] K. Keawkim, S. Chuanuwatanakul, O. Chailapakul, S. Motomizu, Food Control 31 (2013) 14-21.
- [21] N. Serrano, A. G. Calabuig, M. del Valle, *Talanta* **138** (2015) 130-137.
- [22] H. Dai, N. Wang, D. Wang, H. Ma, M. Lin, *Chemical Engineering Journal* **299** (2016) 150-155.
- [23] S. Kheirandish, M. Ghaedi, K. Dashtian, R. Jannesar, M. Montazerozohori, F. Pourebrahim, M. A. Zare, *Journal of Colloid and Interface Science* **500** (2017) 241-252.
- [24] L. Zhu, L. Xu, B. Huang, N. Jia, L. Tan, S. Yao, Electrochimica Acta 115 (2014) 471-477.
- [25] J. P. Llovera, C. P. Ràfols, N. Serrano, J. M. Díaz-Cruz, C. Ariño, M. Esteban, *Talanta* **175** (2017) 501-506.
- [26] Z. Guo, D. Li, X. Luo, Y. Li, Q. N. Zhao, M. Li, Y. Zhao, T. Sun, Chi Ma, *Journal of Colloid and Interface Science* **490** (2017) 11-22.
- [27] I.P. Khullar, U. Agarwala, Canadian Journal of Chemistry 53 (1975) 1165-1171.
- [28] Ş. Tokalıoğlu, A. Papak, Ş. Kartal, Arabian Journal of Chemistry 10 (2017) 19-23.
- [29] V. S. Somerset, M. J. Klink, M. M. C. Sekota, P. G. L. Baker, E. I. Iwuoha, *Analytical Letters* **39** (2006) 1683-1698.
- [30] M. d. F. B. Sousa, E. J. Dallan, S. B. Yamaki, R. Bertazzoli, *Electroanalysis* 9 (1997) 614-618.
- [31] H. Huang, W. Zhu, X. Gao, X. Liu, H. Ma, Analytica Chimica Acta 947 (2016) 32-41.
- [32] <u>Chemicalland21.com</u>, <u>http://chemicalland21.com/specialtychem/perchem/2-MERCAPTOBENZOTHIAZOLE.htm</u> (29th May 2018)
- [33] L. Cao, J. Jia, Z. Wong, *Electrochimica Acta* **53** (2008) 2177-2182.
- [34] Y. Ma, Y. Wang, D. Xie, Y. Gu, X. Zhu, H. Zhang, G. Wang, Y. Zhang, H. Zhao, *Chemical Engineering Journal* **347** (2018) 953-962.
- [35] G. Zhu, Y. Ge, Y. Dai, X. Shang, J. Yang, J. Liu, *Electrochimica Acta* **268** (2018) 202-210.
- [36] C. Göde, M. L.i Yol, A. Yılmaz, N. Atar, S. Wang, *Journal of Colloid and Interface Science* **508** (2017) 525-531
- [37] L. Yu, Q. Zhang, B. Yang, Q. Xu, Q. Xu, X. Hu, Sensors and Actuators B 259 (2018) 540-551.
- [38] T. Priya, N. Dhanalakshmi, S. Thennarasu, N. Thinakaran, *Carbohydrate Polymers* **182** (2018) 199-206
- [39] L. Li, D. Liu, A. Shi, T. You, Sensors and Actuators B **255** (2018) 1762-1770.
- [40] K. Pokpas, S. Zbeda, N. Jahed, N. Mohamed, P. G. Baker, E. I. Iwuoha, *International Journal of Electrochemical Science* **9** (2014) 736-759.

©2019 by the authors; licensee IAPC, Zagreb, Croatia. This article is an open-access article distributed under the terms and conditions of the Creative Commons Attribution license (http://creativecommons.org/licenses/by/4.0/)





Open Access: ISSN 1847-9286

www.jESE-online.org

Original scientific paper

Sol-gel synthesis and electrochemical performance of NiCo₂O₄ nanoparticles for supercapacitor applications

Yong Zhang^{1,2,⊠}, Yi Ru¹, Hai-Li Gao^{1,}, Shi-Wen Wang¹, Ji Yan¹, Ke-Zheng Gao¹, Xiao-Dong Jia¹, He-Wei Luo¹, Hua Fang¹, Ai-Qin Zhang¹ and Li-Zhen Wang¹

¹Department of Material and Chemical Engineering, Zhengzhou University of Light Industry, Zhengzhou 450002, P.R. China

²Henan Provincial Key Laboratory of Surface & Interface Science, Zhengzhou University of Light Industry, Zhengzhou 450002, P.R. China

Corresponding authors: [™]zy@zzuli.edu.cn; [™]gaohaili@zzuli.edu.cn

Received: April 4, 2019; Revised: June 7, 2019; Accepted: June 8, 2019

Abstract

In this work, NiCo₂O₄ nanoparticles with enhanced supercapacitive performance have been successfully synthesized via a facile sol-gel method and subsequent calcination in air. The morphology and composition of as-prepared samples were characterized using scanning electron microscopy (SEM), transmission electron microscope (TEM), X-ray diffraction (XRD), and Raman spectroscopy (Raman). The electrochemical performances of NiCo₂O₄ nanoparticles as supercapacitor electrode materials were evaluated by cyclic voltammetry (CV), galvanostatic charge/discharge (GCD) tests in 3 mol L-1 KOH aqueous solution. The results show that as-prepared NiCo₂O₄ nanoparticles have diameters of about 20-30 nm with uniform distribution. There are some interspaces between nanoparticles observed, which could increase the effective contact area with the electrolyte and provide fast path for the insertion and extraction of electrolyte ions. The electrochemical tests show that the prepared NiCo₂O₄ nanoparticles for supercapacitors exhibit excellent electrochemical performance with high specific capacitance and good cycle stability. The specific capacitance of NiCo₂O₄ electrode has been found as high as 1080, 800, 651, and 574 F g⁻¹ at current densities of 1, 4, 7, and 10 A g^{-1} , respectively. Notably, the capacitance retention rate (compared with 1 A q^{-1}) is up to 74.1 %, 60.3 %, and 53.1 % at current densities of 4, 7, and 10 A g⁻¹, respectively. After 100 cycles, higher capacitance retention rate is also achieved. Therefore, the results indicate that NiCo₂O₄ material is the potential electrode material for supercapacitors.

Keywords

Supercapacitors, sol-gel method, NiCo₂O₄, nanoparticles, electrochemical performances

Introduction

Due to the rapid growth of global economy, depletion of fossil fuels and increasing environmental pollution, the search for "green" and renewable energy resources is one of the most urgent challenges facing us today. As one of the most promising energy storage devices, supercapacitors, also known as electrochemical capacitors or capacitors, are widely used in emergency power systems, hybrid electric vehicles, consumer electronics, industrial power systems, smart grids, aerospace, *etc.* This is due to their superior performances, such as high power density, nearly infinite cycle life, wide temperature range and high coulomb efficiency [1]. According to different storage mechanisms, supercapacitors are divided into two types [2]: electric double-layer capacitors (EDLCs) based on charge storage mechanisms at the electrode/electrolyte interface, and pseudocapacitors based on additional reversible redox reaction(s) of electrode materials. The electroactive materials of EDLCs are usually carbon-based materials [3] (such as activated carbon (AC), carbon nanotubes, carbon aerogels (CA), graphene, *etc.*), while the electrode materials of pseudocapacitors are mainly transition metal oxides and conductive polymers (such as RuO₂ [4], NiO [5], Co₃O₄ [6], MnO₂ [7], CeO_x [8], NiCo₂O₄ [9], Pr₆O₁₁@Ni-Co [10], NiMoO₄ [11], polyaniline [12], polypyrrole [13], *etc.*).

Pseudocapacitors can provide much higher specific capacitance than EDLCs by using reversible Faraday reactions on the electrode surface. Supercapacitor devices are composed of four parts: electrode materials (positive and negative), electrolyte, separator and shell, among which electrode materials play the key role in their performance. Unfortunately, the defects of electrode materials, such as low specific capacitance of carbon-based materials, poor electrochemical stability of conductive polymers, and poor electronic conductivity of transition metal oxides, seriously impede practical applications of supercapacitors [14]. Among pseudocapacitive materials, RuO₂, having specific capacity as high as 1580 F g⁻¹ [15], is the most prominent electrode material for application in supercapacitors. However, the high cost and environmental toxicity hinder its extensive commercial application. Therefore, great efforts have been devoted to search cheap alternative materials with good capacitive characteristics similar to RuO₂, and especially those electrode materials with multiple oxidation states and high electronic conductivity.

In recent years, binary metal oxide/hydroxides have shown much better electronic conductivity and higher electrochemical activity than single component oxides/hydroxides [16], making them one of the most promising electrode materials for supercapacitors. As one of the binary metal oxides, NiCo₂O₄ is generally considered as a mixed valence oxide with pure spinel structure, in which nickel occupies octahedral sites and cobalt distributes in octahedral and tetrahedral sites [17]. The solid phase redox couples of Ni²⁺/Ni³⁺ and Co²⁺/Co³⁺ in this structure, present better electrocatalytic activity than single NiO and Co₃O₄, the conductivity that is at least twice higher than for NiO and Co₃O₄, and capacitive performance comparable with the noble metal oxide RuO₂. Therefore, NiCo₂O₄ has attracted considerable attention in energy conversion/storage systems due to its excellent electrochemical properties, rich redox reactions involving different ions, complex chemical components and synergistic effects. Hence, NiCo₂O₄ with ultra-high specific capacitance could be an alternative pseudocapacitive material to RuO₂. Currently, the spinel NiCo₂O₄ has been widely used in supercapacitors and lithium ion batteries, as electrocatalysts and magnetic materials, in photodetectors, ferrofluid technology, *etc.*[14,18].

Based on the pseudocapacitor mechanism, a golden way to improve the redox kinetics is to create nanostructured electrode materials with large surface area for redox reaction and short transport paths for ions and electrons. Therefore, the development of polymetallic oxide supercapacitor materials with special micro-nano structure and morphology is of great practical

significance and challenge. Thus far, various $NiCo_2O_4$ materials with different morphologies and nanostructures, such as nanowires [19], nanorods [20], urchin-like hollow microspheres [21], nanotubes [22], nanoneedles [23], nanosheets [24], *etc.*, have been synthesized by various methods, including the sol-gel method [25], coprecipitation method [26], electrodeposition method [27], microwave method [28], and hydrothermal method [29]. In recent years, the ultracapacitors of $NiCo_2O_4$ have been studied [17,30]. However, due to the high calcination temperature, high crystallinity and low electrochemical activity, the specific capacitance of $NiCo_2O_4$ is low. Therefore, the development of pure $NiCo_2O_4$ by sol-gel technology is considered as a simple, cheap and low energy consumption method for the preparation of mixed metal oxides, which can produce homogeneous multi-component metal oxide materials with high purity, small grain size, large specific surface area, and good electrical conductivity.

In this work, we demonstrate use of a simple sol-gel method followed by calcination at moderate temperature of 350 °C, to prepare NiCo₂O₄ nanoparticles with unique characteristics. Some techniques such as scanning electron microscopy (SEM), X-ray diffraction (XRD), Raman spectroscopy (Raman), cyclic voltammetry (CV), and galvanostatic charge/discharge (GCD) methods were used to characterize the samples. The results show that the as-synthesized NiCo₂O₄ nanoparticles exhibit high specific capacitance, superior high-rate capability and long-life cycling stability. This is due to its small particle size, low crystallinity and high active materials utilization. Moreover, NiCo₂O₄ material benefits from multiple oxidation states/structures which contribute by both nickel and cobalt ions. These results indicate that the as-prepared NiCo₂O₄ nanoparticles have the potential application in development of high performance supercapacitors.

Experimental

Synthesis of NiCo₂O₄ nanoparticles

All reagents were of analytical level and used without further purification. Figure 1 presents the schematic diagram of the fabrication process of NiCo₂O₄ nanoparticles.

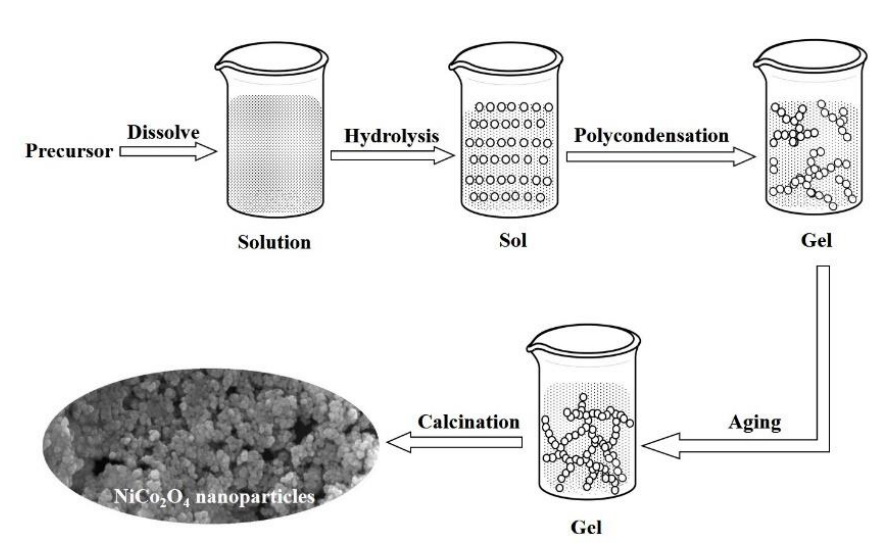


Figure 1. Schematic diagram of NiCo₂O₄ nanoparticles preparation

Firstly, 0.77 mmol of Ni(NO₃)₂·6H₂O and 1.54 mmol of CoCl₂·6H₂O were dissolved in 2.5 mL ethanol by ultrasonic treatment for 5 min, and then 0.025 g hexadecyl trimethyl ammonium bromide (CTAB) and 2.0 g propylene oxide were added to the dispersion and followed by stirring for 8 h at 25 °C. After reaction, the gel product was collected and cleaned by deionised water and

ethanol and dried at 60 °C for 12 h. Finally, the light green powder of the precursor was calcined in air atmosphere at 350 °C for 3 h in a muffle furnace to obtain the final NiCo₂O₄ nanoparticles.

Structure characterization

The morphologies and structures of the as-prepared NiCo₂O₄ nanoparticles were characterized by field emission scanning electron microscopy (SEM, JEOL JEM-7001F, Japan), transmission electron microscope (TEM, JEOL, JEM-700, Japan) and X-ray diffraction (XRD, D8 ADVANCE, Bruker Corporation). The composition and microstructure of the samples was performed on a Raman spectrometer (Raman, HORIBA, LABRAM HR800).

Electrode preparation and electrochemical measurements

The circular nickel foam with a diameter of 14 mm used as the working electrode current collector was firstly ultrasonicated for 10 min in 1 mol L-1 HCl solution, and then rinsed twice with acetone, ethanol and deionized water, respectively. Then, the cleaned nickel foam was put into a vacuum drying oven and dried at 60 °C for 12 h. The working electrode was prepared as follows. Firstly, the active material sample, carbon black and polyvinylidene fluoride (PVDF) were mixed with a mass ratio of 75:15:10 in an appropriate amount of N-methyl-2-pyrrolidone (NMP). The obtained mixture was ground to form the slurry, which was evenly coated on the surface of the treated nickel foam and dried at 60 °C for 8 h. The three-electrode system was used to determine the electrochemical performance of the working electrode. A platinum slice (2 \times 2 cm) and Hg/HgO electrode were used as the counter and reference electrode, respectively. All measurements were performed in 3 mol L-1 KOH aqueous solution. The sample electrode was tested by using CHI 660E electrochemical workstation (Shanghai ChenhuaInstrument co., LTD.) in a three-port H-type cell for cyclic voltammetry (CV) and constant current charge-discharge (GCD) test. The scanning rates of CV tests were 2, 5, 10, 15 and 20 mV s⁻¹ performed in the voltage scope of 0-0.5 V. GCD experiments were carried out in the potential range of 0-0.5 V with current densities of 1, 4, 7 and 10 A g⁻¹, respectively. The specific capacitance (C_m , F g^{-1}) values were calculated from charge-discharge curves according to the following equation (1):

$$C_{\rm m} = \frac{C}{m} = \frac{i\Delta t}{m\Delta u} \tag{1}$$

In Eq. (1), i(A), m (g), $\triangle t$ (s) and $\triangle u$ (V) represent discharge current, mass of active electrode material, total discharge time and potential window, respectively.

Results and discussion

Structural characterization

The surface morphologies of $NiCo_2O_4$ samples were investigated by SEM with different magnifications. As shown in Figure 2, the sample is composed of many regular and disordered nanoparticles with a diameter of about 20-30 nm. Obviously, there are some loosely packed porous structures between the nanoparticles, with the size ranging from tens to hundreds of nanometers. This porous structure and interaction space between $NiCo_2O_4$ nanoparticles is beneficial for improving the specific surface area by enhancing the transport facility of ions, shortening the pathway of electron migration, maintaining the chemical stability during redox reactions, and improving the electrochemical performance. Therefore, as obtained $NiCo_2O_4$ nanomaterial is a promising candidate electrode material for supercapacitors.

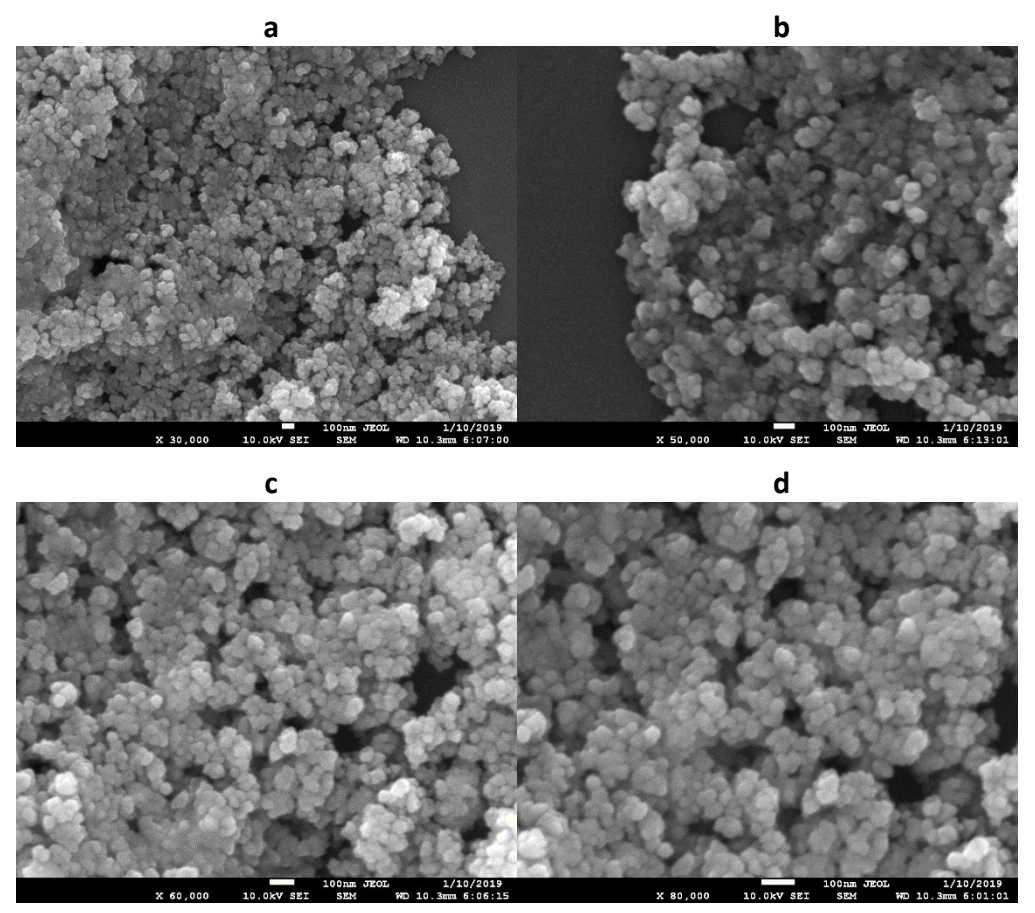


Figure 2. SEM images of as-obtained NiCo₂O₄ nanoparticles at different magnifications: $a - \times 30000$; $b - \times 50000$; $c - \times 60000$; $d - \times 80000$.

The detailed morphology, size and microstructure of the obtained $NiCo_2O_4$ nanoparticles were further examined by TEM. As shown in Figure 3(a) and (b), numerous nanoparticles are loosely packed together. In addition, Figure 3(c) and (d) show TEM magnification images of an individual diamond-like $NiCo_2O_4$ nanoparticles with a size of about 20-30 nm, in which the diamond-like structure contains a large number of nanopores. This unique porous structure will increase the contact area between the electrode and the electrolyte, which in turn will improve the electron and ion transport, improving thus electrochemical performance of the electrode [31].

The purity and crystal structure of the nickel foam substrate and as-prepared NiCo₂O₄ sample were determined by X-ray diffraction, and the corresponding XRD patterns are shown in Figure 4. It is found that all peaks located at 2 θ = 44.51, 51.85 and 76.37 ° can be perfectly indexed to (111), (200) and (220) planes of the nickel foam substrate (JCPDS 04-0850), respectively. The major diffraction peaks at 2θ = 31.15, 36.70, 44.62, 59.09 and 64.98° of NiCo₂O₄ (JCPDS No. 20-0781) correspond to the (220), (311), (400), (511) and (440) crystal planes, respectively [32]. It can be observed that all peaks in the pattern corroborate well with the standard pattern of face-centered cubic spinel NiCo₂O₄ with a space group of Fd3m. No excrescent peaks are detectable, indicating that the pure NiCo₂O₄ phase was successfully obtained. Moreover, broad and weak diffraction peaks indicate that NiCo₂O₄ exhibited inferior crystallinity and nanocrystallinity, which are favorable for NiCo₂O₄ nanoparticles to exhibit better capacitive performance [25].

To further evaluate the phase formation and structural features of the prepared $NiCo_2O_4$ nanoparticles, Raman spectroscopy was performed with a typical spectral range of 150-750 cm⁻¹, and the typical Raman spectrum of the sample is shown in Figure 5.

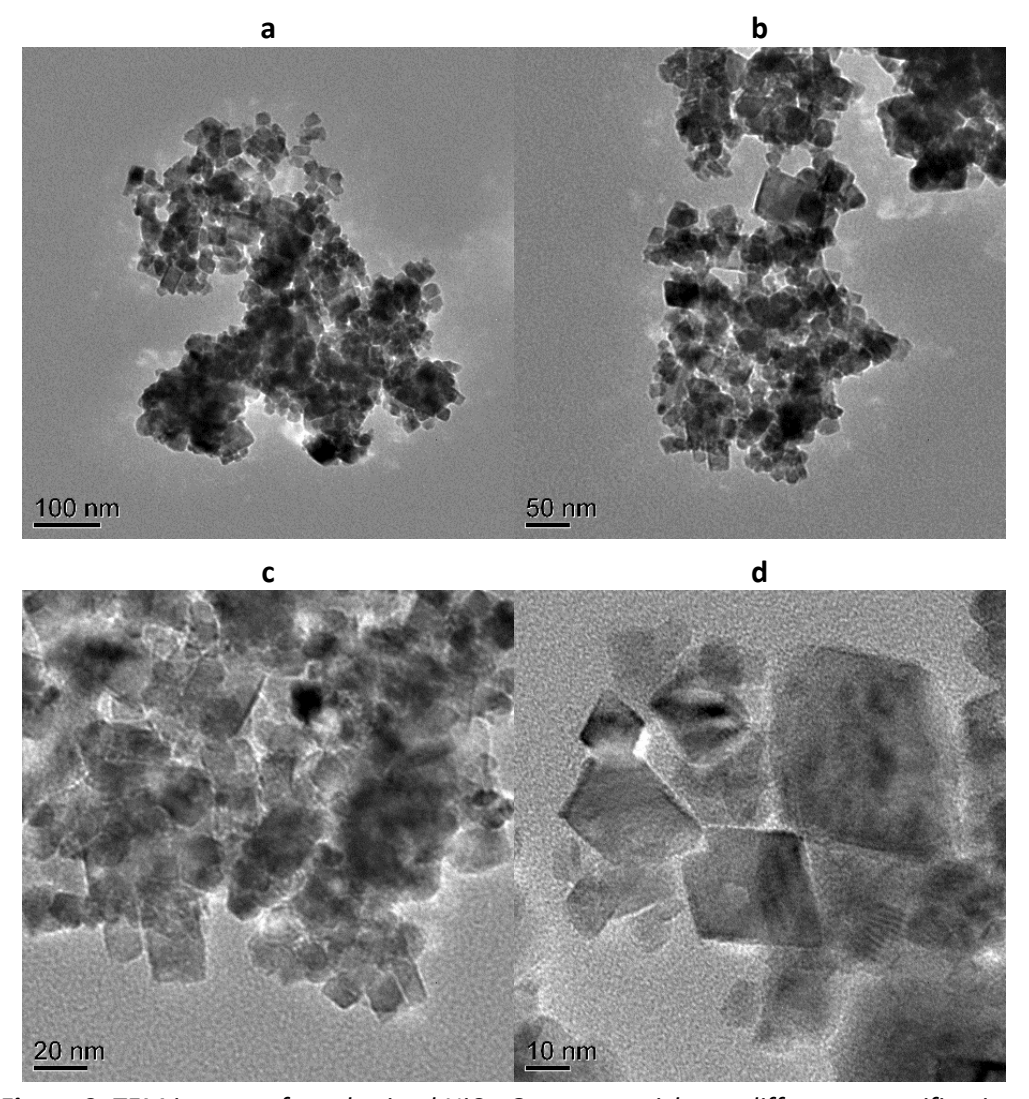


Figure 3. TEM images of as-obtained NiCo₂O₄ nanoparticles at different magnifications

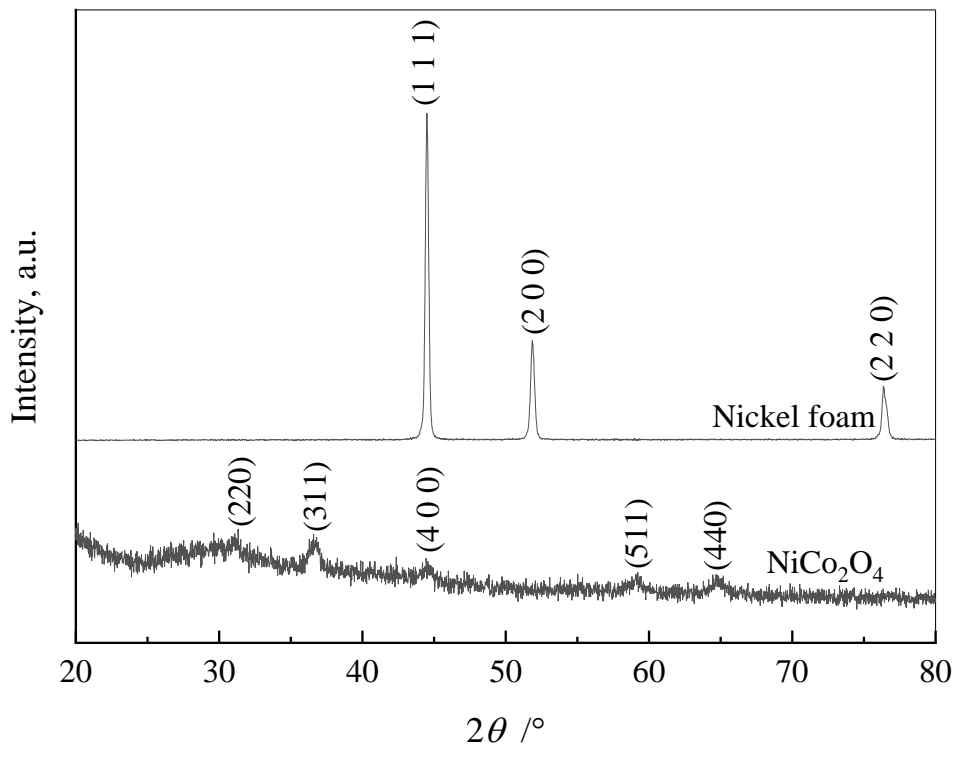


Figure 4. XRD patterns of the nickel foam substrate and as-prepared NiCo₂O₄ nanoparticles

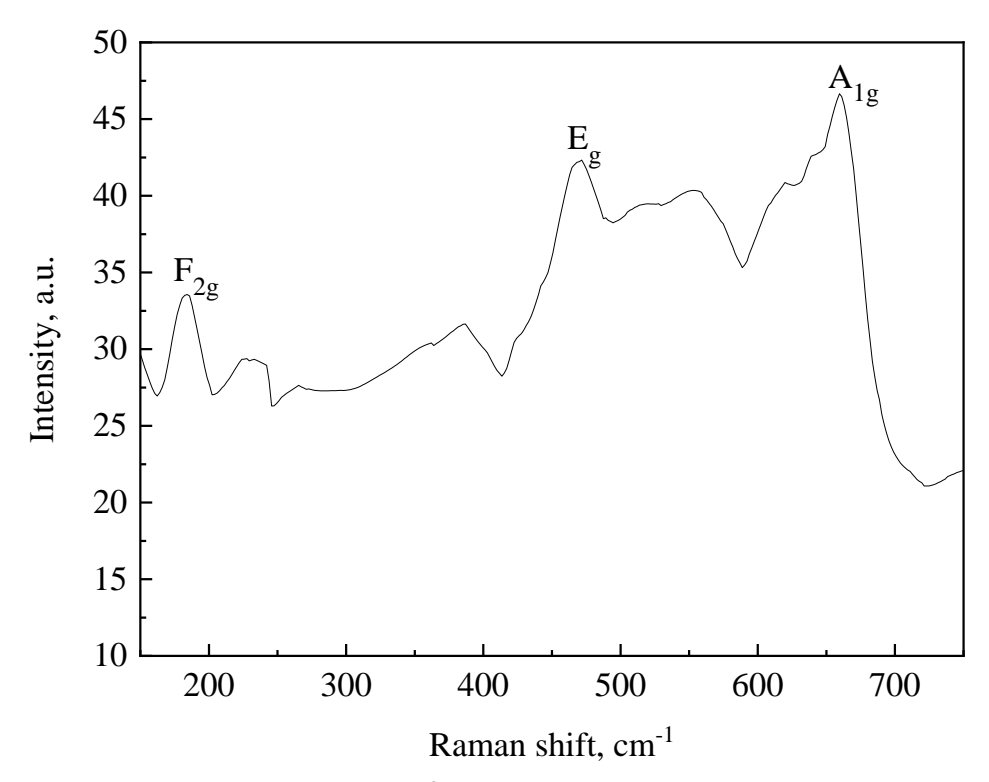


Figure 5. Raman spectrum of the as-prepared NiCo₂O₄ nanoparticles

The stretching vibration peaks observed at ~182.2 , ~469.1, and ~661.1 cm $^{-1}$ correspond to F_{2g}, E_g and A_{1g} modes of NiCo₂O₄ respectively, confirming its single-phase formation of spinel structure. The observed mode of the phonon is attributed to the vibration of Co-O and Ni-O, respectively [33]. Moreover, NiCo₂O₄ samples show only Co-O and Ni-O vibrations, indicating that the precursors of nickel and cobalt were completely decomposed at 350 °C, what is consistent with the literature [34] and implies that pure NiCo₂O₄ was formed after calcination. These results are well consistent with the XRD results, which further confirm the formation of NiCo₂O₄ nanoparticles.

Electrochemical characterization

The electrochemical capacitive performance of the as-prepared NiCo₂O₄ sample was evaluated by CV measurements using a three-electrode system. Figure 6 shows CVs recorded for NiCo₂O₄ nanoparticles in 3 mol L⁻¹ KOH aqueous electrolyte. The potential was scanned between 0 and 0.5 V at scanning rates of 2, 5, 10, 15 and 20 mVs⁻¹, respectively. A pair of redox peaks can be detected in each voltammogram, indicating that the electrode capacitance is mainly based on the redox mechanism related to reversible redox reactions of Ni²⁺/Ni³⁺ and Co³⁺/Co⁴⁺, associated with anions OH⁻ [35]. As can be seen from CV curves in Figure 6, the anodic peak potential at around \sim 0.48 V and cathodic peak potential at \sim 0.36 V are noticed at the scan rate of 2 mVs⁻¹, which is close to the literature value. Moreover, when the scanning rate increased from 5 to 20 mVs⁻¹, the position of the anodic peak shifts slightly from 0.48 to 0.50 V, indicating that the electrode material resistance is relatively low and electrochemical reversibility is good [18].

To further estimate the supercapacitive performance of the as-prepared $NiCo_2O_4$ nanoparticles, GCD measurements were carried out within the potential range from 0 to 0.5 V at current densities of 1, 4, 7 and 10 A g⁻¹, respectively. As shown in Figure 7, the charge-discharge curves are non-linear with an obvious plateau at around 0.45 V and 0.39 V. This is well consistent with CV results and further verifies the pseudocapacitive behavior and good reversibility of the redox process at $NiCo_2O_4$ electrode [18].

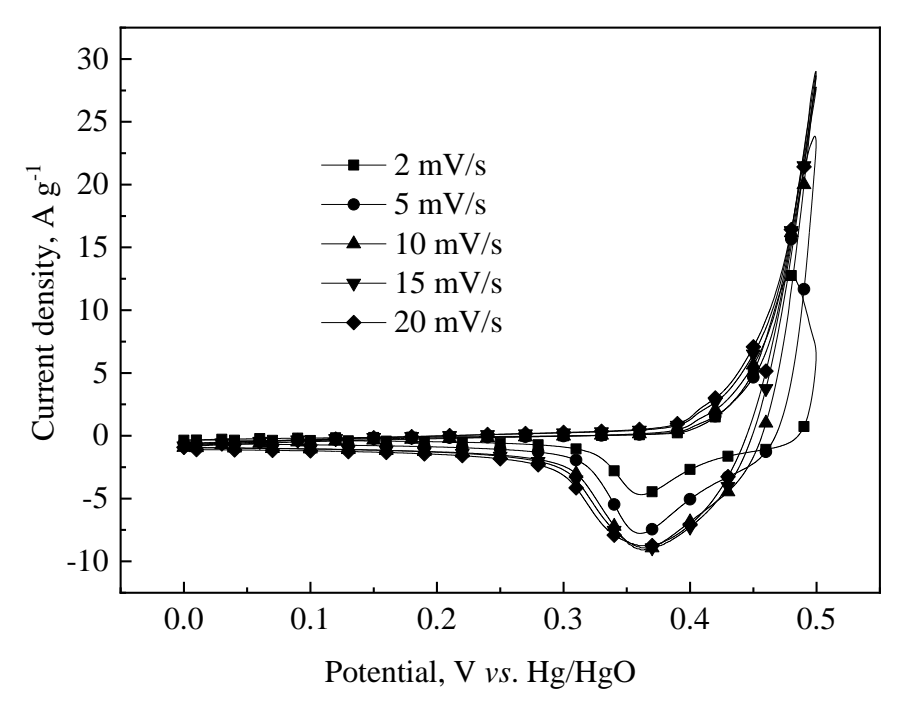


Figure 6. CV curves of as-prepared NiCo₂O₄ electrode in a three-electrode system scanned between 0 and 0.5 V at various scan rates

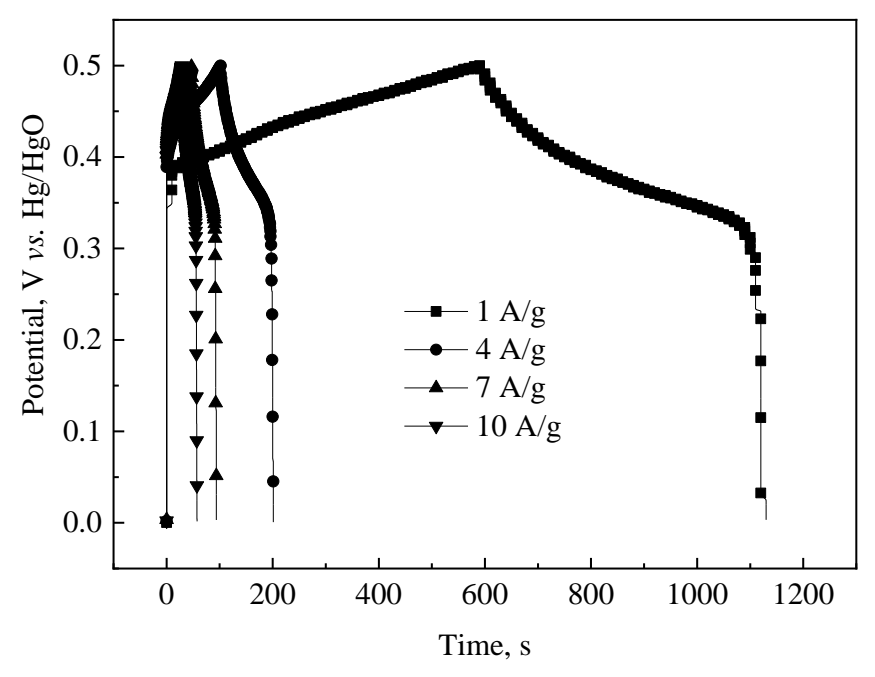


Figure 7. GCD curves of as-prepared NiCo $_2$ O $_4$ electrode at various current densities between 0 and 0.5 V

Based on the discharge curves, the specific capacitances of the as-prepared $NiCo_2O_4$ electrode were calculated according to Eq. (1), and the results are illustrated in Figure 8. Specific capacitances of as-prepared $NiCo_2O_4$ are as high as 1080, 800, 651 and 574 F g⁻¹ at discharge current densities of 1, 4, 7 and 10 A g⁻¹, respectively. Compared with the current density of 1 A g⁻¹, the retained capacitances were still 74.1, 60.3 and 53.1 %, even the current density was increased to 4, 7 and 10 A g⁻¹, what suggests good retention rate performance. The excellent electrochemical properties of $NiCo_2O_4$ nanoparticles can be attributed to the small particle size, which will increase the contact area of electrolyte/electrode, thus providing more active sites for rapid redox reactions which undoubtedly contributes to the high capacitance [35]. Besides, the nanoporous structure between the particles also allows the electrolyte ions to be transported quickly into the bulk materials, what further enhances the electrode rate capability.

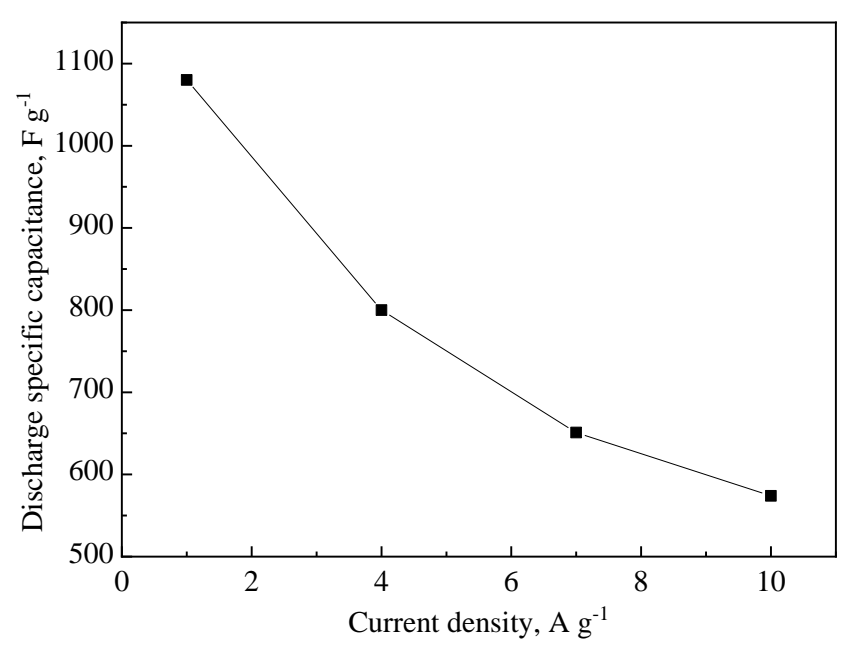


Figure 8. Specific capacitance of as-prepared NiCo₂O₄ electrode as a function of discharge current density

The cycling stability of the as-prepared NiCo₂O₄ electrode in 3 mol L⁻¹ KOH aqueous electrolyte was examined by applying 100 cycles within the potential range of 0-0.5 V at current densities of 4, 7 and 10 A g⁻¹, and the results are shown in Figure 9. During the cycling, the specific capacitance of the as-prepared NiCo₂O₄ electrode remained almost unchanged at all current densities. The initial discharge specific capacitance of NiCo₂O₄ electrode is 800, 651 and 574 F g⁻¹ at the current density of 4,7 and 10 A g⁻¹, respectively. After 100 cycles, the specific capacitance decreases to 758, 597 and 521 F g⁻¹, showing that the corresponding specific capacitance retention rates were 94.8, 91.7 and 90.8 % and indicating that NiCo₂O₄ electrode has good electrochemical stability. Better cyclic stability can be attributed to the unique pore structure, which can be used as the "release zone" of ions and internal nanogrids that buffers possible volume changes due to OH⁻ ions insertion/extraction process during cycling, improving thus its structural stability.

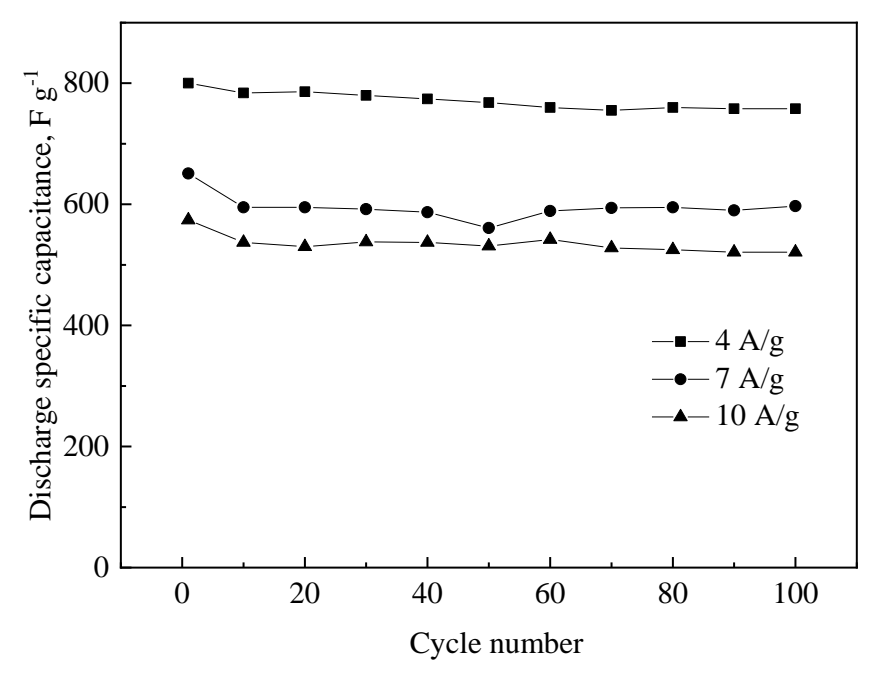


Figure 9. Cyclic stability of as-prepared NiCo₂O₄ electrode at various discharge current densities

Conclusion

By using Ni(NO₃)₂·6H₂O and CoCl₂·6H₂O as raw materials, a promising electrode material, NiCo₂O₄ nanoparticles, were synthesized successfully *via* the sol-gel process followed by calcining at 350 °C. In the unique structure of synthesized nanoparticles, there are obvious porous structures formed among large number of nanoparticles, which provide an effective way for rapid reversible reaction, improving thus electrochemical properties of NiCo₂O₄ material. Electrochemical characterization showed high specific capacitance, good rate capability and good cycling stability of the prepared NiCo₂O₄ nanomaterial. High specific capacitance of 1080 F g⁻¹ was achieved at the current density of 1 A g⁻¹, while specific capacitances of 800, 651 and 574 F g⁻¹were obtained at the discharge current densities of 4, 7 and 10 A g⁻¹, respectively. After 100 cycles, the specific capacitance decreases to 758, 597 and 521 F g⁻¹, suggesting the corresponding specific capacitance retention rates of 94.8, 91.7 and 90.8 %. The excellent electrochemical capacitive performance, low cost, simple and easy fabrication of the as-prepared NiCo₂O₄ nanoparticles render this material as the promising electrochemical capacitor electrode material.

Acknowledgments: This work is supported by the Program for Science & Technology Innovation Team in Universities of Henan Province (Grant No. 16IRTSTHN016), the National Natural Science Foundation of China (Grant No. 21503193), and the National Natural Science Foundation of China (Grant No. U1404201).

References

- [1] Y. Zhang, H. Feng, X. Wu, L. Wang, A. Zhang, T. Xia, H. Dong, X. Li and L. Zhang, *International Journal of Hydrogen Energy* **34** (2009) 4889-4899.
- [2] Y. Li, X. Han, T. Yi, Y. He and X. Li, Journal of Energy Chemistry 31 (2019) 54-78.
- [3] W. Gu and G. Yushin, Wiley Interdisciplinary Reviews: Energy and Environment **3** (2014) 424-473.
- [4] J. Sun, E. Lei, C. Ma, Z. Wu, Z. Xu, Y. Liu, W. Li and S. Liu, *Electrochimica Acta* **300** (2019) 225-234.
- [5] Y. Jiao, W. Hong, P. Li, L. Wang and G. Chen, Applied Catalysis B: Environmental 244 (2019) 732-739.
- [6] Y. Duan, T. Hu, L. Yang, J. Gao, S. Guo, M. Hou and X. Ye, *Journal of Alloys and Compounds* **771** (2019) 156-161.
- [7] Y. Zhang, Q.-q. Yao, H.-l. Gao, L.-s. Zhang, L.-z. Wang, A.-q. Zhang, Y.-h. Song and L.-x. Wang, *Journal of Analytical and Applied Pyrolysis* **111** (2015) 233-237.
- [8] A. Younis, D. Chu and S. Li, *Journal of Materials Chemistry A* **3** (2015) 13970-13977.
- [9] Y. Z. Ma, Z. X. Yu, M. M. Liu, C. Song, X. N. Huang, M. Moliere, G. S. Song and H. L. Liao, *Ceramics International* **45** (2019) 10722-10732.
- [10] N. Chen, A. Younis, S. Huang, D. Chu and S. Li, *Journal of Alloys and Compounds* **783** (2019) 772-778.
- [11] Y. Zhang, H.-l. Gao, X.-d. Jia, S.-w. Wang, J. Yan, H.-w. Luo, K.-z. Gao, H. Fang, A.-q. Zhang and L.-z. Wang, *Journal of Renewable and Sustainable Energy* **10** (2018) 054101-054110.
- [12] H. Zhou, X. Zhi, W. Zhang and H.-J. Zhai, Organic Electronics 69 (2019) 98-105.
- [13] Q. Zhang, B. Sun, J. Sun, N. Wang and W. Hu, *Journal of Electroanalytical Chemistry* **839** (2019) 39-47.
- [14] L. Liu, H. Zhang, L. Fang, Y. Mu and Y. Wang, *Journal of Power Sources* **327** (2016) 135-144.
- [15] X. Y. Liu, Y. Q. Zhang, X. H. Xia, S. J. Shi, Y. Lu, X. L. Wang, C. D. Gu and J. P. Tu, *Journal of Power Sources* **239** (2013) 157-163.
- [16] Z. Z. Zeng, L. Z. Zhu, E. S. Han, X. C. Xiao, Y. R. Yao and L. M. Sun, *Ionics* **25** (2019) 2791-2803.
- [17] Y. Q. Wu, X. Y. Chen, P. T. Ji and Q. Q. Zhou, *Electrochimica Acta* **56** (2011) 7517-7522.
- [18] Y. Zhu, X. Pu, W. Song, Z. Wu, Z. Zhou, X. He, F. Lu, M. Jing, B. Tang and X. Ji, *Journal of Alloys and Compounds* **617** (2014) 988-993.
- [19] S. Li, K. Yang, P. Ye, H. Jiang, Z. Zhang, Q. Huang and L. Wang, *Applied Surface Science* **473** (2019) 326-333.
- [20] W. Zhang, W. Xin, T. Hu, Q. Gong, T. Gao and G. Zhou, *Ceramics International* **45** (2019) 8406-8413.
- [21] Y. Luo, R. Guo, T. Li, F. Li, L. Meng, Z. Yang, Y. Wan and H. Luo, *ChemElectroChem* **6** (2019) 690-699.
- [22] H.-L. Fan, J. Zhang, W. Ju, B.-X. Liu, X.-F. Zhao, X.-C. Liu and X.-B. Yi, *International Journal of Nanomanufacturing* **15** (2019) 92-104.

- [23] Y. L. D. LI, R. Chen, H NI, Acta Metallurgica **54** (2018) 1179-1186.
- [24] J. Dai, R. Zhao, J. Xiang, F. Wu, L. Xin, Y. Zhang and S. Ma, *Science of Advanced Materials* **11** (2019) 379-385.
- [25] M. C. Liu, L. B. Kong, C. Lu, X. M. Li, Y. C. Luo and L. Kang, *ASC Applied Materials & Interfaces* **4** (2012) 4631-4636.
- [26] Z. Wu, Y. Zhu and X. Ji, *Journal of Materials Chemistry A* **2** (2014) 14759-14772.
- [27] N. Wang, B. Sun, P. Zhao, M. Yao, W. Hu and S. Komarneni, *Chemical Engineering Journal* **345** (2018) 31-38.
- [28] Y. Xiao, Y. Lei, B. Zheng, L. Gu, Y. Wang and D. Xiao, RSC Advances 5 (2015) 21604-21613.
- [29] S. N. Gao, F. Liao, S. Z. Ma, L. L. Zhu and M. W. Shao, *Journal of Materials Chemistry A* **3** (2015) 16520-16527.
- [30] H.-W. Wang, Z.-A. Hu, Y.-Q. Chang, Y.-L. Chen, H.-Y. Wu, Z.-Y. Zhang and Y.-Y. Yang, *Journal of Materials Chemistry* **21** (2011) 10504-10511.
- [31] L. Ma, X. Shen, Z. Ji, X. Cai, G. Zhu and K. Chen, *Journal of Colloid and Interface Science* **440** (2015) 211-218.
- [32] C. Wang, X. Zhang, D. Zhang, C. Yao and Y. Ma, Electrochimica Acta 63 (2012) 220-227.
- [33] S. Karmakar, S. Varma and D. Behera, *Journal of Alloys and Compounds* **757** (2018) 49-59.
- [34] P. Bhojane, S. Sen and P. M. Shirage, Applied Surface Science 377 (2016) 376-384.
- [35] Y. Zhu, X. Ji, Z. Wu, W. Song, H. Hou, Z. Wu, X. He, Q. Chen and C. E. Banks, *Journal of Power Sources* **267** (2014) 888-900.



Open Access: ISSN 1847-9286

www.jESE-online.org

Original scientific paper

Synthesis and characterization of LaMnO₃ nanocrystals and graphene oxide: fabrication of graphene oxide–LaMnO₃ sensor for simultaneous electrochemical determination of hydroquinone and catechol

Sedighe Akbari¹, Mohammad Mehdi Foroughi¹, Hadi Hassani Nadiki¹ and Shohreh Jahani²

¹Department Department of Chemistry, Kerman Branch, Islamic Azad University, Kerman, Iran ²NanoBioElectrochemistry Research Center, Bam University of Medical Sciences, Bam, Iran

Corresponding author: [™]mohammadmehdi869@yahoo.com; Tel. +98 34331321750

Received: November 1, 2018; Revised: April 7, 2019; Accepted: May 9, 2019

Abstract

For the first time, a new method for preparation of graphene oxide-LaMnO $_3$ (GO-LaMnO $_3$) nanocomposite as a material of electrochemical sensor for simultaneous determination of catechol (CT) and hydroquinone (HQ) is developed. LaMnO $_3$ nanoparticles have been characterized by Fourier-transform infrared spectroscopy (FT-IR), scanning electron microscopy (SEM), X-ray diffraction (XRD), transmission electron microscopy (TEM) and energy dispersive X-ray analysis (EDX) technique. Due to the excellent catalytic activity, enhanced electrical conductivity and high surface area, the simultaneous determination of HQ and CT with two well-defined peaks has been achieved at the GO-LaMnO $_3$ modified electrode. Comparing with unmodified electrodes, the oxidation currents of HQ and CT increased remarkably. Also, the result exhibited a great decrease in anodic overpotential resulting in about 150 mV negative shift of potential. The catalytic peak current values are found linearly dependent on the HQ and CT concentrations in the range of 0.5–433.3 and 0.5–460.0 μ M with sensitivity of 0.0719 and 0.0712 μ A μ M $^{-1}$, respectively. The detection limits for HQ and CT are determined as 0.06 and 0.05 μ M, respectively.

Keywords

Catechol; hydroquinone; graphene oxide; LaMnO₃ nanoparticles; voltammetry

Introduction

Phenolic materials compounds are widely used in a broad class of industries, such as coal mining, cosmetics, paint, pharmaceutical preparation and polymer [1]. During the manufacturing and application process of these compounds, some of them are unintentionally released into environment,

polluting thus ground waters and rivers. Catechol (CT) and hydroquinone (HQ) are two most important isomers of phenolic materials which are announced as environmental contaminants by the European Union and the US Environmental Protection Agency [2]. Simultaneous determination of HQ and CT is very important for environmental analysis because they coexist in environmental samples as environmental contaminants of high toxicity and too difficult to degrade [3]. CT has also been found in cigarette smoke and researches have demonstrated that it induces damage to DNA and can cause cancer [4,5]. Hence, it is essential to develop a sensitive, simple, rapid and cheap analytical method for determination of dihydroxybenzene isomers. So far, many analytical methods have been reported for their determination, such as capillary zone electrophoresis, liquid chromatography, synchronous fluorescence, gas chromatography/mass spectrometry, chemiluminescence, and pH based-flow injection analysis [6-12]. Electrochemical methods have some attractive advantages such as simple and fast response, low maintenance cost, excellent selectivity and high sensitivity. However, a serious obstacle is that the oxidation peak potentials of the isomers are too close at a bare electrode which causes overlapping of voltammetric responses, making their discrimination very difficult [13-17]. A chemically modified electrode is a superior approach to solve the peak separation problem by applying a modifier [18-24]. Hence, a few modified electrodes have already been reported to determine HQ and CT such as GCE modified by carbon nanotubes (CNT), poly-amid sulfonic acid-CNTs, graphenechitosan composite, carbon nanotubes/poly (3-methylthiophene), penicillamine), Zn/Al layered double hydroxide film, or gold-graphene [25-31].

Graphene (Gr) nano sheets have a great potential for the applications in the development of electrochemical sensors and biosensors. Gr is used as a support material to improve the electrochemical reactivity of molecules on the surface of modified electrode, what is due to its superior mechanical, electrical, thermal, and optical properties [32]. On the other side, its low energy storage capacity greatly hinders its extensive use. To overcome these shortcomings, many researches have been focused on the synthesis of graphene-based inorganic composites. Recently, the synthesis procedures of new composites of graphene with inorganic particles, such as metal, metal oxide, metal hydroxide, or metal sulfide particles, have been reported [33-38]. Due to presence of graphene and inorganic particles, the fabricated electrochemical sensors display exceptional improvement in electrical properties and functionality for different types of composites. Among inorganic particles, perovskite nanocrystals having electrically active structure and convenient magnetic and dielectric properties have been broadly studied and employed in the development of electrochemical gas sensors, solid fuel cells and many of electrochemical catalytic processes [39-44].

To the best of our knowledge, no study has already been reported for the electroanalysis and simultaneous determination of HQ and CT using GCE modified by GO-LaMnO₃. For the first time, we have described the preparation of a new, GO-LaMnO₃ modified GCE for the electroanalysis and determination of HQ and CT. In this paper, we have evaluated analytical performance of this sensor for simultaneous determination of HQ and CT by the voltammetry technique.

Experimental

Reagents and solutions

Manganese sulphate, lanthanum chloride and oleic acid were purchased from Merck and used as received. The HQ and CT were purchased from Sigma-Aldrich (Sigma-Aldrich, USA) and used as received. A 1.0×10^{-2} mol L⁻¹ HQ and CT solution was prepared daily by dissolving appropriate amounts of HQ and CT in water and the solution was diluted to 100 mL with distilled deionized water. The solution was kept in a refrigerator in dark. More dilute solutions were prepared by serial dilution of

phosphate buffer solutions. Phosphate buffer solution (PBS, $0.1 \text{ mol } L^{-1}$) was prepared by mixing the stock solution of $0.1 \text{ mol } L^{-1} \text{ NaH}_2\text{PO}_4$ and $0.1 \text{ mol } L^{-1} \text{ Na}_2\text{HPO}_4$, and the pH was adjusted by HCl or NaOH. All other materials used were of analytical reagent grade and all solutions were prepared with double distilled deionized water. All chemicals were used without additional purification.

Apparatus

FT-IR spectra were recorded as KBr disks on a JASCO FT/IR-460 PLUS instrument. X-ray powder diffraction (XRD) analysis was conducted on a Philips analytical PC-APD X-ray diffractometer with graphite monochromatic Cu K α radiation (α_1 , λ_1 = 1.54056 Å, α_2 , λ_2 = 1.54439 Å) to verify the formation of products. Surface analysis was done using a low vacuum JSM, 6380 LV scanning electron microscope (SEM) after coating the samples with a thin layer of gold by magnetron sputtering. Energy-dispersive X-ray spectrometry (EDX) is a significant nondestructive analytical tool typically applied for the chemical composition analysis. Electrochemical determinations were done with a SAMA 500 Electroanalyser (SAMA Research Center, Iran) controlled by a personal computer. The three-electrode electrochemical cell system consisted of glassy carbon working electrode (GCE, modified or unmodified), a saturated calomel reference electrode (SCE) and a Pt wire electrode as the auxiliary electrode. All electrochemical determinations were carried out under a pure nitrogen atmosphere at room temperature.

Synthesis of perovskite nanocrystal

In order to synthesize lanthanum manganese oxide nanocrystals, manganese sulphate and lanthanum chloride were chosen as starting materials. Solutions of manganese sulphate (10 ml, 0.1 M) and lanthanum chloride (10 ml, 0.1 M) were prepared and mixed together. Oleic acid (2 ml) was added into the pink solution. The pH of solution was adjusted to 7-8 by dropwise addition of NaOH (1.5 M) in the stirred solution. After complete precipitation, it was nebulized in the ultrasonic at 60 °C for 30 min. The precipitate was centrifuged for 15 min at (3000 rpm), washed with deionized distilled water and dried at 100 °C for 8 h. The achieved product was calcinated at 1100 °C for 6 h to let the sample self-ignite and burn off the impurity organic compound in the crystal.

Electrochemical synthesis of graphene oxide

The graphene oxide nano sheets were prepared by the electrochemical functionalization of graphite. In a typical synthesis, 10 mL 1-octyl-3-methyl-imidazolium hexafluorophosphate ([C8mim]+[PF₆]-) and 20 mL water were mixed and used as the electrolyte. A static potential of 2 V was applied between two graphite rods (6.0 cm distance between two rods) for 2 h and then potential increased to 6 V for 6 h. After corrosion for 6 h at room temperature, a black precipitate of GO was obtained at the bottom of the reactor. The black precipitate was separated and washed with ethanol and then sonicated for 30 min. The product was dried for 3 h in an oven at 70 °C.

Preparation of GCE and modified electrode

Prior to the surface modification, GCE was carefully polished with 0.3 μ m and 0.05 μ m alumina slurries to obtain a mirror-like surface. After sonication in water and ethanol successively for 20 s, the electrode was rinsed with water, and then dried under an infrared lamp. The GCE/GO-LaMnO₃ was prepared by casting 4 μ L of GO-LaMnO₃ suspension (0.01 g LaMnO₃ + 0.005 g GO + 50 μ L chitosan 1 % + 0.95 mL H₂O) on the surface of cleaned GCE. The solvent was then evaporated under an infrared heat lamp. As controls, GCE/GO and GCE/ LaMnO₃ were also fabricated with similar procedure by replacing GO-LaMnO₃ hybrid materials with GO or LaMnO₃, respectively.

Results and discussion

Characterization of LaMnO₃ nanocrystals

The FT-IR spectra of the pure oleic acid (a), precursor (b) and LaMnO₃ nanoparticles after calcination (c) are shown in Figure 1(A). In curve (a), two sharp bands at 2925 and 2854 cm⁻¹ are attributed to the asymmetric CH₂ stretch and the symmetric CH₂ stretch, respectively. The intense peak at 1710 cm⁻¹ was derived from the existence of the C=O stretch and the band at 1285 cm⁻¹ exhibits the presence of the C=O stretch. In the curve (b), the asymmetric CH₂ stretch and the symmetric CH₂ are shifted to 2922 and 2853 cm⁻¹, respectively. The surfactant molecules in the adsorbed state were subjected to the field of the solid surface. As a result, the characteristic bands shifted to a lower frequency region which indicates that the hydrocarbon chains in the monolayer surrounding the precursor are in a closed-packed, crystalline state. All these bands disappeared when the precursor was calcinated at 800 °C, but two strong bands appear in the range of 400-600 cm⁻¹ related to metal-O and O-metal-O vibration of LaMnO₃ perovskite (Fig. 1(A) (c)).

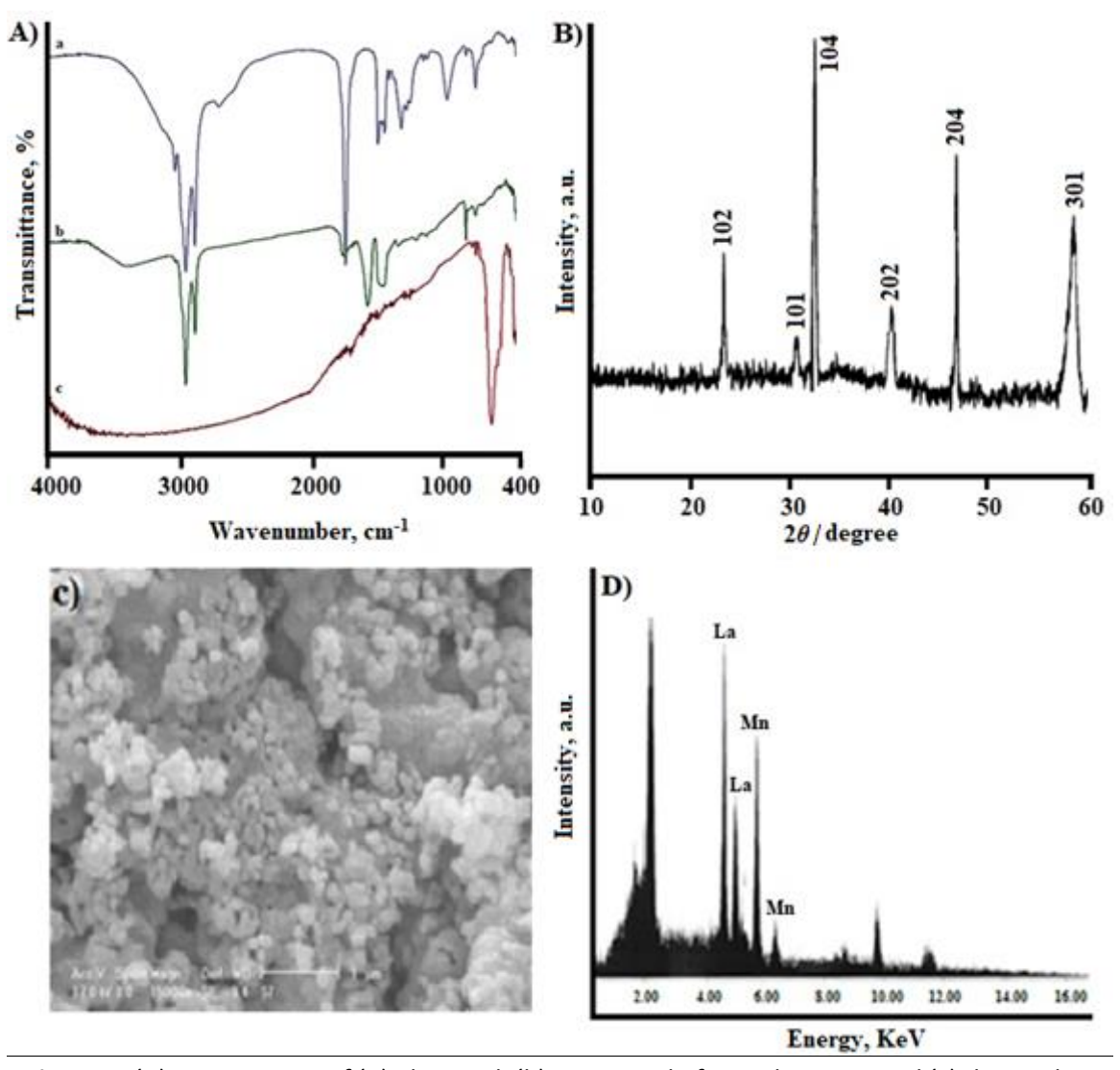


Figure 1. (A) FT-IR spectra of (a) oleic acid, (b) precursor before calcination and (c) the product after calcination, (B) XRD pattern of the product, (C) SEM image of LaMnO $_3$ (D) EDX of nanocrystals

XRD pattern of LaMnO₃ sample prepared *via* the ultrasonic-assisted co-precipitation process at 1100 °C is shown in Figure 1(B). For LaMnO₃ nanoparticles all diffraction peaks can be directly

indexed to a hexagonal phase of LaMnO₃ according to the JCPDS No. 23-0484 and no additional peaks for other impurities can be detected, indicating high purity of prepared sample. Furthermore, the narrow sharp peaks suggest that LaMnO₃ nanoparticles are well crystallized. The size distribution of LaMnO₃ nanoparticles has been estimated from the XRD spectra using the Debye–Scherrer equation [45]:

$$D_{\rm c} = \frac{K\lambda}{\beta\cos\theta}$$

where D is the crystallite size, K is the so-called shape factor which usually takes a value about 0.9, λ is the wavelength of radiation, β is the corrected full width at half maximum (FWHM), and θ is diffraction angle. The crystallite size of LaMnO₃ was estimated as 54 nm at 1100 °C. The morphologies of LaMnO₃ nanoparticles were studied by SEM. As can be seen from Figure 1(C), LaMnO₃ crystal is made from spherical particles with average size of 56 nm. The purity of the nanocrystalline product was evaluated by EDX (Figure 1(D)), which showed that the sample was merely composed of La and Mn.

Characterization of GO and GO-LaMnO₃ nanocomposite

TEM image shown in Figure 2A proves the formation of very thin GO. The flake-like GO shows a very stable nature under irradiation of electron beam. Very thin and featureless sections are likely to be few layers of GO, suggesting that the electrochemical method is slight, but strong enough to break down the van der Waals interaction and make GO layers by fractional exfoliation of the graphite surface. As expected, TEM image of GO-LaMnO₃ presented in Figure 2B shows well dispersed combinations of LaMnO₃ nanoparticles on GO when LaMnO₃ and GO are mixed together, which may cause many conducting channels between the electrode and electrolyte for electron transfer.

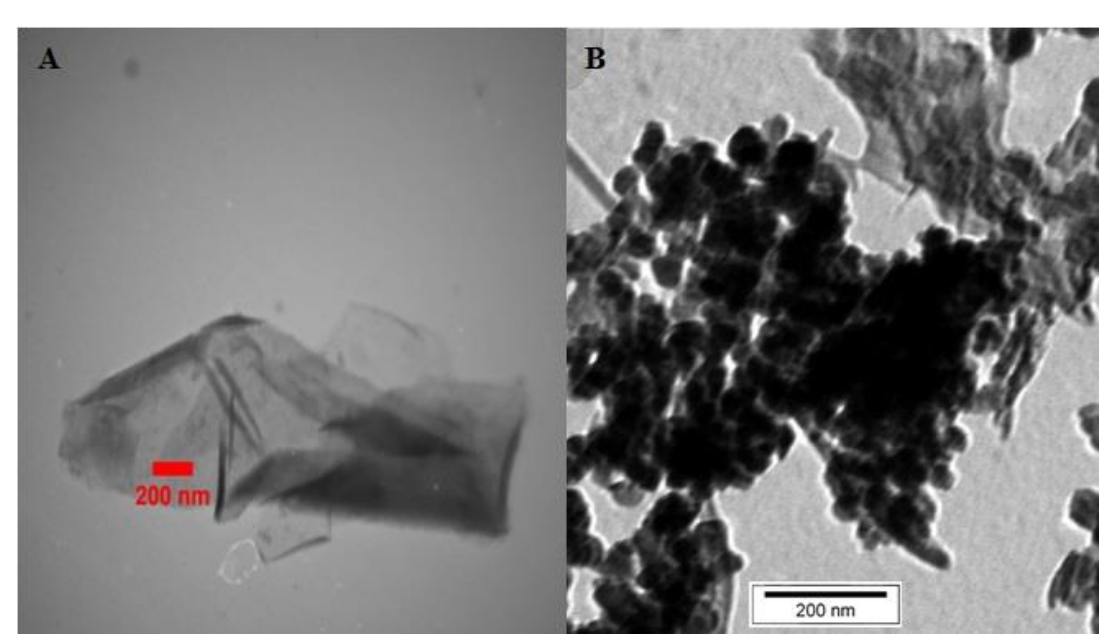


Figure 2. TEM image of (A) GO and (B) GO-LaMnO₃.

Voltammetric behavior of mixed HQ and CT

Electrochemical behavior of mixed components of HQ and CT (166.0 μ M of each) in 0.1 M PBS of pH 5 was carefully investigated at the surfaces of bare GCE (BGCE), GCE/LaMnO₃ and GCE/GO-LaMnO₃ using cyclic voltammetry. BGCE electrode showed a weak and broad oxidation peak for a mixture of HQ and CT at 0.33 V (curve a in Figure 3) suggesting slow electron transfer kinetics. The

oxidation peaks of HQ and CT are merged with a very low peak current. In contrast, the GCE/LaMnO₃ modified electrode showed two well-defined and sharp oxidation peaks for HQ and CT at 0.11 and 0.21 V vs. SCE, and two corresponding reduction peaks. It can be seen from curve b in Figure 3 that the oxidation peak current for HQ and CT at GCE/LaMnO₃ is several times larger than that of the unmodified electrode (BGCE) because of catalytic property of LaMnO₃ that acts as a promoter by increasing the rate of electron transfer. The potential values of peaks shifted to less positive potentials comparing with BGCE. After addition of GO to the modifier composition, peak current values increased (curve c in Figure 3) due to high surface area and conductivity of GO. The separation of oxidation peak potential of HQ-CT was 0.1 V which is high enough for the simultaneous determination of two isomers.

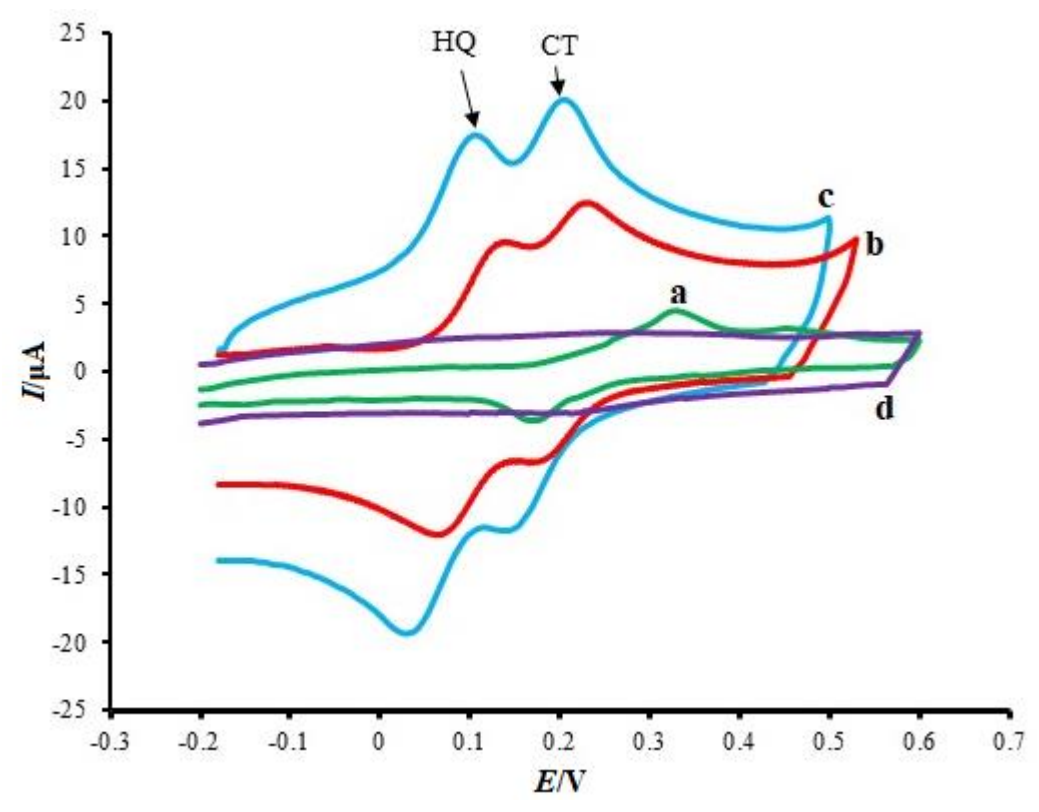


Figure 3. CVs recorded in PBS (0.1 M pH 5) in presence of HQ and CT (166.0 μ M each) at (a) BGCE, (b) GCE/LaMnO₃, (c) GCE/GO-LaMnO₃ electrodes and in absence of HQ and CT (d). Scan rate: 100 mV s⁻¹.

Effect of pH on the oxidation of HQ and CT

The acidity of electrolyte has a significant influence on the HQ and CT electro-oxidation because protons take part in the electrode reaction. The effect of pH on GCE/GO-LaMnO₃ current signal was carefully investigated by cyclic voltammetry using 0.1 M buffer solutions at pH ranging from 2 to 6. The results are shown in Figure 4(A). Obviously, the peak current values of HQ and CT increased with an increase of the solution pH until pH reached 5 and then decreased. It can be seen from Figure 4(B) that the highest peak current value is for both compounds obtained at pH 5. Also, as pH of the medium was gradually increased, peak potentials for the oxidation of HQ and CT are shifted towards less positive values, showing that protons have taken part in the electrode processes. Since phosphate buffer solution at pH 5 gave the best response in terms of peak current value, peak shape and negative shift, it was selected as the optimal pH for further studies. Plot of $E_p vs$. pH for HQ and CT in the working pH range is shown in Figure 4(C). E_p values of two compounds showed linear relationship with pH of the buffer solution according to the following equations:

CT:
$$E_p / V = -0.06 \text{ pH} + 0.506 \quad (R^2 = 0.999)$$
 (1)

HQ:
$$E_p / V = -0.063 \text{ pH} + 0.41$$
 (R²= 0.9963)

The observed slopes of 0.063 and 0.06 mV/pH for HQ and CT are close to the anticipated Nernstian value for two-electron, two-proton electrochemical reaction [46]. Therefore, it can be concluded that equal number of electrons and protons are involved in both electrode reactions. The presumed HQ and CT oxidation mechanisms are presented in Scheme 1.

Scheme 1. Probable oxidation mechanism for HQ and CT

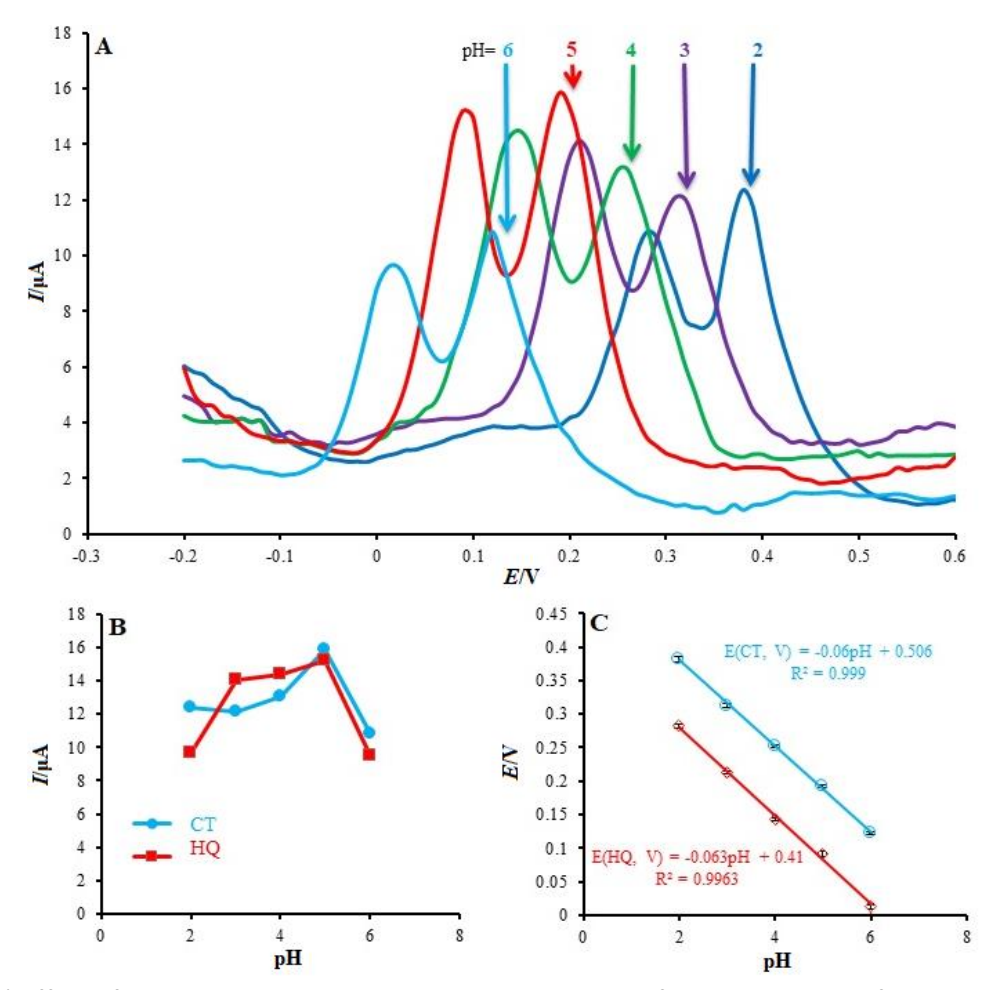


Figure 4. (A) Effect of pH on the peak separation and peak current for the oxidation of HQ and CT (100.0 μ M each); pH 2–6. Scan rate: 100 mVs⁻¹. (B) Plots of peak currents vs. pH. (C) Plots of peak potentials vs. pH.

Influence of scan rate on electrochemical behavior of HQ and CT

The influence of the scan rate on the oxidation peak currents of HQ and CT was investigated on the GO-LaMnO $_3$ modified GCE by cyclic voltammetry. As can be seen in Figure 5(A), the peak current values continuously increase with the increase of scan rate. As shown in Figure 5(B), the current is directly proportional to the square root of the scan rate in the range of 10–1000 mV s $^{-1}$, which powerfully proposed that the redox reactions of HQ and CT are diffusion controlled. Also, the results show clearly that the peak separation of HQ and CT is satisfactory for their separate analysis at higher scan rates. It is additionally observed in Figure 5 that with increasing of the scan rate, potential of the oxidation peak shifted positively, while potential of the reduction peak shifted negatively. This pointed to a kinetic limitation existing at higher scan rates in the course of the reaction between the GCE/GO-LaMnO $_3$ composite and HQ and CT. Due to our study, the scan rate of 100 mV s $^{-1}$ has to be ultimately chosen to reach the best efficiency for peak currents and peak separation.

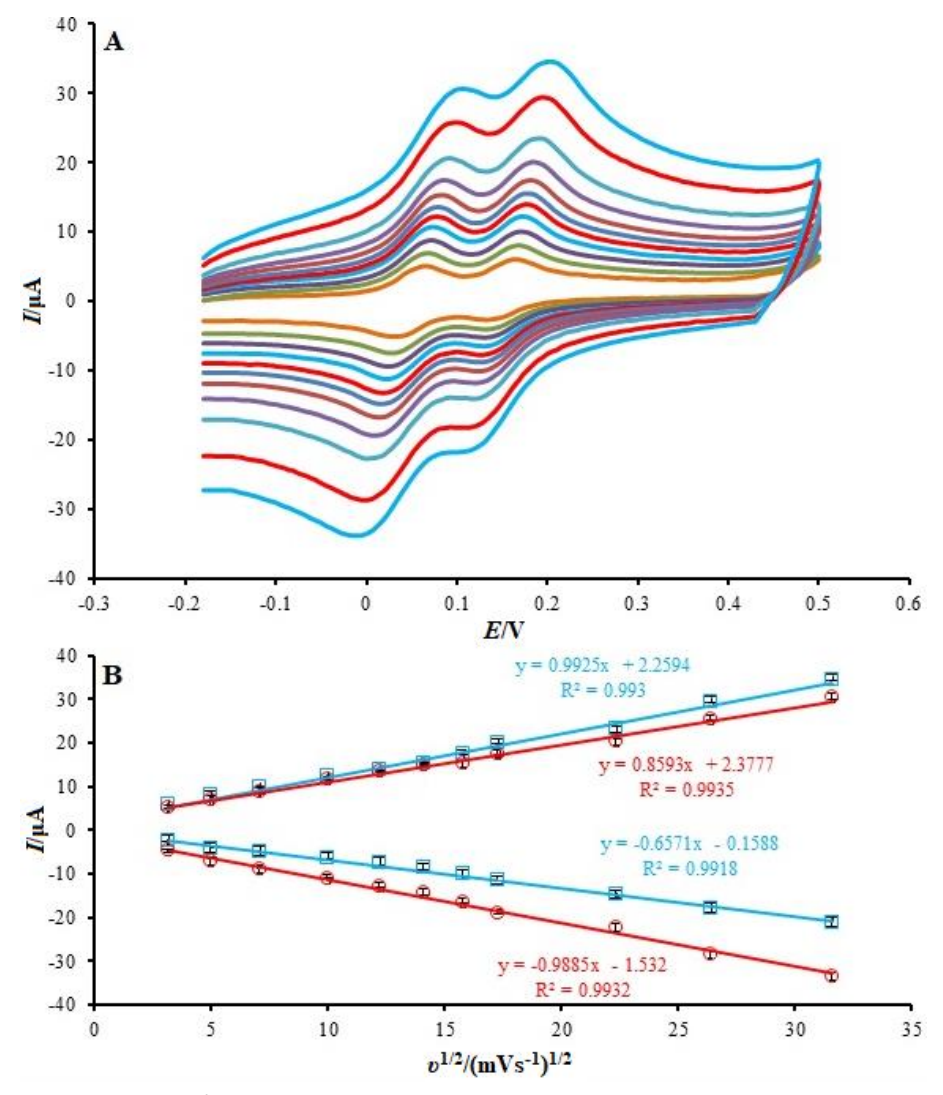


Figure 5. (A) CVs of GCE/GO-LaMnO₃ electrode in pH 5 in the presence of HQ and CT (100.0 μ M of each) at various scan rates (from inner to outer curve): 10, 25, 50, 100, 150, 200, 250, 300, 500, 700 and 1000 mV s⁻¹. (B) Plots of oxidation and reduction peak currents vs. $v^{1/2}$.

Interference studies

As dihydroxybenzene isomers usually coexist in real samples, it is very important to study the interference of each other for the selective detection of the single one species. In each experiment, the concentration of one species was changed, while the concentration of the other one was kept

constant. The results are shown in Figure 6. It can be seen from Figure 6(A) that the oxidation peak current of HQ increased with an increase in the concentration of HQ, while the peak current for the oxidation of CT remained constant. The same is seen in Figure 6(C) for the voltammetric peak corresponding to the oxidation of CT. This peak increased linearly with the increase of CT concentration, whereas the peak current for the oxidation of HQ remained constant. The results presented in Figure 6 (B and D) show that peak currents are linearly proportional to the concentration of HQ and CT, respectively. The fact that by changing concentration of one species, the peak current value of the other species did not change, indicates that oxidations of HQ and CT at GO-LaMnO₃ modified GCE take place independently.

Interference of some other species on determination of HQ and CT was investigated by the addition of interfering species (foreign compounds) into a solution containing 40.0 μ M of HQ and CT and the effects on the electrode recovery are shown in Table 1. It is clear that all kinds and amounts of interfering species (expressed as ratios between foreign compounds and HQ and CT) did not cause effects on currents being higher than ± 5 %.

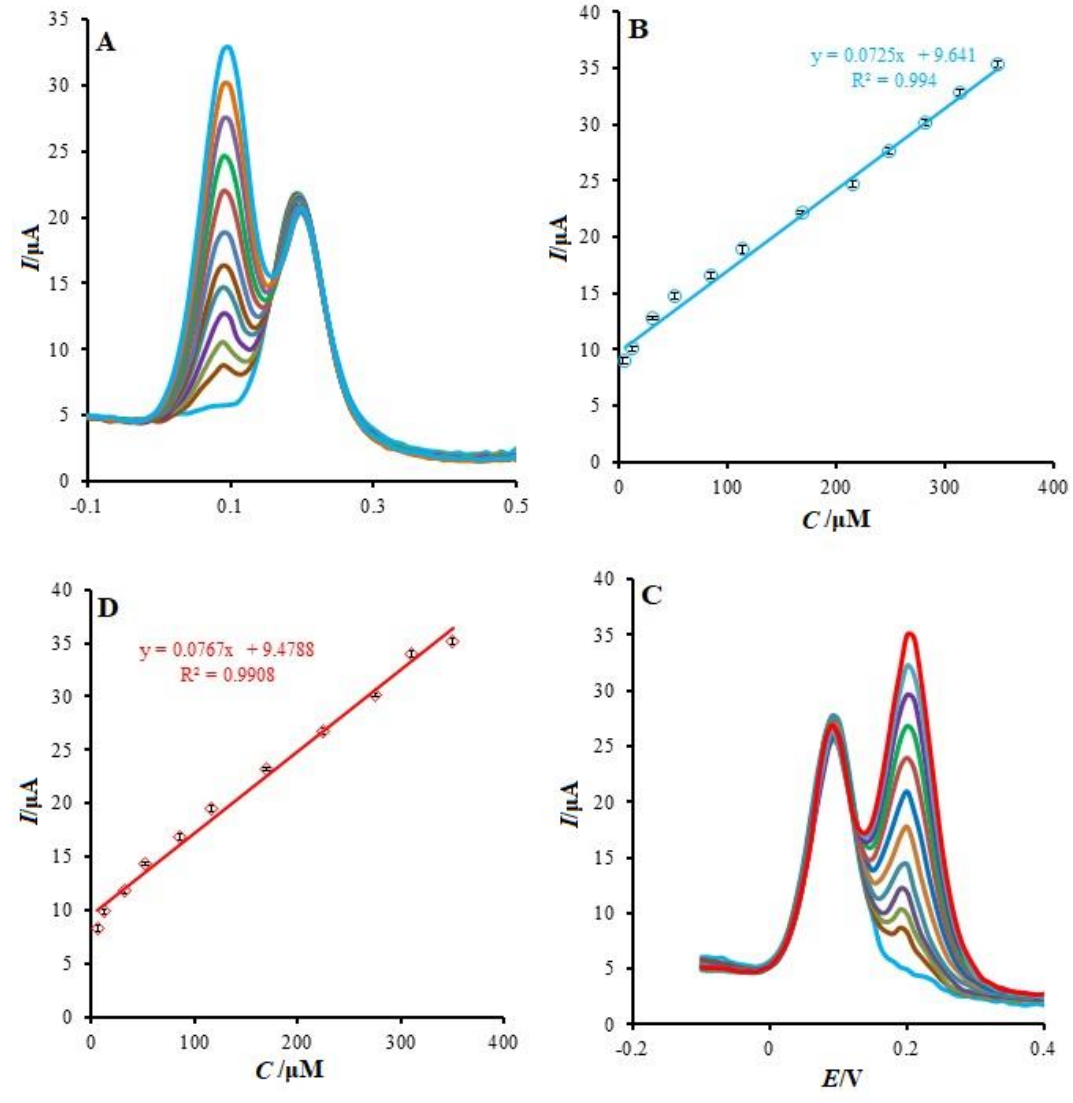


Figure 6. DPV at the GCE/GO–LaMnO₃ electrode in PBS (0.1 M pH 5) (A) containing CT (166.6 μM) and different concentrations of HQ (from inner to outer): 0.0, 6.6, 13.3, 33.3, 53.3, 86.6, 116.0, 170.0, 216.6, 250.0, 283.3, 316.0 and 350.0 μM. (C) HQ (233.3 μM) and different concentrations of CT (from inner to outer): 0.0, 6.6, 13.3, 33.3, 53.3, 86.6, 116.0, 170.0, 225.0, 275.0, 310.0 and 350.0 μM. Plots of peak current vs. concentration of (B) HQ and (D) CT.

Foreign compound Molar ratio of foreign compound/HQ and CT Recovery, % K+ (12 mM) 300.0 98.2 Ca^{2+} (8 mM) 200.0 97.3 Zn²⁺ (12 mM) 300.0 96.0 Fe²⁺ (10 mM) 250.0 98.0 Cl- (12 mM) 300.0 99.4 NO_{3}^{-} (16 mM) 400.0 98.0 Ascorbic acid (8 mM) 200.0 95.7 Urea (12 mM) 96.9 300.0

Table 1. Effect of interferences on determination of HQ (40.0 μ M) and CT (40.0 μ M).

Simultaneous determination of HQ and CT

Differential pulse voltammetry (DPV) was performed to investigate the relationship between the peak current value and concentration of HQ and CT. As shown in Figure 7, DPV curves showed two well distinguished oxidation peaks. Electrocatalytic peak currents of HQ and CT oxidation at the surface of GCE/GO-LaMnO $_3$ are linearly dependent on HQ and CT concentrations over the range of 0.5–433.3 and 0.5–460.0 μ M, respectively. Detection limit was obtained 0.06 and 0.05 μ M for HQ and CT, respectively. For 7 successive determinations of 100.0 μ M of HQ and CT, the relative standard deviations were 2.2 % and 1.9 %, respectively. These results show that the proposed electrode can be used effectively for the simultaneous determination of HQ and CT. Comparison of here obtained results using GCE/GO-LaMnO $_3$ electrode with the results obtained using other modified electrodes is presented in Table 2.

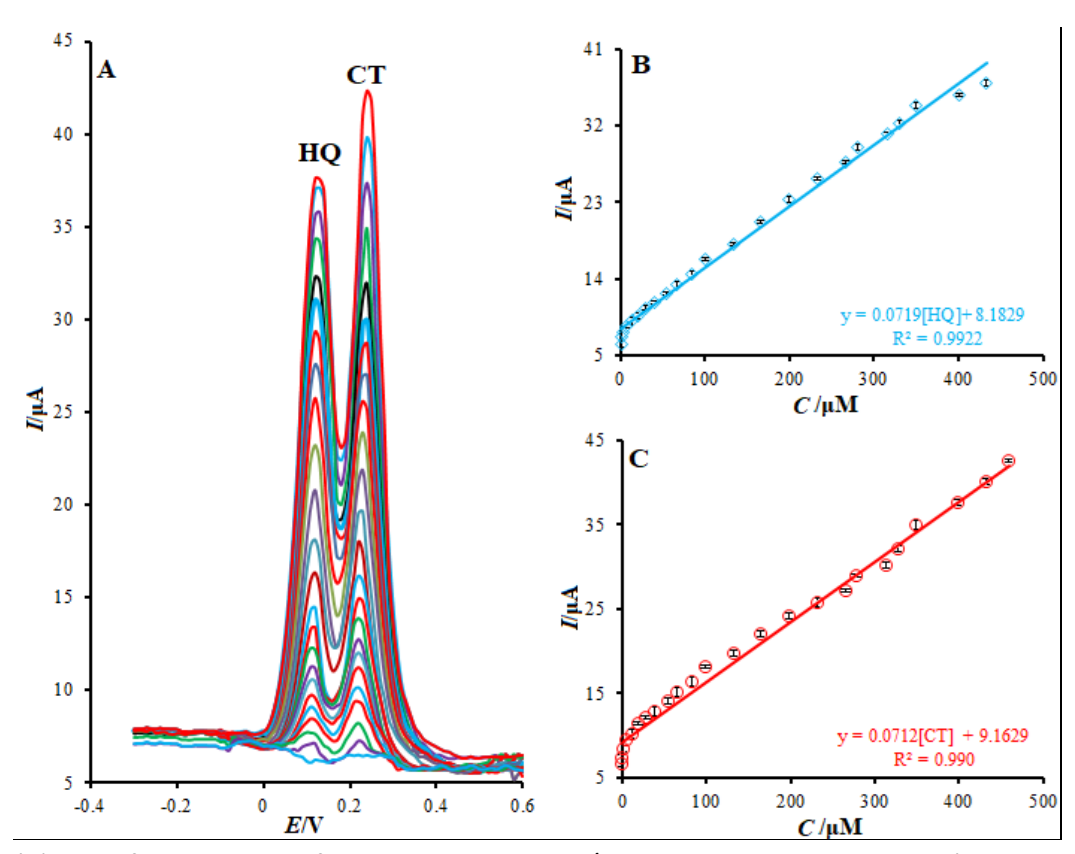


Figure 7. (A) DPV of the mixtures of HQ and CT at the GCE/GO–LaMnO $_3$ electrode in PBS (0.1 M pH 5) at the scan rate of 100 mV s $^{-1}$. Concentrations from inner to outer of curves: (0.0, 0.5, 1.5, 2.0, 3.0, 6.6, 13.3, 20.0, 30.0, 40.0, 55.0, 66.6, 85.0, 100.0, 133.3, 166.6, 200.0, 233.3, 266.6, 280.0, 316.6, 330.0, 350.0, 400.0, 433.3 and 460.0). (B) and (C): Plots of oxidation peak current vs. concentration.

Linear range, µM Detection limit, µM Modifier Ref HQ CT HQ CT 3-447 Pt-MnO₂ 15-4481 [26] MWNTs-P3MTa/GCE 0.5-150 0.5-150 0.05 0.05 [28] Gold-Graphene 1-100 1-100 0.2 0.15 [31] RGOb-MWCNT 5.5-540 1.8 8-391 2.6 [47] 0.8-100 0.8-100 0.2 [48] Carbon nanoparticle chitosan 0.2 Imidazolium ionic liquid 1-500 1-400 0.4 0.17 [49] 0.8-500 Nb_2O_5 39.8-980 1.6 8.0 [50] Aminated glassy carbon 5-260 5-260 0.2 0.2 [51] Graphene oxide-LaMnO₃ 0.5-460.0 0.06 0.05 This work 0.5-433.3

Table 2. Performance comparison of GCE/GO-LaMnO₃ electrode for the simultaneous determination of HQ and CT with other modified electrodes.

Real sample analysis

In order to evaluate the analytical applicability of the developed method for simultaneous determination of HQ and CT, local tap and mineral waters were tested. The amounts of HQ and CT in the tap (Kerman drinking water, Kerman, Iran) and mineral (Damavand mineral water Co., Iran) water samples were determined. The reliability of the method was checked by the analysis of the samples spiked with the known amount of HQ and CT. The results are listed in Table 3. The recoveries were 95.4–102.5 % for HQ and CT. Therefore, a capability of the proposed electrode for the simultaneous determination of HQ and CT is clearly confirmed.

Sample	Analyte		Docovery 0/		
		Detected	Added	Founda	Recovery, %
Tap water ^b	HQ	ND ^c	20	19.4±0.8	97.0
			30	28.6±1.0	95.4
	СТ		20	20.5±0.8	102.5
			30	29.2±1.2	97.4
Mineral water ^d	HQ	ND ^c	30	28.8±1.3	96.0
	CT	NDc	30	29 1+1 0	97.0

Table 3. Determination of HQ and CT in water samples using GCE/GO-LaMnO₃ (n = 5).

Stability of modified electrode

Long term stability of modified electrode, GCE/GO–LaMnO₃, was assessed for a period of three weeks, when the modified electrode was stored at atmosphere conditions. DPVs showed that there were no significant variations in regard to HQ and CT oxidation peak potential values, with the exception of a drop less than 2.8 % and 2.3 % in comparison to the primary response. The adjusted electrode oxidation antifouling capacity pertaining to HQ and CT and relevant oxidation byproducts were examined via DPV evaluation.

Conclusions

For the first time, we have demonstrated an effective approach to construct of GCE/GO-LaMnO₃ sensor and its application for simultaneous determination of HQ and CT. Compared with the bare GCE, a large peak-to-peak separation between CT and HQ, and the significant increase of peak

^aPoly (3-methylthiophene); ^bReduced graphene oxide

^aMean ± standard deviation for n = 5; ^bKerman drinking water, Kerman, Iran; ^cNot detected; ^dDamavand mineral water Co., IRAN;

current values were observed for GCE/GO-LaMnO $_3$, which clearly demonstrated that GO-LaMnO $_3$ could be used as an efficient promoter to enhance the kinetics of the electrochemical process of HQ and CT. The optimization of the experimental conditions for differential pulse voltammetry yielded a detection limit for HQ and CT of 0.06 and 0.05 μ M, respectively. These values are comparable or even better than those already described in the literature. In addition, the presented sensor was applied for the simultaneous determination of HQ and CT in water samples with satisfactory results.

Acknowledgment: This project was supported by Islamic Azad University, Kerman branch.

References

- [1] S. L. Mu, Biosensors and Bioelectronics **21** (2006) 1237-1243.
- [2] T. Xie, Q. Liu, Y. Shi, Q. Liu, Journal of Chromatography A 1109 (2006) 317-321.
- [3] J. Bai, L.P. Guo, J. Ndamanisha, Journal of Applied Electrochemistry 39 (2009) 2497-2502.
- [4] Iarc Working Group, Monographs on the Evaluation of Carcinogenic Risks to Humans, **71** (1999) 433.
- [5] K. Hirakawa, S. Oikawa, Y. Hiraku, I. Hirosawa, S. Kawanishi, *Chemical Research in Toxicology* **15** (2002) 76-82.
- [6] S. Dong, L. Chi, Z. Yang, P. He, Q. Wang, Y. Fang, Journal of Separation Science 32 (2009) 3232-3238.
- [7] G. Marrubini, E. Calleri, T. Coccini, A. Castoldi, L. Manzo, Chromatographia 62 (2005) 25-31.
- [8] A. Asan, I. Isildak, *Journal of Chromatography A* **988** (2003) 145-149.
- [9] M. F. Pistonesi, M. S. D. Nezio, M. E. Centurin, M. E. Palomeque, A.G. Lista, B. S. F. Band, *Talanta* **69** (2006) 1265-1268.
- [10] S. C. Moldoveanu, M. Kiser, Journal of Chromatography A 1141 (2007) 90-97.
- [11] H. Cui, Q.L. Zhang, A. Myint, X. W. Ge, L. J. Liu, *Journal of Photochemistry and Photobiology* **181** (2006) 238-245.
- [12] J. A. Garcia-Mesa, R. Mateos, J. Agric, Food Chemistry **55** (2007) 3863-3868.
- [13] I. C. Eleotério, M. Aantonio Balbino, J. F. de Andrade, B. Ferreira, A. Aparecida Saczk, L. Luiz Okumura, A. C. Ferreira Batista, M. F. de Oliveira, *Journal of Electrochemical Science and Engineering* **8** (2018) 281-289.
- [14] M. M. Foroughi, Sh. Jahani, H. Hasani Nadiki, Sensors and Actuators B 285 (2019) 562-570.
- [15] K. Roja, P. R. Prasad, P. Sandhya, N. Y. Sreedhar, *Journal of Electrochemical Science and Engineering* **6** (2016) 253-263.
- [16] H. Maaref, M. M. Foroughi, E. Sheikhhosseini, M.R. Akhgar, *Analytical and Bioanalytical Electro-chemistry* **10** (2018) 1080-1092.
- [17] M. M. Foroughi, M. Noroozifar, M., Khorasani-Motlagh, *Journal of the Iranian Chemical Society* **12** (2015) 1139-1147.
- [18] Sh. Jahani, Analytical and Bioanalytical Electrochemistry 10 (2018) 739-750.
- [19] M. M. Foroughi, H. Beitollahi, S. Tajik, M. Hamzavi, H. Parvan, *International Journal of Electrochemical Science* **9** (2014) 2955-2965.
- [20] H. Yaghoubian, Sh. Jahani, H. Beitollahi, S. Tajik, R. Hosseinzadeh, P. Biparva, *Journal of Electro-chemical Science and Technology* **9** (2018) 109-117.
- [21] M. Rajaei, M.M. Foroughi, Sh. Jahani, M. Shahidi Zandi, H. Hassani Nadiki, *Journal of Molecular Liquids* **284** (2019) 462-472.
- [22] M. Baniasadi, Sh. Jahani, H. Maaref, R. Alizadeh, *Analytical and Bioanalytical Electrochemistry* **9** (2017) 718-728.
- [23] M. Salajegheh, M. Ansari, M.M. Foroghi, M. Kazemipour, *Journal of Pharmaceutical and Biomedical Analysis* **162** (2019) 215-224.
- [24] R. Torkzadeh-Mahani, M.M. Foroughi, Sh. Jahani, M. Kazemipour, H. Hassani Nadiki, *Ultrasonic Sonochemistry* **56** (2019) 183-192.
- [25] J. G. Redepenning, *TrAC Trends* in *Analytical Chemistry* **6** (1987) 18-22.
- [26] S. Feng, Y. Zhang, Y. Zhong, Y. Li, S. Li, Journal of Electroanalytical Chemistry 733 (2014) 1-5.
- [27] B. Unnikrishnan, P.Ru, S. Chen, Sensors and Actuators B 169 (2012) 235-242.
- [28] H. Zhang, J. Zhao, H. Liu, R. Liu, H. Wang, J. Liu, Microchimica Acta 169 (2010) 277-282.

- [29] L. Wang, P. Huang, J. Bai, H. Wang, L. Zhang, Y. Zhao, Microchimica Acta 158 (2007) 151-157.
- [30] M. Li, F. Ni, Y. Wang, S. Xu, D. Zhang, S. Chen, L. Wang, *Electroanalysis* **21** (2009) 1521-1526.
- [31] X. Ma, Z. Liu, C. Qiu, T. Chen, H. Ma, *Microchimica Acta* **180** (2013) 461-468.
- [32] Y. Ma, Y. Tang, K. Yin, S. Luo, C. Liu, T. Liu, L. Yang, *Journal of Electrochemical Science and Engineering* **7** (2017) 201-212.
- [33] C. Z. Zhu, L. Han, P. Hu, S. J. Dong, *Nanoscale* **4** (2012) 1641-1646.
- [34] K. Roja, P. Reddy Prasad, P. Sandhya, N. Yugandhar Sreedhar, *Journal of Electrochemical Science and Engineering* **6** (2016) 253-263.
- [35] R. Li, T. Yang, Z. Li, Z. Gu, G. Wang, J. Liu, Analytica Chimica Acta 954 (2017) 43-51.
- [36] F. Y. Li, J. J. Zhao, Z. F. Chen, Journal of Physical Chemistry C 116 (2012) 2507-2514.
- [37] C. Nethravathi, M. Rajamathi, N. Ravishankar, L. Basit, C. Felser, *Carbon* 48 (2010) 4343-4350.
- [38] X. Q. Yin, T. S. Jiang, Q. Zhao, H. B. Yin, Journal of Materials Science 47 (2012) 1026-1032.
- [39] D. M. Smyth, Ferroelectrics **380** (2009) 1-13.
- [40] F. Lichtenberg, A. Herrnberger, K. Wiedenmann, *Journal of Solid State Chemistry* **36** (2008) 253-387.
- [41] P. K. Panda, Journal of Materials Science 44 (2009) 5049-5062.
- [42] A. Dutta, T. Ishihara, H. Nishiguchi, *Chemistry of Materials* **16** (2004) 5198-5204.
- [43] A. Orera, P.R. Slater, Chemistry of Materials 22 (2010) 675-690.
- [44] Y. Yang, Y.B. Sun, Y.S. Jiang, *Materials Chemistry and Physics* **96** (2006) 234-239.
- [45] M. Khorasani-Motlagh, M. Noroozifar, Sh. Jahani, *Synthesis and Reactivity in Inorganic and Metal-Organic Chemistry* **45** (2015) 1591-1595.
- [46] A. J. Bard, L. R. Faulkner, *Electrochemical Methods: Fundamentals and Applications*, second ed., Wiley, New York, (2001).
- [47] F. Hu, S. Chen, C. Wang, R. Yuan, D. Yuan, Analytica Chimica Acta 724 (2012) 40-46.
- [48] M. Amiri, S. Ghaffari, A. Bezaatpour, F. Marken, Sensors and Actuators B 162 (2012) 194-200.
- [49] X. Feng, W. Gao, S. Zhou, H. Shi, H. Huang, W. Song, Analytica Chimica Acta 805 (2013) 36-44.
- [50] T. C. Canevari, L. T. Arenas, R. Landers, R. Custodio, Y. Gushikem, *Analyst* 138 (2013) 315-324.
- [51] X. Wang, M. Xi, M. Guo, F. Sheng, G. Xiao, S. Wu, S. Uchiyama, H. Matsuura, *Analyst* **141** (2016) 1077-1082.



Open Access: ISSN 1847-9286

www.jESE-online.org

Original scientific paper

Principles of the express method for controlling interelectrode space condition during wire electrochemical processing

Vasyl Osypenko, Oleksandr Plakhotnyi[™] and Oleksii Timchenko

Cherkasy State Technological University, Cherkasy, 18006, Ukraine

Corresponding author: [™]o.plakhotny@chdtu.edu.ua

Received: February 3, 2019; Revised: June 26, 2019; Accepted: June 27, 2019

Abstract

In the practical implementation of the sequential wire electrical discharge machining – pulsed electrochemical machining (WEDM – PECM) technology and in order to perform high quality electrochemical processing, there is a need for the real-time operational control of electrical parameters of inter-electrode space and corresponding adaptive correction of amplitude-frequency power supply parameters (AFPSP). In the context presented by the authors, a mathematical apparatus and an algorithm of operational galvanostatic mode monitoring of anode dissolution using wire electrode-tool are proposed. This will allow adaptive adjustment of AFPSP to ensure controlled passage of electrochemical reactions and significantly increase process stability, dissolved surface layer thickness uniformity along entire electrode tool movement trajectory and resulting surface quality.

Keywords

Wire electrical discharge machining; pulsed electrochemical machining; current and voltage waveforms; process monitoring; surface finishing.

Introduction

Wire electrical discharge machining (WEDM) technology fully satisfies the requirements of modern production in terms of miniaturization and precision. However, modern industry and especially instrumental production require electrical discharge wire cutting machines to form surfaces with roughness Ra < 0.1 microns. Obtaining such surface parameters and getting rid of a structurally modified heat affected zone (HAZ) using only material removal by a highly concentrated source of heat having a spark discharge is extremely costly and difficult. In modern machines of the world leader in the field of electrical discharge nanotechnology, Sodick Co. LTD, a mirror-like smoothing of steel blank surfaces of up to 0.08 microns is achieved in 12 passes with a change of working environment. This leads to an unacceptable cost increase of machined parts.

Pulse electrochemical machining (PECM) principally allows obtaining surfaces with roughness *R*a < 0.1 microns with the absence of a structurally altered layer on the workpiece surface. However, implementation of an efficient PECM process by a mobile wire tool electrode (WTE) following to the WEDM technology scheme is currently not sufficiently researched and is challenging in scientific and technical terms. The solution requires complex experimental and theoretical studies, as well as mathematical and physical modelling of basic processes that determine the nature of the electrochemical dissolution of the anode surface obtained by WEDM.

Literature review and problem statement

For WEDM, the express methods of preliminary determination of power supply parameters and inter-electrode space (IES) condition monitoring in real time are already developed and successfully used on serial machines. The IES resistance is controlled by the hardware. AFPSP and machine drives feed rate have adaptive control. More sophisticated modern schemes are implemented through the continuous supply of low-power diagnostic impulses to IES. By analysing the response, a decision is made to switch on a more powerful source of pulsed technological current, which in fact, carries the electro-discharge destruction of material [1,2].

For wire PECM, such control methods have not been developed. The time of periodic process of double layer charging to the overvoltage activation and its discharge time are very important for nanosecond pulsed electrochemical processing [3-5]. Cylindrical wire electrode causes significant current density distribution on the anode surface. Therefore, even a slight change in electrode potential leads to a significant change in current density and accordingly, to dissolution localization. With a longer duration of microsecond pulses, a diffusion processes becomes a limiting factor in IES. Accordingly, calculation of stationary and transition components of diffusion current, which depend on main parameters of each technological PECM scheme, must be preceded by the choice of current amplitude [6]. For configuration of flat anode and cylindrical cathode with stream electrolyte flow, it is problematic to determine diffusion layer thickness, which depends on velocities distribution of electrolyte in near-anode zone. Consequently, calculated mathematical models of electrochemical processes in IES are complex, require usage of computer-aided design software and significant computational time [7]. These mathematical models are adequate for preliminary calculation of PECM processes parameters but are not suitable for operational monitoring and adaptive real-time correction. Therefore, there is an urgent need for the creation of algorithms and schemes suitable for practical implementation in the existing technological equipment.

The proposed approach is based on the determination of magnitude and dynamics change of IES electrical parameters and as a result, process nature of electrochemical dissolution. These can be obtained from analysis of response oscillograms using equivalent electrical circuit substitution scheme. A similar approach was used in [8], using a complex mathematical apparatus not suitable for operative quantitative analysis of response oscillograms. In the subsequent work [9] only a qualitative analysis of oscillograms was conducted.

Proper choice of AFPSP according to PECM scheme, can significantly improve surface quality, machining accuracy, material removal rate and overall process controllability [10,11].

The purpose is to increase the technological characteristics of high-performance combined methods of current-conducting materials machining with the help of further development of mathematical apparatus of operational monitoring and adaptive efficiency correction of galvanostatic PECM mode.

Experimental equipment and methods

Technological scheme

When using the PECM scheme of unipolar current pulses with moving WTE as a cathode (Figure 1), developed by the authors and implemented in particular experimental technological equipment, the process of anodic dissolution of workpiece material significantly depends on the magnitude and growth dynamics of anode polarization and relaxation of its potential during the pause between current pulses.

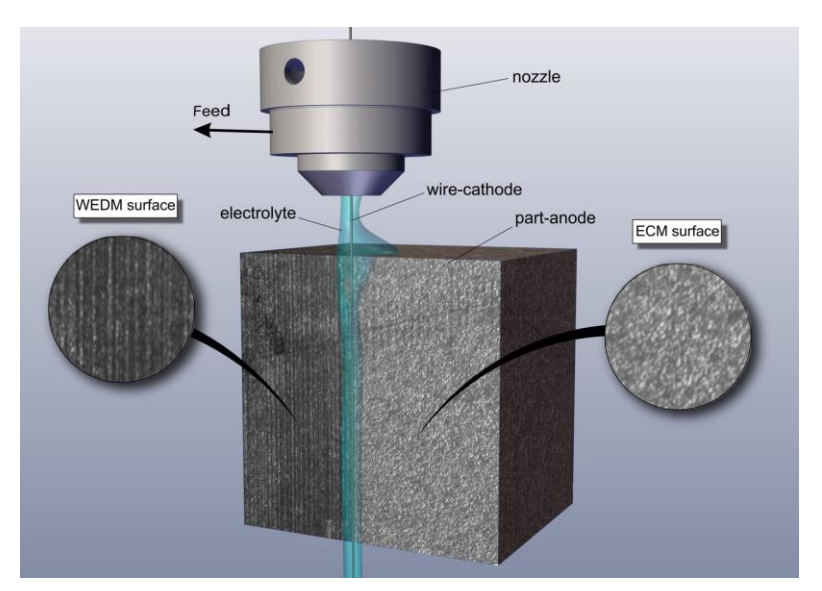


Figure 1. Machining scheme of sequential wire EDM and wire PECM

Replacement of the partition boundary "anode – electrolyte" for equivalent electrical circuit (Randles circuit) is carried out and described in Figure 2 [8,12]. The choice of circuit should be based on electrical properties of IES. Technological parameters during machining process determine dynamics change of electrical properties of IES. Electrolyte flow speed (renewal rate) influences R_E – electrolyte resistance. Change of IEG value, a size of interacting surface while moving on intricate-contoured trajectory affects capacity. WTE feed rate along trajectory alters dissolution conditions of EDM-affected surface layers and influences the electrical properties of IES.

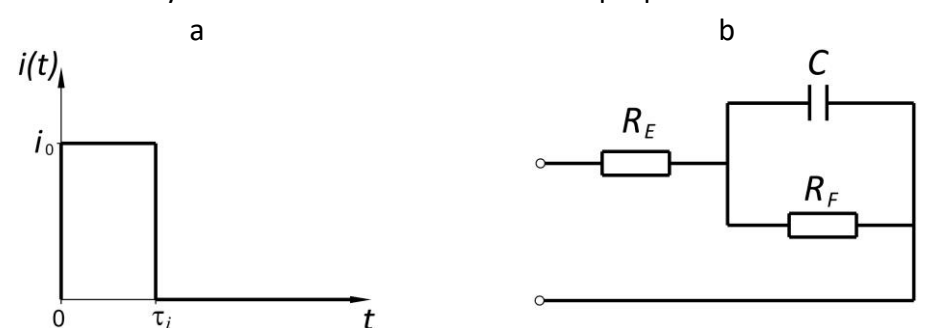


Figure 2. a - Current pulse parameters; **b** - Electrical equivalent scheme for anode-electrolyte boundary interface of pulse ECM (PECM): R_E – electrolyte resistance; C – double layer capacity; R_F – Faraday resistance

Methods for obtaining oscillograms of anode current pulses are well worked out and have a relatively simple scheme implementation (Figure 3) [8,13].

Research of physical and technological parameters of wire cutting electrical discharge machining and subsequent electrochemical processing by a wire electrode was carried out on SELD-02 (wire-cut

electrical discharge machine on linear motors, Ukraine). SELD-02 machine has linear motors, granite guides and gas-lubricated supports. This provides minimal displacement error.

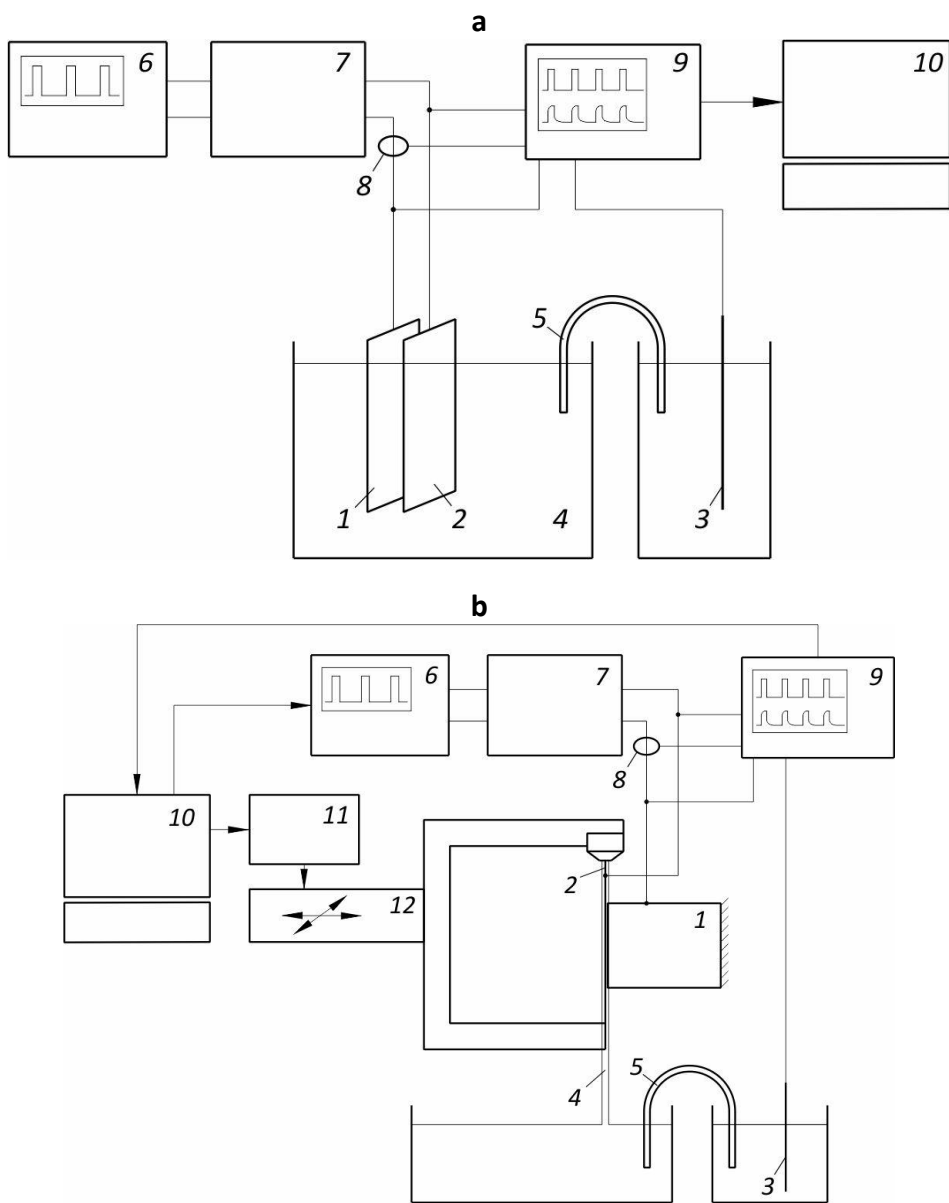


Figure 3. Schemes of measurements: a - flat electrodes, b - flat anode – cylindrical (wire) cathode. 1 – anode, 2 – cathode, 3 – reference electrode (platinum), 4 – electrolyte, 5 – bridge, 6 – driving pulse generator, 7 – current source, 8 – current transducer, 9 – oscillograph, 10 – computer, software, 11 – computer numerical control unit, 12 – positioner

Experimental conditions: anode – stamping steel DIN X155CrVMo12-1, cathode – 0.2 mm diameter Cobra Cut B wire (AGIE, Switzerland), CuZn37 hard brass, 1 M NaCl electrolyte at temperature of 28 °C which was delivered as a jet from the upper chamber of the machine at pressure of 5×10^4 Pa. Height of the part is 11 mm. The machine-tool provided wire electrode movement with a given speed along the trajectory at a given distance (IEG) from the machined surface. Conductivity of the electrolyte was controlled by the Oakton TDS-5/CON-5 with a special electrode which expands measurement scale (cell factor K = 10). Polarization-time and current-time dependencies were recorded by digital Atten ADS1000 dual-channel oscillograph and transmitted to computer in a mathematical software package for processing.

Preliminary testing of the proposed method for monitoring IES was carried out in studies of transient processes in electrochemical system. It had fixed flat electrodes and the process was

conducted by the passing of a sequence of rectangular current pulses. Electrodes $20 \times 12.5 \times 1.5$ mm were immersed in a bath with immovable 1 M NaCl electrolyte, so the electrodes interaction area was 2.5 cm^2 . Anode material – stamping steel DIN X155CrVMo12-1, cathode – brass CuZn37.

Mathematical method for calculating parameters of an electric circuit loaded by microsecond current pulses

As is known, current i(t) and voltage u(t) at the ends of an electrical circuit element with active resistance R and capacity C are bound by formula [14]

$$u(t) = R \cdot i(t), \qquad u(t) = \frac{1}{C} \left[\int_{0}^{1} i(t) dt + q_{0} \right]$$

$$\tag{1}$$

where q_0 – initial charge on condenser covers.

Using the operational method [14], we introduce an integral transform of Laplace's "operational current", $i(t) \rightarrow I(p)$ and "operational voltage", $u(t) \rightarrow U(p)$, where p is a complex number frequency parameter. Then, relation (1) will be converted into operational formulas

$$U = RI, \quad U = \frac{1}{Cp}I \tag{2}$$

if we consider $q_0 = 0$.

Formulas (2) combine into "operational Ohm's law "

$$U = ZI \tag{3}$$

where Z is "operational resistance" or impedance, which in the case of active resistance and capacitance has the following form:

$$Z_R = R, \qquad Z_C = \frac{1}{Cp} \tag{4}$$

Considering rules for adding parallel and serial impedances, we obtain the expression for the overall circuit (Figure 2b) impedance,

$$Z = R_{\rm E} + \frac{R_{\rm F}}{C\rho R_{\rm E} + 1} \tag{5}$$

and the operational equation, respectively:

$$U = \left(R_E + \frac{R_F}{CpR_F + 1}\right)I \tag{6}$$

Similarly, it is possible to formulate the operational equation for more complex electric substitution schemes taking into account additional components of inter-electrode space, such as cathode double electrical layer capacitance, resistance of passivating films that can be formed on surface of electrodes, *etc.* Also, in the substitution scheme, inductivities can be introduced if response oscillograms taken from IES clearly indicate oscillatory attenuation signals and model must reproduce them. It is important to substantiate the conformity of each element of electrical circuit and way of its connection to the real processes occurring in IES during electrochemical machining.

To construct a mathematical description of the passage of a rectangular current pulse through a model of an electrochemical cell (Figure 2b), we first consider the problem of DC current i_0 activation at time t = 0.

$$i(t) = i_0 \theta(t), \quad \theta(t) = \begin{cases} 0, & \text{if } t < 0, \\ 1, & \text{if } t \ge 0; \end{cases}$$

 $\theta(t)$ – Heaviside function.

Operational current is defined as $I = i_0/p$, while the operational voltage according to Eqs. (3) and (6) is defined as:

$$U = \left(R_E + \frac{R_F}{C\rho R_F + 1}\right) \frac{i_0}{\rho} \tag{7}$$

We perform the transition operation to the original $u(t) \leftarrow U(p)$ started using the conclusion of the second expansion theorem [14], according to formula

$$\frac{A(p)}{pB(p)} \to \frac{A(0)}{B(0)} + \sum_{k=1}^{k=l} \frac{A(p_k)}{p_k B'(p_k)} e^{p_k t}$$
(8)

where $p_k - k^{th}$ equation root of B(p) = 0.

In our case, using Eq. (7) we have only one root, $p_1 = 1/CR_F$. Then using Eq. (8)

$$\frac{A(p)}{pB(p)} \rightarrow (R_E + R_F)i_0 - R_Fi_0e^{\rho_1t}$$

u(t) becomes defined as:

$$u(t) = i_0 [R_F + R_F (1 - e^{\rho_1 t})]$$
(9)

Next, to get response function to the rectangular shape current pulse passage, $i(t) = i_0 \theta(t) - i_0 \theta(t - \tau_i)$, where τ_i is pulse duration, the lag theorem [14] was used and we get:

$$u(t) = i_0 \{ [R_E + R_F (1 - e^{\rho_1 t})] \theta(t) - [R_E + R_F (1 - e^{\rho_1 (t - \tau_i)})] \theta(t - \tau_i) \}$$
(10)

Here it is assumed that electrochemical cell parameters R_E , R_F , C have not changed during pulse duration.

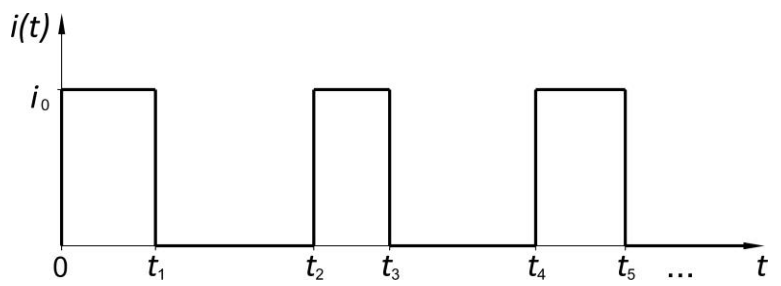


Figure 4. Sequence of current pulses with arbitrary parameters of duration and on-off time

For a series of current pulses with an arbitrary time duration and on-off time parameters (Figure 4), it is suitable to use the following form of the response function

$$u(t) = i_{0} \{ [R_{E1} + R_{F1}(1 - e^{\rho_{1}t})] \theta(t) - [R_{E2} + R_{F2}(1 - e^{\rho_{2}(t - t_{1})})] \theta(t - t_{1}) + \\ + [R_{E3} + R_{F3}(1 - e^{\rho_{3}(t - t_{2})})] \theta(t - t_{2}) - [R_{E4} + R_{F4}(1 - e^{\rho_{4}(t - t_{3})})] \theta(t - t_{3}) + \\ + [R_{E5} + R_{F5}(1 - e^{\rho_{5}(t - t_{4})})] \theta(t - t_{4}) - [R_{E6} + R_{F6}(1 - e^{\rho_{6}(t - t_{5})})] \theta(t - t_{5}) + \\ + \dots \},$$

$$(11)$$

where according to the trend of parameters changing from R_{E1} , R_{F1} , C_1 to R_{E2} , R_{F2} , C_2 , then to R_{E3} , R_{F3} , C_3 , etc, it is possible to clearly observe dynamics of IES condition indicators for an electrochemical cell during pulsed current workload in the galvanostatic mode.

Results and discussion

Flat electrodes

Figure 5(a) presents the results of dynamic measurements of anode polarization at given amplitude-time parameters of current. It should be noted that amplitude of current pulses and interaction area of electrodes in this experiment do not correspond to the operating modes of current density of electrochemical dissolution using wire WEDM + PECM technology. Duration and amplitude of pulse current, area of interaction of electrodes, IEG value were selected in such a way to maximize manifestation of IES resistance and capacity in anodic polarization curves. In addition, oscillograms were recorded at the beginning of dissolution process in order to minimize influence of external factors such as electrochemical reaction products saturation (slag) and IES gas pollution or formation of various films on electrodes, which had not yet appeared in a short time.

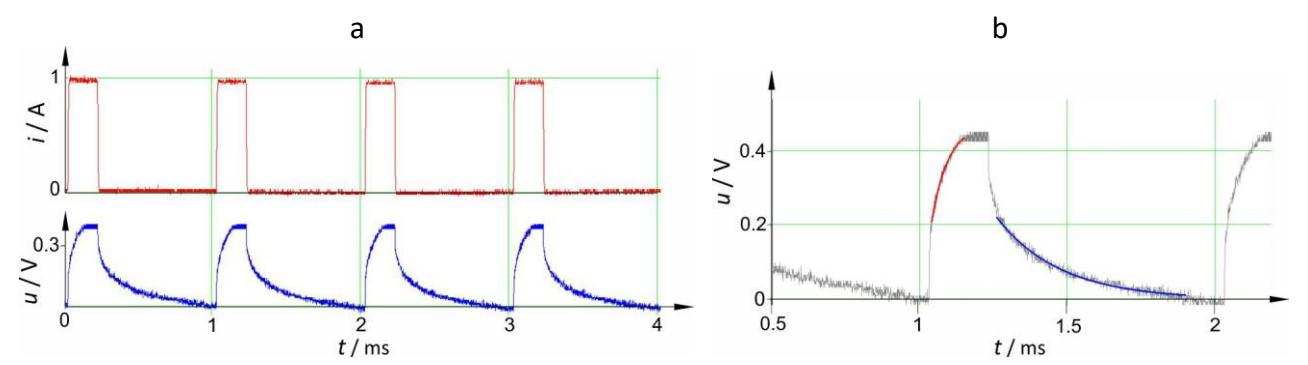


Figure 5. Oscillograms and their mathematical processing: **a** - rectangular current pulses (red curve); increase and decrease of anode polarization (blue curve); **b** - approximation by response function of areas with transient processes

Then, the inverse mathematical problem was solved using the experimentally obtained plot of polarization-time dependence, and selecting coefficients in the response function (Eq. (10)), *i.e.* parameters R_E , R_F , C of the electrical equivalent substitution scheme of an electrochemical cell. Polarization growth area (Figure 5b) was approximated by the least squares method using function (9), which is a response function when passing the front edge of current pulse through an electrochemical cell. The decrease of area which corresponds to the back edge of the switch-off of current pulse, was approximated by the function represented in the second term Eq. (10).

According to oscillogram processing results (Figure 5b), it was found that at the moment of passing the forward front of current pulse, IES parameters had following values: $R_E = 0.12$ Ohm, $R_F = 0.33$ Ohm, $C = 1.2 \cdot 10^{-4}$ F. At the moment of passing rear front, these values were: $R_E = 0.12$ Ohm, $R_F = 0.4$ Ohm, $C = 3.9 \cdot 10^{-4}$ F. Estimated total IES resistance, R, according to the Ohm's law

$$R = \frac{\delta}{\kappa S} \tag{12}$$

using values of electrolyte conductivity, $\kappa = 8.61 \text{ S m}^{-1}$, electrodes interaction area, $S = 2.5 \cdot 10^{-4} \text{ m}^2$ and IEG, $\delta = 0.8 \cdot 10^{-3}$ m, was 0.37 Ohm. Specific capacity of double electric layer *i.e.* capacity according to the equivalent interaction area of electrodes is 0.48 F/m² and 1.6 F/m² in the first and second case, respectively. According to the literature data, specific capacity values should be within 0.2-0.4 F/m² [15], Helmholtz model, 0.6-0.8 F/m²] [15], or 0.4-0.5 F/m² [16], measured at the boundary between mercury anode and 1M NaCl solution at 25 °C, 0<U<0.4 V. That is, the order of experimentally determined resistance values $R_E + R_F$ (values are adding for serial connection)

coincides with theoretical calculation. The found specific capacity value along the pulse forward front is located in well-known range. The rear edge determined capacity, however, is not correct (similar to [8]), so it is obvious that the electrical equivalent scheme needs to be clarified.

With an increase of the current amplitude up to 9 A and a decrease in of IEG value down to 0.6 mm, IES is filled with sludge over time due to reactions products. This is noticeable when analysing oscillograms (Figure 6). At the beginning of experiment, electrochemical cell specific capacities are 0.22 F/m² and 0.76 F/m² for forward and rear pulse fronts, respectively. After 2 minutes of the anode dissolution, a significant amount of sludge is observed visually in IES, and from analysing oscillograms it follows that the corresponding capacities increased to 0.49 F/m² and 1.2 F/m² and resistance decreased. Consequently, IES is filled by sludge, caused by insufficient rate of stationary electrolyte renewal that is clearly visible on the oscillograms and can be quantified by their mathematical analysis.

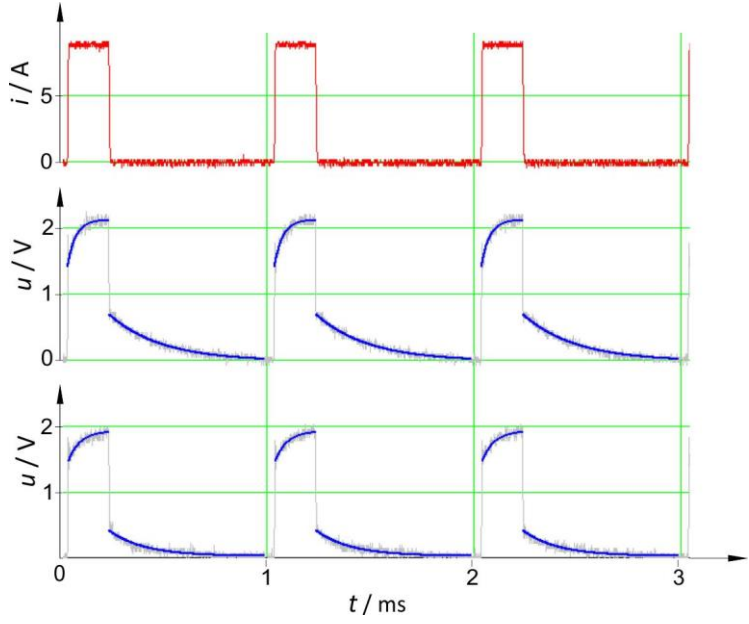


Figure 6. Oscillograms, approximated by response function, when working with a larger current amplitude 9A: voltage at the beginning of experiment – medium graph; voltage after 2 minutes of polluted IES – lower graph

With a variation of the IEG and AFPSP parameters, other characteristic cases of polarization change dynamics of electrodes were experimentally obtained. Oscillograms in Figure 7 are mathematically processed in the following way. On the first pulse, we obtain resistance and capacitance parameters of elements and using Eq. (11) further polarization change is predicted for several subsequent pulses (red curve).

In the first case (Figure 7a), an unsuccessful choice of AFPSP for experimental conditions led to increasing residual polarization. In another example (Figure 7b) there is an increase in polarization and a simultaneous change in IES conditions. Both cases are unacceptable and require an immediate correction of AFPSP for normalization of the anode dissolution process in electrochemical cell with flat electrodes. A novel pulsed-power supply method allows to accelerate depolarization and to improve the machining accuracy of PECM [17].

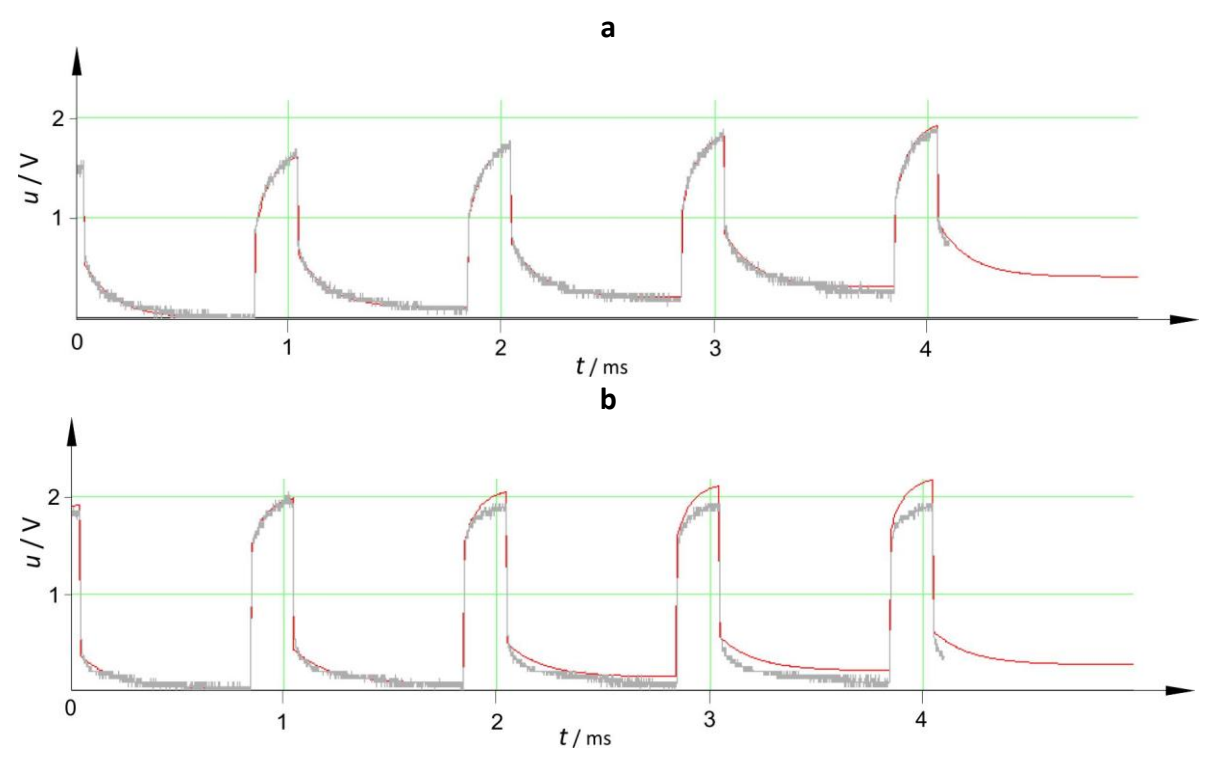


Figure 7. Oscillograms with (a) increasing residual polarization, (b) increasing polarization and changes in IEG characteristics

Flat anode – cylindrical cathode

For polarization oscillograms with flat anode and wire cathode analysis it is incorrect to use value of electrodes interaction area *S* in Eq. (12). To obtain more accurate quantitative results of oscillograms analysis, the following mathematical description of electric field distribution for the calculation scheme of flat anode – cylindrical cathode (Figure 8) [18,19] must be applied.

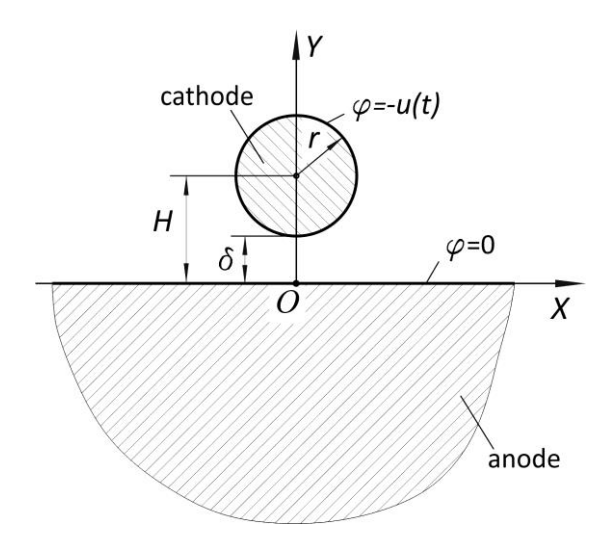


Figure 8. Scheme for electrochemical machining of flat anode by a wire cathode

If cathode potential is u(t), then field strength distribution on anode surface is determined by the formula

$$E_{y}(x,t)\Big|_{y=0} = \frac{2au(t)}{\ln p} \frac{1}{x^{2} + a^{2}}$$
 (13)

where $a = \sqrt{H^2 - r^2}$, $p = (a-\delta)/(a+\delta)$. Field strength component E_x is insignificant due to smallness.

Amplitude current in circuit can be described by the following equation

$$I_{A} = 2\int_{0}^{\infty} \kappa E_{y} \left| y = 0 \right| L dx = 2\pi L \kappa \frac{U_{A}}{\left| \ln p \right|}$$
(14)

where κ is specific electrolyte conductivity, and L is the part height.

Then IES resistance filled with electrolyte is

$$R = \frac{|\ln p|}{2\pi L\kappa} \tag{15}$$

or by analogy with Eq. (12)

$$R = \frac{a}{\kappa A_{s}} \tag{16}$$

where, $A_s = 2\pi\alpha L/|\ln p|i.e.$ equivalent interaction area for cylindrical cathode and flat anode, similar to the interaction area of electrodes S for flat electrodes.

The area of electrodes interaction, which in turn determines electrical capacity of electrochemical cell, has much less calculated value for a wire electrode than for a pair of flat electrodes. Therefore, transient processes of increasing and decreasing polarization under pulsed current are visually less obvious. Figure 9 depicts an oscillogram of anode polarization at IEG of 0.5 mm, amplitude current $I_A = 2.34$ A and voltage $U_A = 11$ V.

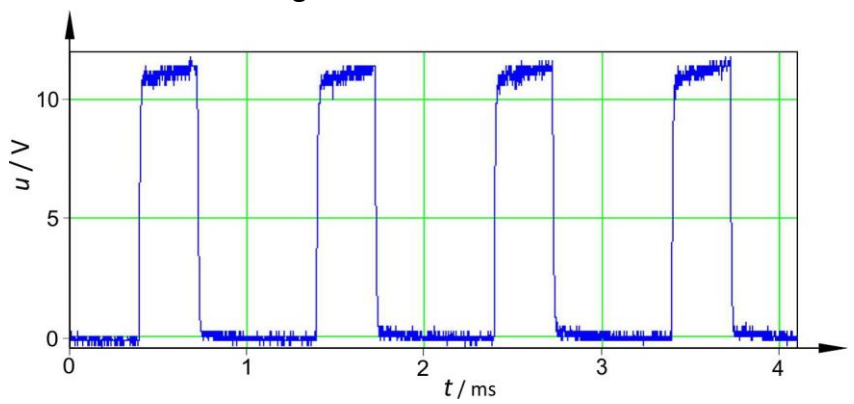


Figure 9. Oscillogram of anode polarization during electrochemical machining of flat anode by a wire cathode.

Figure 10 shows areas of voltage growth and decrease of oscillogram in Figure 9, approximated by the response function (Eq. 10). The experimental value of resistance is 4.7 Ohm, while the theoretically calculated value according to Eq. (15) is 4.33 Ohm. The difference between the experimental and theoretical results is 7.9 % and may be explained by the appearance of partial gas pollution of IES as a result of electrochemical reaction, which leads to a decrease in electrolyte conductivity.

Following the results of the response function approximation of forward pulse front, the following values were obtained: $R_E = 3.74$ Ohm, $R_F = 0.89$ Ohm, $C = 8.3 \cdot 10^{-6}$ F. Specific capacity, *i.e.* the capacity of electrochemical cell according to the equivalent interaction area of electrodes, is 0.5 F/m^2 . Data of the voltage drop area approximation asserts that specific capacity reached 0.45 F/m^2 .

With the prolongation of response function according to Eq. (11) with parameters obtained for several subsequent pulses and comparison with the oscillogram in Figure 9, it was established that electrochemical process proceeds normally, without significant changes in IES condition and without accumulation of residual polarization. That is, AFPSP for given conditions is selected correctly, providing necessary metal removal rate and avoiding a process of entering passivation zone.

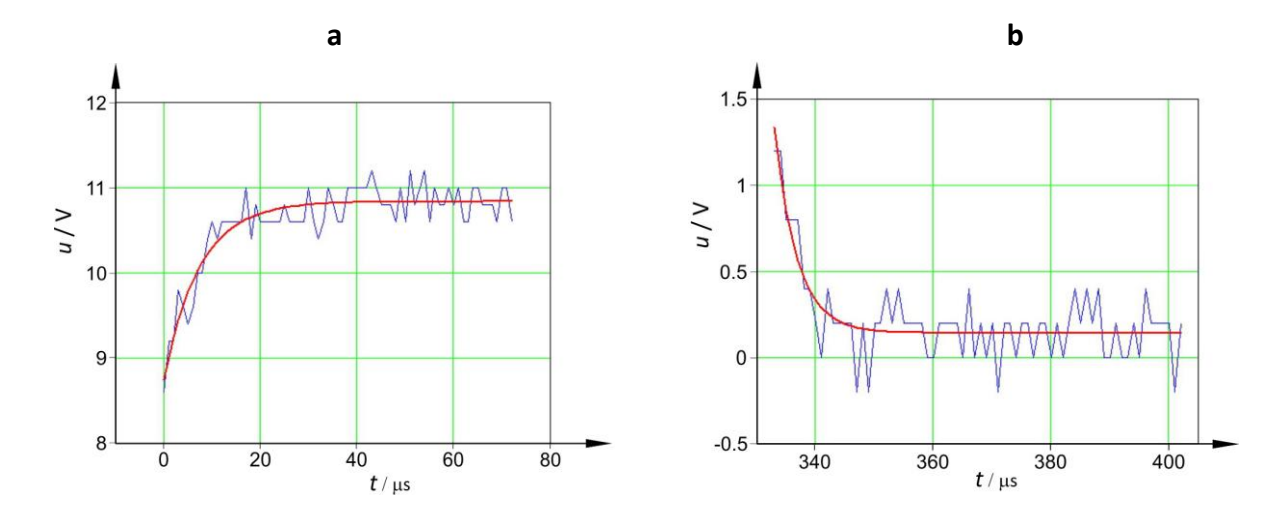


Figure 10. Voltage oscillogram (blue curve) approximated by response function (red curve) **(a)**-area of voltage increase on forward pulse front; **(b)** area of voltage decrease on rear pulse front.

Following the results of the response function approximation of forward pulse front, the following values were obtained: $R_E = 3.74$ Ohm, $R_F = 0.89$ Ohm, $C = 8.3 \cdot 10^{-6}$ F. Specific capacity, *i.e.* the capacity of electrochemical cell according to the equivalent interaction area of electrodes, is 0.5 F/m². Data of the voltage drop area approximation asserts that specific capacity reached 0.45 F/m².

With the prolongation of response function according to Eq. (11) with parameters obtained for several subsequent pulses and comparison with the oscillogram in Figure 9, it was established that electrochemical process proceeds normally, without significant changes in IES condition and without accumulation of residual polarization. That is, AFPSP for given conditions is selected correctly, providing necessary metal removal rate and avoiding a process of entering passivation zone.

According to Faraday's law we obtain an expression for determining material depth dissolution distribution on anode surface due to the action of one current pulse

$$h(x) = \frac{2K_{\nu}\kappa a\eta}{\ln p} \frac{1}{x^2 + a^2} \int_{0}^{\tau} u(t)dt$$
 (17)

where K_v is coefficient of electrochemical machinability of anode material; η is current efficiency coefficient; T is pulse period; u(t) is response function (10) obtained by approximating the corresponding voltage oscillogram section during current pulse passage.

If the process of electrochemical dissolution is stable as in the considered example, then according to Eq. (17) it is possible to calculate the thickness of the removed surface layer, taking into account the velocity of the wire electrode and current pulse frequency. In the case of ECM parameters deviation from normal reaction, oscillogram analysis will indicate unacceptable changes. Refusal to apply corresponding operational measures for correction of AFPSP will result in a significant reduction of current efficiency coefficient. This is approved by numerous experimental evidences in practical implementation of wire ECM technology.

Approximation of oscillogram signals in this work was carried out using a mathematical software package, which is quite convenient for research, but is not fundamentally necessary. Computational experiments have shown that sufficient accuracy in this case can provide an approximation of 3-5 points of the curve (filtered from digital noise). According to the least squares deviation method, this means that in order to find unknown coefficients, it is necessary to solve a system of 3-5 linear algebraic equations, which solution can be represented in an analytical form. That is, calculations are reduced to normal multiplication and addition operations that can be performed in real time on

microprocessor elements used in modern computer numerical control equipment for controlling and managing machine-tools and technological systems.

Conclusions

- 1. The concept of operational monitoring, forecasting and adaptive correction of AFPSP of ECM using mobile wire electrode is substantiated in order to improve accuracy and quality of surface shaping using the latest combined technology of sequential WEDM and ECM.
- 2. Based on experimental data, a mathematical model was developed that adequately describes the increase and decrease of polarization dynamics of anode in electrochemical machining using wire electrode, with a series of unipolar rectangular current pulses.
- 3. The solution of inverse mathematical problem is proposed which, based on the experimentally obtained plot of the response polarization-time dependence, allows–determination of R_E , R_F , C parameters of the substituted electrical equivalent circuit scheme of an electrochemical cell.

References

- [1] V. I. Osypenko, S. P. Poliakov, D. O. Stupak, R. I. Savisko UA 10153 MPK 7B23H1/02 (2005).
- [2] Y. Jiang, W. Zhao, X. Xi, L. Gu, X. Kang, *International Journal of Advanced Manufacturing Technology* **61(1-4)** (2012) 171-183.
- [3] R. Schuster, V. Kirchner, P. Allongue, G. Ertl, Science 289(5476) (2000) 98-101.
- [4] S. Skoczypiec, A. Ruszaj, *Precision Engineering* **38(3)** (2014) 680-690.
- [5] S. Skoczypiec, International Journal of Advanced Manufacturing Technology **87(1-4)** (2016) 177-187.
- [6] C. Zhao, L. Xu, Journal of Electrochemical Science and Engineering **8(4)** (2018) 321-330.
- [7] J. A. Kenney, G. S. Hwang, *Nanotechnology* **16(7)** (2005) S309.
- [8] S. Galanin, Elektrokhimicheskaya obrabotka metallov i splavov mikrosekundnymi impul'sami toka (Electrochemical Treatment of Metals and Alloys by Microsecond Current Pulses), Kostrom. Gos. Tekh. Univ., Kostroma, Russia, 2001, p.118 (in Russian).
- [9] S. Galanin, I. Kalinnikov, Surface Engineering and Applied Electrochemistry 44(5) (2008) 359-366.
- [10] M. Mithu, G. Fantoni, J. Ciampi, *International Journal of Advanced Manufacturing Technology* **55(9-12)** (2011) 921-933.
- [11] G. Wollenberg, H. Schulze, H. Trautmann, G. Kappmeyer, *Proceedings of the 15th ISEM*, (2007) 335-338.
- [12] O. Weber, A. Rebschlager, P. Steuer, D. Bahre, *Proceedings of the European COMSOL conference*, Rotterdam, 2013.
- [13] J. Sun, E. Taylor, R. Srinivasan, *Journal of Materials Processing Technology* **108(3)** (2001) 356-368.
- [14] M. A. Lavrent'ev, B. V. Shabat, *Methods of the theory of function of complex variable,* Nauka, Moscow, 1987, p.544 (in Russian).
- [15] V. S. Bagotsky, Fundamentals of Electrochemistry. John Wiley & Sons, Inc.: Hoboken, NJ, 2005, p.752.
- [16] J. Newman, K.E. Thomas-Alyea, *Electrochemical Systems*, John Wiley & Sons, NY, 2012, p.672.
- [17] F. Han, W. Chen, W. Ying, *Procedia CIRP* **68** (2018) 493-498.
- [18] V. P. Zhitnikov, A. N. Zaytsev, Impul'snaya elektrokhimicheskaya razmernaya obrabotka: monografiya (Pulse electrochemical machining: monograph), Mashynostroenye, Moscow, 2008, p. 413 (in Russian).
- [19] V. I. Osipenko, A. P. Plakhotny, A. Yu. Denisenko, *Pratsi Odeskoho politekhnichnoho universytetu* **1(43)** (2014) 55-60.

©2019 by the authors; licensee IAPC, Zagreb, Croatia. This article is an open-access article distributed under the terms and conditions of the Creative Commons Attribution license (http://creativecommons.org/licenses/by/4.0/)





Open Access: ISSN 1847-9286

www.jESE-online.org

Review

Platinum utilization in proton exchange membrane fuel cell and direct methanol fuel cell

Madhavi Bandapati¹, Sanket Goel² and Balaji Krishnamurthy^{1,⊠}

¹Department of Chemical Engineering, BITS-Pilani, Hyderabad Campus, Hyderabad-500078, India ²Department of Electrical and Electronics Engineering, BITS-Pilani, Hyderabad Campus, Hyderabad-500078, India

Corresponding author: <u>balaji@hyderabad.bits-pilani.ac.in</u>; <u>balaji.krishb1@gmail.com</u>;

Tel.: +91-040-663-03552

Received: February 15, 2018; Revised: March 22, 2019; Accepted: March 25, 2019

Abstract

Proton exchange membrane fuel cell (PEMFC) and direct methanol fuel cell (DMFC) are increasingly used as substitutes to conventional energy systems. Their compact design, high energy density and efficient energy-conversion offer several advantages over existing energy systems with potential for use in a variety of applications. However, performance, robustness and cost are the key challenges to overcome before fuel cells can be commercialized. Even though the use of platinum (Pt) and platinum group metal (PGM) alloy catalysts provide higher performance and durability, they are at the same time the largest cost components which need to be addressed. This paper reviews different approaches adopted to enhance Pt utilization such as reducing Pt loading, decreasing Pt particle size, developing Pt free metallic alloy catalyst, improving Pt dispersion, developing membrane electrode assembly (MEA) fabrication methods, increasing mass-transport at the electrode surface and modifying the catalyst support materials. Finally, the performance optimization efforts for Pt utilization are summarized with insights into probable directions of future research in this area.

Keywords

Electrochemical active surface area; hydrogen adsorption; CO stripping; catalyst particle size; catalyst loading; catalyst dispersion; catalyst support

Introduction

Over the last two decades, proton exchange membrane fuel cell (PEMFC) and direct methanol fuel cell (DMFC) have been extensively studied and are emerging as potential systems as they provide clean energy and are commercially viable [1]. They possess a series of highly advantages features such as low operating temperature (<100 °C), high efficiency, sustainability at high current

density, development of catalyst material for hydrogen generation, 10-100 fold reduction of the catalyst loading, multiple options for membrane electrode assembly (MEA) fabrication, manufacturing and synthesis process for gas diffusion layer (GDL) and membranes, development in thermal and water management, compactness, potential for low volume and weight, long stack life, fast start-up and suitability for discontinuous operation [2-4].

In the recent years, leveraging these advantages, automobile and fuel cell (FC) manufacturers are moving towards commercialization from a demonstration phase. This is carried out through development of suitable catalysts, introduction of zero emission vehicles and development of prototype vehicles that have adopted FC systems. However, several technological challenges and cost reduction still need to be overcome. The primary approaches towards addressing these challenges include reducing the precious metal catalyst loading with controlled particle deposition through improved electrode preparation methods, optimizing the MEA, enhancing the tolerance of MEA to high temperature to promote higher degrees of electro-catalysis, exploring non-platinum based electrode materials [5-7].

Platinum (Pt) or Pt-alloys such as PtRu, PtCo, PtNi, PtFe, PtV, PtMn, PtCr are the most suitable electrocatalysts for PEMFCs and DMFCs as they have low overpotential values, high catalytic activities and also ability to tolerate the harsh acidic surroundings inside FC. Pt is a less abundant and expensive noble metal that contributes as much as 50 % (even at 1.7 % of Pt) to the total cost of fuel cell. In addition, Pt utilization is quite low with only 25-35 % utilized for electroactivity [8-10].

The limited supply and high cost of Pt necessitate its optimal utilization and reduction in Pt loading. Table 1 illustrates the status and long term goals set by the U.S. Department of Energy for Pt utilization with Pt loading targets. As a result, optimizing Pt utilization in order to reduce cost has been the primary focus of much research in this field [11-13].

Characteristics	2011	Targets	
Cital acteristics	status	2017	2020
Platinum group metal (PGM) total content (both electrodes), g kW ⁻¹	0.19	0.125	0.125
PGM total loading, mg m ⁻²	0.15	0.125	0.125
Loss in initial catalytic activity, wt%	48	40	40
Electrocatalyst support stability, wt%	10	10	10
Mass activity, A mg _{Pt} ⁻¹	0.24	0.44	0.44
Non-Pt catalyst activity per volume of supported catalyst, A cm ⁻³	60	300	300

Table 1. Platinum metal content status and targets [13]

In order to improve Pt utilization efficiency, the electrocatalysts need to be developed with the reduced Pt loading and increased Pt active sites. The active research approaches explored towards enhancement of effective Pt utilization in PEMFC and DMFC electrodes are grouped in following categories [14,15]:

- Reducing the electrocatalysts loading in fuel cell electrodes.
- Developing novel nano-structured thin-film Pt by decreasing the electrocatalysts nanoparticle size
- Reducing Pt dependence by developing metallic alloys and Pt-free electrocatalysts.
- Improving electrocatalysts dispersion by using novel fabrication methods.
- Developing MEA fabrication methods to enable better catalyst dispersion and utilization.
- Using new techniques to increase mass-transport at the fuel cell electrode surface.
- Improving the performance of carbonaceous electrocatalysts support and exploring novel noncarbonaceous electrocatalysts support materials.

Although Pt is the catalyst commonly used for both anode and cathode in PEMFCs, the oxygen reduction reaction (ORR) at cathode is more complex with sluggish reaction kinetics, thus requiring higher Pt loading, typically several times higher than that of anode. In addition, the hydrogen oxidation reaction (HOR) on the DMFC anode catalyst suffers from high over potential. This has triggered researchers to explore optimization of Pt catalyst including the synthesis of catalysts that are more active and less expensive than Pt [16,17].

This paper focuses on various approaches, already taken by researchers to optimize Pt utilization for cathode of PEMFC and both electrodes of DMFC to reduce the cost and improve the performance and durability of PEMFCs and DMFCs. Catalyst utilization can also be represented in terms of mass activity and specific activity. As catalyst utilization is a surface phenomenon [18], the progress made in this area has been presented by considering electrochemical active surface area (ECSA), as the benchmark parameter across various research approaches over a period of time. The calculation procedure of this parameter is briefly described in the following section.

In addition, fuel cell performance can also be increased by increasing specific activity of the catalyst by alloying or shaping. Specific activity (SA) is the ratio of the kinetic current to the real surface area of the catalyst. Nevertheless, in the case of nanostructures the real surface area is significantly greater than geometric and can be determined using CO stripping [21]. However, discussing specific activity of the catalyst is beyond the scope of this review.

Measuring platinum utilization efficiency

Platinum utilization (PtUt) is the amount of exposed Pt atoms available for catalytic reaction among those dispersed on the electrode. As catalyst utilization is a surface phenomenon, the surface and the specific surface area are considered as critical factors for measurement. Here, electrochemical active surface area (ECSA) is considered as a measure of Pt utilization. A comparison of ECSA with geometrical specific surface area (GSA) tells the number of electrochemically active Pt surface atoms. Therefore, the ratio of ECSA to GSA is considered as a measure of PtUt [19,20].

$$PtUt, \% = [ECSA/GSA] \times 100$$
 (1)

Electrochemical active surface area (ECSA)

ECSA is a measure of the number of electroactive Pt sites on the surface of the catalyst on which reaction occurs and is sometimes called the intrinsic Pt catalyst surface area. Numerous methods are available in the literature to calculate ECSA of Pt catalysts. In the context of this review, two primary methods, H-adsorption (ECSA_H) and CO stripping (ECSA_{CO}) used for measuring ECSA are explained below [21].

H-adsorption (ECSA_H)

ECSA_H of Pt catalyst, reported in m²g_{Pt}⁻¹ units, is determined conventionally from hydrogen under-potential deposition (HUPD) reaction, which can be expressed as [22]:

$$Pt + H^+ + e^- \rightleftharpoons Pt - H_{ads}$$
 (2)

Figure 1 shows a typical hydrogen electrosorption/desorption voltammetric profile for the polycrystalline Pt electrode in 0.5 M H_2SO_4 . Characteristic peaks between 0.0 and \sim 0.2 V are attributed to the atomic hydrogen desorption/adsorption at Pt surface and ECSA_H can be determined by:

$$ECSA_{H} = (100 Q_{H}) / (Q_{H(ref)} m)$$
 (3)

In Eq. (3), $Q_{\rm H}$ / $\mu{\rm C}$ is the charge calculated by integrating the area under the cyclic voltammetry (CV) curve (Figure 1) within the potential range of hydrogen desorption, $Q_{\rm H(ref)}$ is the charge corresponding to formation of the monolayer of adsorbed hydrogen on the polycrystalline Pt given as 210 $\mu{\rm C}$ cm⁻², and m is the mass of Pt loading (mg) that indicates the amount of Pt at the working electrode [23,24].

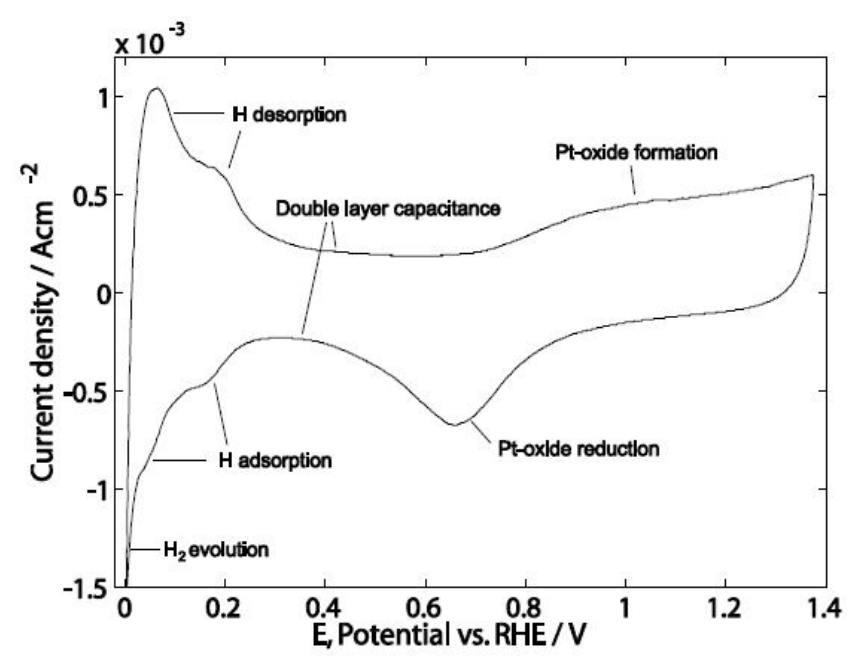


Figure 1. Typical hydrogen adsorption/desorption voltammetry profile for polycrystalline Pt electrode in 0.5 M H_2SO_4 at room temperature at 100 mVs⁻¹ [21]

When electrodes are fabricated with the polymer electrolyte membrane (PEM), however, all Pt active sites are not available for electrochemical reaction. This may be due to an improper contact of Pt particles with the solid polymer electrolyte or to electrical insulation between Pt particles caused by a thin film of the electrically non-conducting polymer electrolyte. In such case, the ECSA measured by CV in solid polymer electrolyte is denoted as ECSA_{MEA} which is called as driven – cell mode [25]. This value may be smaller than ECSA. The ratio of ECSA and ECSA_{MEA} is termed as MEA platinum utilization [81].

CO stripping

The most commonly used anode catalyst for DMFC is platinum-ruthenium (PtRu). The ECSA and performance of the prepared PtRu anode catalysts for DMFC are measured by means of CO stripping method.

Pre-adsorbed carbon monoxide (CO_{ad}) oxidation can be calculated using CO adsorption removal voltammogram (Figure 2) at a particular scan rate. Gaseous CO can be purged into the cell to permit complete CO adsorption onto the electrocatalyst while maintaining a steady voltage. The surplus CO can be removed by nitrogen gas [26].

The following reactions occur on the platinum surface for methanol oxidation:

$$CH3OH + Pt \rightarrow COad-Pt + 4H+ + 4e-$$
 (4a)

$$Pt + CO_{ad} - Pt + H_2O \rightarrow CO_{ad} - Pt + H^+ + OH_{ad} - Pt + e^- \rightarrow 2Pt + 2H^+ + CO_2 + 2e^-$$
 (4b)

For PtRu, the equation for methanol oxidation is as follows:

$$CH3OH + PtRu \rightarrow COad-PtRu + 4e- + 4H+$$
 (5a)

$$CO_{ad}-PtRu + H_2O \rightarrow CO_{ad}-PtRu-OH_{ad} + e^- + H^+ \rightarrow PtRu + CO_2 + 2e^- + 2H^+$$
(5b)

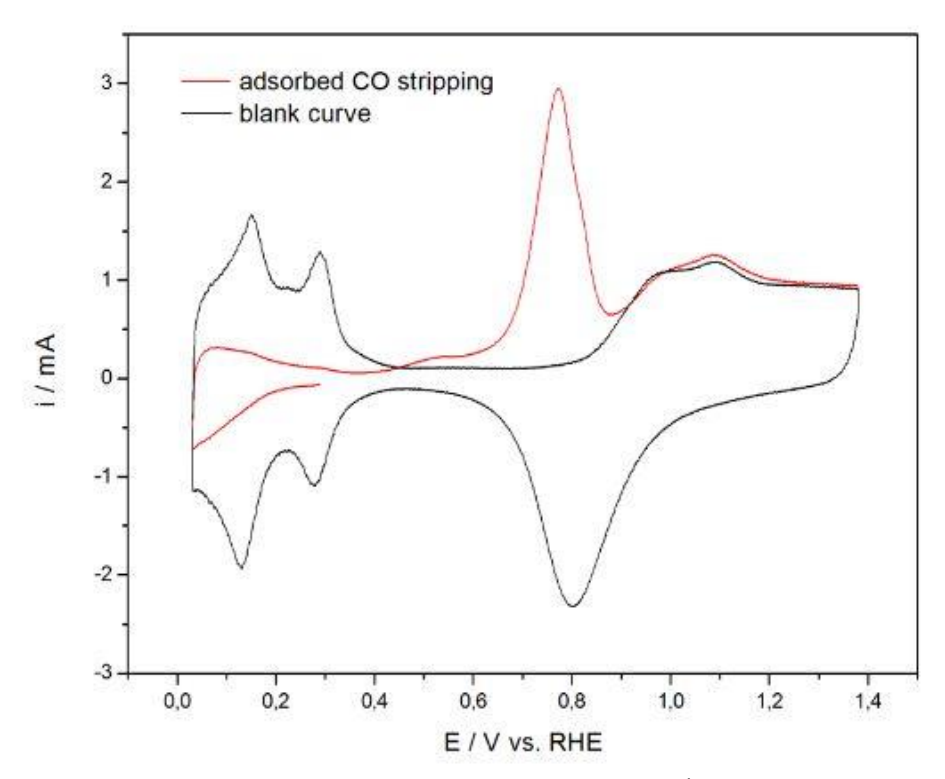


Figure 2. CO stripping current (red line) recorded at 500 mVs⁻¹ scan rate for polycrystalline Pt electrode in 0.5 M H_2SO_4 at 298 K together with a blank curve (black line). CO adsorption at 0.29 V vs. RHE for 20 min [21]

As the charge of the CO oxidation peak is taken as two electrons per CO molecule, the resulting charge is approximately double of that corresponding to the hydrogen-desorption peak. ECSA_{CO} can be calculated using the following equation:

$$ECSA_{CO} = (100 Q_{CO}) / (Q_{CO(ref)} m)$$

$$(6)$$

In Eq. (6), Q_{CO} / μ C is the charge calculated by integrating the area under CO desorption peak, $Q_{CO(ref)}$ is the charge needed for oxidation of the monolayer of adsorbed CO on the platinum surface, given as 420 μ Ccm⁻², and m is the mass of Pt loading (mg) indicating the amount of platinum on the working electrode. CO stripping gives realistic ECSA on Pt-alloys, whereas ESCA based on HUPD is usually lower [27].

Optimization approaches for PEMFC Cathode

Some approaches to optimizing Pt utilization in PEMFC cathode are described below:

Reducing Pt loading and decreasing Pt particle size

Typically, the performance of a catalyst layer (CL) has proportional relationship with the catalyst loading. However, in the case of platinum, there is a challenge of enhancing CL performance while decreasing Pt loading. In order to achieve this, reducing of particle size and improving Pt dispersion on the catalyst support have been explored. As was already reported, the effective particle size of Pt based catalyst is between 2 nm and 4 nm [28]. Since the percentage of exposed Pt decreases with increase of Pt particle size, only 20-50 % of total Pt is available for catalytic reaction, what is far below ideal dispersion.

Martin *et al.* [29] attempted to optimize electrode performance at significantly low Pt loading (0.012 mg cm⁻²) obtained by electrospray method. By optimizing control parameters (Nafion® content, flow rate for electro-spraying catalyst ink and pressure for hot pressing MEA) they could achieve high

PtUt of 20 kW g^{-1} at 3.4 bar, a 70 °C. This is relatively high PtUt when compared to the previous of 3.3 kW g^{-1} [30]. Later on, the same team reported [31] further increase of PtUt to 30-35 kW g^{-1} at low Pt loading of 0.01 mg cm⁻², achieved by utilizing additional benefits of a microporous layer of carbon nanotubes coated on GDL as the cathode catalyst support. The authors also observed that Pt utilization remained unchanged for Nafion® content in the range of 30-50 %.

Wang *et al.* [32] fabricated MEA with low Pt loading of 0.022 mg cm⁻² at the cathode side by simultaneously using electrospray and electrospinning (E/E) dispersion techniques, where they introduced Nafion® and Pt using two separate needles to produce Nafion® nanofibers and platinum nanoparticles (PtNP). Using this technique, they could regulate the size of fibers and loading of Pt catalyst, what resulted in improved ECSA with excellent Pt utilization of 42 kW g⁻¹ for H₂/O₂ electrode at 0.022 mg cm⁻² Pt cathode loading.

Alia *et al.* [33] developed a novel electrocatalyst using Pt/Pt alloy nanotubes (PtNT) and carried out voltammetry measurements for every 6000 cycles to investigate durability and ORR activity. They found that the electrode with cathode loading of 0.04 mg cm⁻² showed highest ECSA of 23.9 m² g⁻¹ with 127 % PtUt (Eq. 1) for which electrode porosity was stated as the reason.

Su *et al.* [34] combined ultrasonic spray coating technique and catalyst coated substrate (CCS) to achieve low Pt loaded gas diffusion electrodes (GDE). Four electrode samples with varying Pt loading (between 0.138 and 1.208 mg cm⁻²) were studied at 160 °C (air and H₂ flow rate 250 and 100 cm³ min⁻¹), while maintaining atmospheric conditions. As shown in Figure 3, they observed that current density values increased with decrease in Pt loading of cathode electrode and found that the electrode having 0.712 mg cm⁻² Pt loading showed the highest current density values due to the highest ECSA. Therefore, low Pt loading electrode means thin CL, when most of the catalyst is concentrated in the interface between CL and electrolyte membrane, resulting in higher Pt utilization.

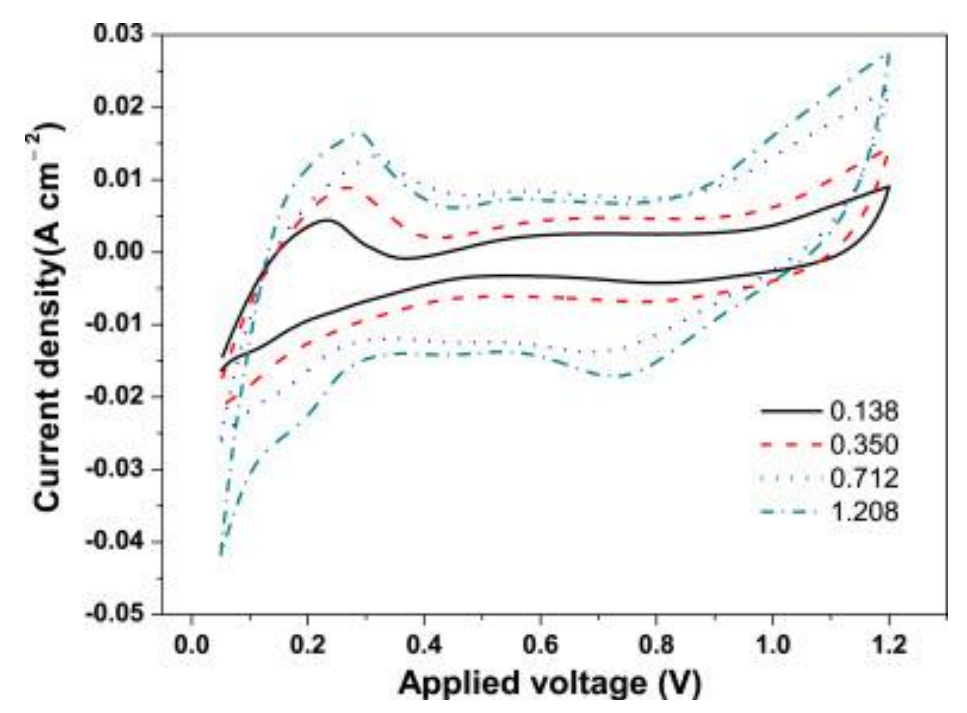


Figure 3. CV profiles of GDEs with different catalyst loadings. Reproduced from [34] with permission from Elsevier

Nabil et al. [35] electrochemically characterized the novel niobium carbide/carbon nano tubular porous structure (NbC) as the catalyst support for PEMFC electrodes. Supports were prepared by electrospinning and functionalized with Pt nano particles. The ORR activity and catalyst stability

showed less ECSA for Pt/NbC/C (43 $\text{m}^2\,\text{g}^{-1}$) than for geometrically calculated surface area (90 $\text{m}^2\,\text{g}^{-1}$). The less conductive Nb₂O₅ was stated as a reason for lower PtUt. Also, 31 % retention in ECSA was observed for Pt/NbC/C after 10,000 cycles when compared with commercial Pt/C (only 5 % retention). The greater stability is attributed to the corrosion resistance of one dimensional NbC nanostructures.

The same group [36] using the same technique synthesized nanotubes with suitable properties as the catalyst support for PEMFC cathode. 3 mm Pt particles were deposited on NbC nanotubes. From electrochemical characterization, they observed less ECSA (43 $\rm m^2\,g^{-1}$) for 30 % Pt/NbC than for 50 % Pt/C. Also, better stability was found for the novel support than commercial 50 % Pt/C, when ECSA of both catalysts were equal. Summarized results for the above category are given in Table 2.

Method / Technique / Support	Pt loading, mg cm ⁻²	ECSA, m ² g ⁻¹	PtUt, %	Reference
Electrospray	0.012			[29]
Carbon microporous layer (CMPL)	0.01			[31]
Electrospinning/Electrospray (E/E)	0.022	93.9		[32]
Porous PtNT	40	23.9	127	[33]
Ultra sonic spray coating technique	0.713	28.38		[34]
Electrospinning (Pt/Nb/C)	0.2	43	-	[35]
Electrospinning (Pt/Nb/C)	30 % Pt	43	-	[36]

Table 2. Reducing Pt loading and decreasing particle size (PEMFC cathode)

Improving Pt dispersion

Dispersion of Pt on different carbon supports has been explored using various methods such as impregnation-reduction, ion exchange (IE), micro emulsion-based synthesis, *etc*. The supports used may include Vulcan, multiwalled carbon nanotubes (MWCNT), Vulcan XC-72R, carbon aerogel (CA), BP2000, activated carbon, carbon cryogel and others. The objective of dispersion is to reduce average Pt particle size and hence, to increase the catalytic surface area [37].

Bayrakceken et al. [38] deposited Pt nanoparticles of size 1-2 nm uniformly distributed on carbon supports (Pt/VXR, Pt/MWCNT, Pt/BP2000) using super critical carbon dioxide deposition technique (Figure 4).

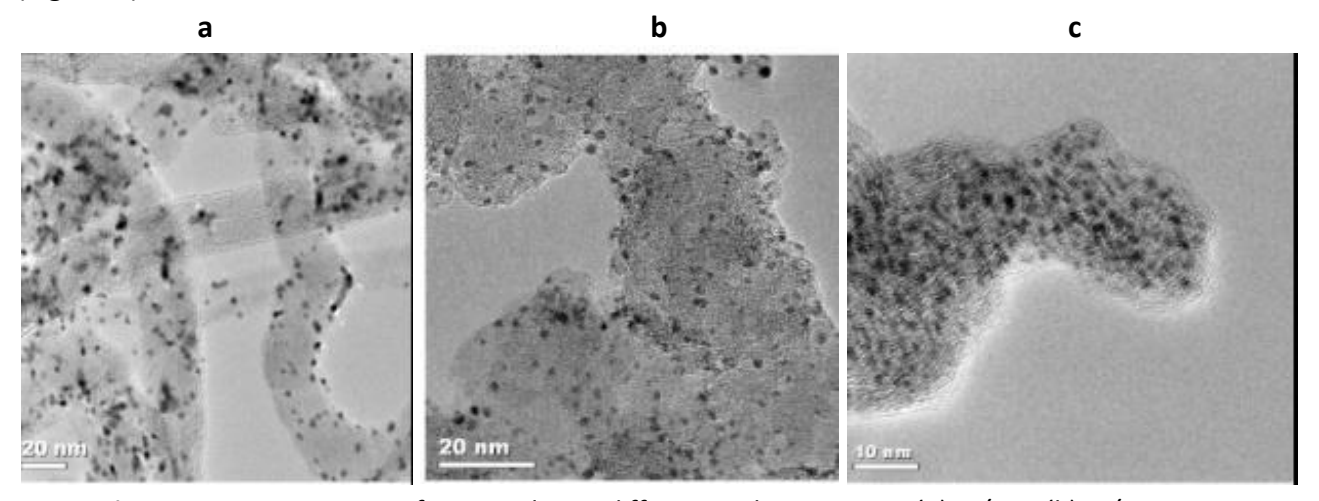


Figure 4. HRTEM images of Pt particles on different carbon supports (a) Pt/VXR (b) Pt/MWCNT and (c) Pt/BP2000. Reproduced from [38] with permission from Elsevier

They achieved nearly three times higher ECSA (173 m² g⁻¹ for Pt/VXR) with the reduced Pt loading when compared to a commercial catalyst (57 m² g⁻¹). The authors assumed that even for smaller Pt particles, the hydrophobic nature of carbon support makes Pt particles inaccessible for electrolytes.

Here, the highest PtUt of 93 % was observed for Pt/MWCNT with ECSA of 130 m² g⁻¹. The observed differences were due to variation in structure of carbon supports.

Fang *et al.* [39] deposited PtNTs on Vulcan XC-72 (VC) carbon black (CB) by employing the homogeneous deposition technique with ethylene glycol (EG) (reducing agent) using polyol process (HD-EG). They found higher ECSA of 78 m² g⁻¹ with high Pt utilization of 78 % when compared with the microwave (EG-MW) assisted polyol approach or conventional sodium borohydride (NaBH₄) reduction process. This highest Pt utilization (60 wt% on VC by HD-EG) was attributed to the relatively small PtNP with improved particle dispersion creating more active sites for the anticipated reactions.

Mroz et al. [40] used the pulse laser deposition (PLD) method for depositing catalyst films directly on Nafion® membranes and GDL and achieved accurately controlled low catalyst loadings with greater uniformity. Under various pressure ranges, electrodes were prepared and studied by varying thickness of the catalyst film between 0.09 and 3.47 nm, in proportion to the laser pulses between 75 and 3000. At low cell voltage, the results revealed higher current densities and less transport resistance of reagents when compared to cells with Pt catalyst placed on the Nafion® membrane. In the case of high cell voltages, low currents were generated due to less active surface area of Pt available for reactions. The authors stated that the efficiency can be further increased by growing the contact area between electrolyte and catalyst and also by enhancing the reaction zone to advance the passage of reagents.

Rost *et al.* [41] deposited Pt particles on carbon nanofibers (CNF) by employing the pulse plating technique (PPT). They observed 3.1 times higher ECSA of 148.6 cm² mg⁻¹ with CNF functionalization at 120 W for 10 min. The creation of the functional groups on fibrous surface of the nanoparticles and graphene (Gr) is stated as the reason for smaller and homogenous dispersion of catalyst.

Huang *et al.* [42] used the impregnation method to synthesize highly dispersed Pt catalyst with addition of centyltrimethylammonium bromide (CTAB) as dispersant at 300 °C. They prepared CL samples with different Pt loadings and observed higher ECSA and high PtUt for the catalyst sample with 4.12mg cm⁻² dispersant concentration. The improved results were attributed to lypophilic alkyl and hydrophilic amine groups of CTAB.

Lv et al. [43] synthesized the novel carbon mixed carbide-based catalyst support (SiC/C) to improve electrochemical performance and catalytic activity of PEMFC cathode. They deposited Pt catalyst on nano SiC/C particles and observed homogenous dispersion of Pt particles on nano-SiC particles with evidently increased ECSA ($48 \text{ m}^2\text{ g}^{-1}$) for Pt/SiC/C when compared to Pt/SiC ($13 \text{ m}^2\text{ g}^{-1}$). The addition of carbon to Pt/SiC and uniform dispersion of Pt nano particles on the novel support were attributed to the increased PtUt in ORR activity of PEMFC electrode. Summarized results for the above category are given in Table 3.

Dispersion echnique dispersant Pt loading ECSA, m² g⁻¹ PtUt, % Catalyst support Ref. Pt/VXR 9.0 wt% 173 74 Pt/CNT 93 [38] ScCO₂ 9.9 wt% 130 Pt/BP2000 47.5 wt% 102 36 HG-ED 0.2 mg cm⁻² 78 78 [39] CB [40] PLD 1.24 μg cm⁻² CB -**PPT** Pt/CNF 1 mg cm⁻² 148.6 [41] **CTAB** CTAB: 0.096 mg cm⁻² 65.97 63.53 [42] EG reduction method Pt/SiC/C 20 % 48 [43]

Table 3. Improving Pt dispersion (PEMFC cathode)

Structural modification of catalyst layer

Catalyst layer needs to be designed in order to ensure effective movement of electrons, protons, reactant gas, and water through a porous medium. Structural modification of CL aims to improve mass transport, decrease interfacial resistance between catalyst layer and gas diffusion layer, enhance catalyst utilization, and reduce Pt loading [44].

Su *et al.* [45] replaced the conventional double catalyst layer (DCL) with a novel double carbon layer (NDCL) cathode with high Pt content for inner layer and low Pt content for outer layer. Five cathodes (NDCL-1 to NDCL-5) with different Pt distribution ratio of inner and outer layers were prepared (Table 4).

From CV (Figure 5), better ECSA for the novel DCL than single catalyst layered (SCL) and conventional DCL catalysts can be observed. The highest ECSA of 81.4 m² g⁻¹ was recorded for NDCL-2 having the same inner and outer layer thicknesses, which was attributed to the reduced mass transport resistance. Further, the reduced catalyst and Nafion® content in outer layer was proved beneficial for ORR and water removal.

Novel double catalyst layer cathode NDCL-1 NDCL-2 NDCL-3 NDCL-4 NDCL-5 Pt distribution (inner: outer) 8:2 7:3 5:5 9:1 6:4 0.44 1.71 2.78 L_{out}/L_{in} (estimated value)^a 3.91 1

Table 4. Five DCL cathodes with different inner and outer Pt distribution ratios [45]

^aL_{out}: outer catalyst layer thickness, L_{in}: inner catalyst layer thickness.

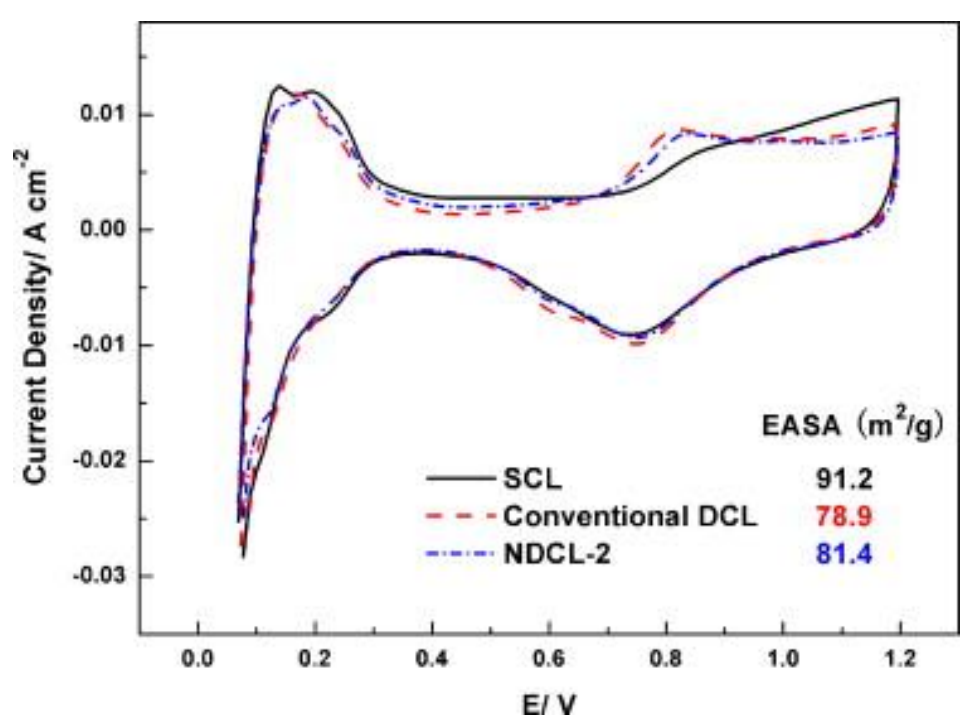


Figure 5. CVs for MEA with single, conventional double and novel double catalyst layered cathode structures. Reproduced from [45] with permission from Elsevier (ESCA is marked as EASA on the graph

Qiu *et al.* [46] developed a novel cathode structure (NCS) having double catalyst layer with reduced Pt loadings of 0.23 mg cm⁻² and 0.11 mg cm⁻² for inner and outer CL, respectively (Figure 6). The NCS was provided with hydrophobic and hydrophilic regions. It was observed that rich small pores of the outer layer provided efficient electrochemical active surface with the reduced GDL interfacial resistance, improving thus mass transfer. The compact structure of the inner layer

provided more active catalyst sites, resulting in improved migration of protons towards the membrane. The results showed 50 % Pt utilization for the developed NCS which was 28 % higher than that of traditional catalyst structure (TCS).

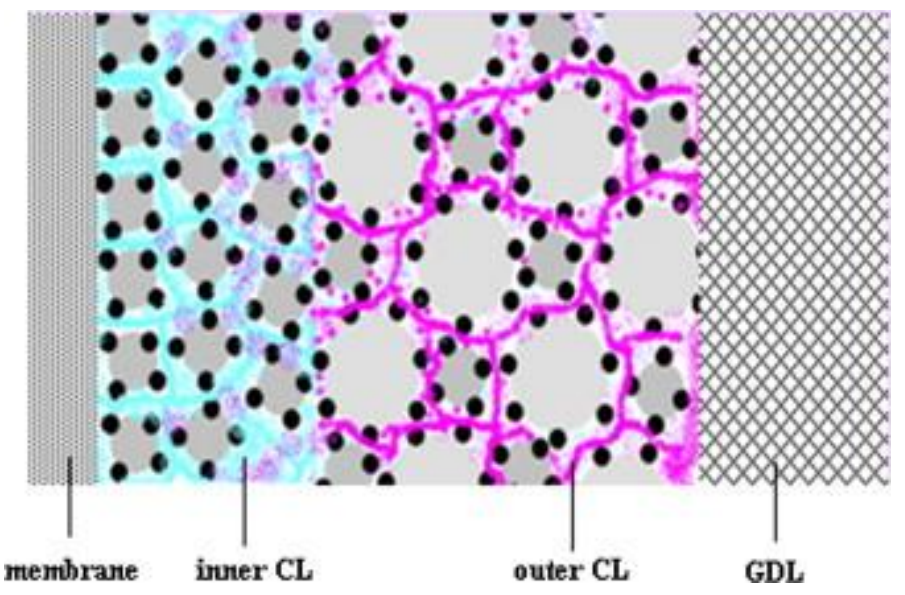


Figure 6. Schematic of novel cathode structure (NCS). Reproduced from [46] with permission from Elsevier

Avcioglu *et al.* [47] made an attempt to explain the significance of CL in water management since CL impacts water balance, while water flooding leads to mass transfer limitation at high current densities. To enhance durability performance and to ensure efficient thermal and water management in the components of PEMFC, the authors constructed a mesoporous hydrophobic channeled catalyst layer by addition of poly(tetraflouroethylene) (PTFE) nanoparticles and employing a two-step catalyst preparation method. By electrochemical characterization of three different types of catalyst *viz.*, Pt/C, Pt/C-Nafion®, Pt/C-Nafion®/PTFE, it was found that addition of PTFE to the catalyst diminished Pt agglomeration, but reduced ECSA and PtUt of Pt/C-Nafion®/PTFE. It was concluded that higher ECSA (77 m² g⁻¹) was observed for Pt/C catalyst because of increased total catalyst surface area. The ECSA (70 m² g⁻¹) of Pt catalyst with Nafion® (Pt/Nafion®) was slightly reduced, but PtUt was improved due to formation of Pt agglomerates by Nafion® addition. The ECSA of Pt/Nafion®/PTFE, however, was only 45 m² g⁻¹ and PtUt was 56 % with enhanced diffusion process in the catalyst layer. Disruption of TPB, active sites blockage and increased average pore diameter were stated as the consequences of PTFE addition.

In order to overcome kinetic loss occurring at low Pt loading, Breitwieser *et al.* [48] employed a direct membrane deposition technique (DMD) in MEA fabrication process, wherein the conventionally free-standing membrane was replaced by two 8–15 µm thin ionomer layers with low Pt loading of 0.102mg cm⁻² on anode and 0.029 mg cm⁻² on cathode, respectively. At 300 kPa_{abs} of total pressure and under oxygen atmosphere, the DMD fuel cell yielded a maximum power density of 2.56 W cm⁻² with very high PtUt of about 88 kW g⁻¹. This value was 2.3 fold higher than that of a commercial Nafion N-211 membrane reference fuel cell. The high PtUt efficiency was attributed to the novel DMD fabrication technique, which favored lower ionic resistance and improved power density in the high current density range.

To reduce Pt loading, Kaplan et al. [49] developed Pt alloys and core-shell structures. They synthesized two carbon supported Pt-surface enriched nano sized (Pt-SENS) catalysts and performed characteristic studies with a partial Pt shell and low-cost ruthenium (Ru) and iridium (Ir)

metal cores. Instead Pt loading of 48 mg cm $^{-2}$ for commercial Pt catalyst, they used Pt loading of 14 mg cm $^{-2}$ for Pt/Ir/XC72 and 19.5 mg cm $^{-2}$ for Pt/Ru/XC72 prepared electrodes. ECSA of 29 m 2 g $^{-1}$ was obtained for Pt/Ru/XC72 catalyst using CO-stripping method, while 26 m 2 g $^{-1}$ for Pt/Ir/XC72 and 48 m 2 g $^{-1}$ for 50 % wt Pt/C were obtained by HUPD method. It was concluded that Pt-surface-enriched structure increased availability of Pt particles for the catalytic reactions.

Chen et al. [50] designed a new gradient cathode with appropriate Pt/C ratio gradient direction (70 wt% inner side and 40 wt% outer sides) and Nafion® gradient span (33 wt% inner side and 23 wt% outer sides). This improved both Pt utilization and mass transfer, thus significantly improving the performance. Especially under low humidity, the performance of appropriate gradient MEA was 135.7 % higher than the MEA with SCL cathode at 20 % relative humidity. It also provided better water management, improved proton conductivity in cathode, and showed lower ohmic resistance and charge transfer resistance. Summarized results for the above category are given in Table 5.

Novel Cathode Structure	Pt Loading	ECSA, m ² g ⁻¹	PtUt, %	References
NDCL	0.2mg cm ⁻²	81.4		[45]
NCS	0.4mg cm ⁻²	35.42	50.56	[46]
Pt/C	21 wt%	77	75	
Pt/C-Nafion®	13 wt%	70	99	[47]
Pt/C-PTFE	8 wt%	45	56	
DMD	29 μg cm ⁻²		88 kW g _{Pt} -1	[48]
Pt/Ru/XC72	19.5 μg cm ⁻²	29		[40]
Pt/Ir/XC72	14 μg cm ⁻²	26		[49]
Pt/C &Nafion® ratio	200 μg cm ⁻²	8.4		[50]

Table 5. Structural modification of catalyst layer (PEMFC Cathode).

Optimization of catalyst parameters

High Pt utilization can be achieved by optimizing various catalyst layer parameters such as Nafion® content, Pt loading, Teflon content, catalyst layer and carbon support thicknesses, etc. [51].

Cheng et al. [52] investigated the effect of Nafion® and PTFE on PtUt for two catalyst layers: a) E-TEK electrode/GDE prepared using immersion method where Pt is impregnated with Nafion® and b) thin film catalyst layer (TFCL) prepared by blending Nafion® and Pt catalyst. PtUt of 77.8 % and 45.4 % were observed for the first and the second catalyst layer, respectively. It was concluded that while the catalyst particles are provided with sufficient passage ways for the transfer of protons in the first case, the thin film catalyst layer experienced lack of conduction because of the blockage of passage ways by the Nafion® solid.

Antolini *et al.* [53] investigated the effect of Nafion® loading on ORR at PEMFC electrode. They observed that the electrode exhibited poor electrolytic conductivity at low Nafion® loading and that ECSA increased with increasing content of Nafion® (Figure 7). The introduction of Nafion® is stated to improve the active surface area, resulting in better transport of protons through the electrolyte.

Sasikumar *et al.* [54] investigated the dependence of Nafion® content on Pt loading. Electrodes were prepared with different Pt loadings (0.5, 0.25, 0.1 mg cm⁻²) and different Nafion® ionomer contents (20, 30, 40, 50, 60 wt%). The highest PtUt (52 %) was obtained at 40 wt% Nafion® content for Pt content of 0.25mg cm⁻². The authors concluded that Nafion® content must be determined by Pt loading and the fabrication technique used. The electrode performance was found to improve with enhancement of Nafion® content up to 40 %, but further increase in Nafion® content reduced the performance. The reasons attributed to this effect are blockage of Pt sites, decreased gas

permeability and augmented mass transport polarization. The increased distance for gas permeation, diffusion and migration are stated as reasons for transport limitation.

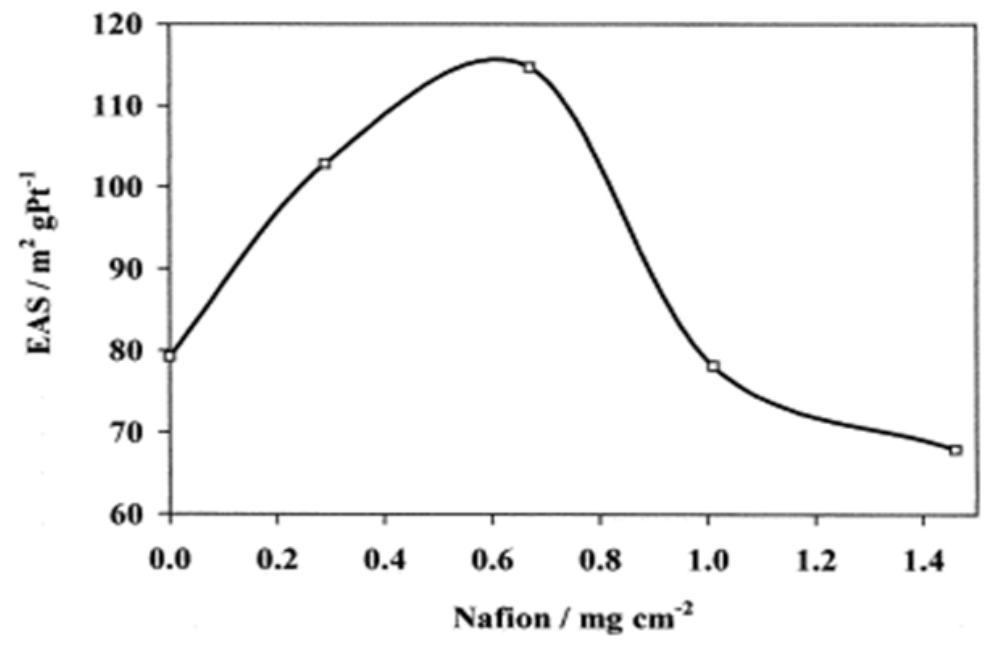


Figure 7. ECSA (marked as ESA on the graph) variation with Nafion® loading in the CL (20 wt% PTFE/C on DL, 0.2mg cm⁻² of Pt in CL). Reproduced from [53] with permission from Elsevier

Jiang *et al.* [55] studied the effect of thickness of carbon supported Pt catalyst layer in ORR using a thin film rotating disc electrode. Various catalyst layer thicknesses (0.25, 0.5, 1.0, 2.0, 4.0, 8.0 mm) were examined. The highest PtUt (77.9 %) was observed for 8.0 mm film. It was concluded that ECSA tends to increase with increasing thickness of the catalyst layer, showing more activity towards ORR accordingly.

Bayrakceken *et al.* [56] used super critical CO_2 deposition to prepare Vulcan supported Pt catalyst (Pt/Vulcan) and studied the effect of thermal reduction. Samples with Pt loading of 9 %, 15 %, 35 % were produced and ECSA were investigated using CV. The order of ECSA was found as follows: Pt/Vulcan 35 % < Pt/Vulcan 15 % < Pt/Vulcan 9 %. Although ECSA for Pt/Vulcan 15 % was found higher than for Pt/Vulcan 35 %, the PtUt was lower. This difference is, however, quite small (58 % vs. 62 %) and is not considered significant related to the uncertainty in both the calculated and the measured average Pt particle sizes. The difference in ECSA between Pt/Vulcan 15 % and 35 % catalysts is attributed to the differences in the Pt particle sizes, since ECSA Pt values differ by a factor of approximately 1.5.

Using plasma dc-magnetron sputtering technique, Khan *et al.* [57] studied the conical nanopillar structured Pt catalyst sputtered on the cathode with argon pressures of 0.05, 0.1, 0.5 mbar and at Pt loading range of 0.05 - 0.2 mg cm⁻². They observed high ECSA for the catalyst nanopillar deposited at 0.5 mbar at low Pt loading of 0.05 mg cm⁻². It was concluded that the deposition of uniform conical nanopillars on the electrode at high pressure improved catalytic activity and led to higher PtUt.

Slavcheva *et al.* [58] studied the effect of sputtering parameters (film thickness, argon pressure, dc-sputtering power) on thin films deposited by dc-sputtering technique. At low sputtering power (120–130 nm thick Pt films, 6 mTorr argon pressure, 100 W dc power), they found a stable and crystalline catalyst film with thickness between 120-130 nm, with large ECSA and PtUt. It was concluded that ECSA increased with increase of film thickness and improved the electrochemical activity towards ORR.

Wang *et al.* [59] studied the influence of PTFE on electro spun/electro sprayed (E/E) MEA. They introduced only 1 wt% PTFE to the process which resulted in PtUt of 0.076 g kW⁻¹ at only 0.094 mg cm⁻² Pt loading. The improvement was attributed to enhanced hydrophobicity of the nanofibers which increases mass transfer and overall performance.

Speder *et al.* [60] studied the effect of Pt/carbon ratio on degradation of PEMFC catalyst. They used a colloidal synthesis approach for Pt/Vulcan and Pt/KetjenBlack catalysts using accelerated stress test (AST) in half cells. It was concluded that the loss in ECSA due to AST treatment depends on carbon support and Pt loading.

Zhao *et al.* [61] investigated the impact of pore size of FDU-15 (two-dimensional hexagonal ordered mesoporous carbon (OMC)) supported Pt catalyst by adopting a soft-template method. Samples with four different pore sizes ranging from 4.0 nm to 8.1 nm were prepared by the addition of pore expanding agents. By impregnation method, Pt catalysts were prepared using FDU-15 samples as catalyst supports and reducing agent, EG. CV and linear sweep voltammetry (LSV) measurements illustrated that catalyst with a pore size of 6.5 nm showed the highest ECSA (70.2 $\rm m^2$ $\rm g^{-1}$). It was also observed that Pt particle size is reduced with increase in pore size up to 6.5 nm and remained unchanged with further increase in pore size.

Kim *et al.* [62] examined the effect of diffusing solvents with varying main chain mobility of Nafion® to demonstrate large influence on Nafion® agglomerates, morphology and other properties such as proton conductivity and water uptake. The MEA synthesized from the dimethyl sulfoxide based isopropyl alcohol (IPA) and N-methyl-2-pyrrolidone (NMP)-based catalyst inks presented ECSA of 40.9, 43.0 and 52.5 m² g⁻¹, respectively. The introduction of diffusing solvents resulted in better diffusion of Nafion® into Pt/C aggregates, bringing more Pt particles in contact with Nafion® thereby increasing the catalytic activity at reduced current density.

Ruengkit *et al.* [63] investigated the influence of GDL properties (type of material (carbon paper (CP), carbon cloth (CC)), thickness, PTFE content and presence of micro porous layer (MPL)) on ECSA of Pt electrodeposited layer and fuel cell performance. Pt catalyst was electrodeposited by dc current onto GDL, with CC and CP of different thicknesses and hydrophobicity, and with and without presence of MPL. Despite their morphological differences, relatively similar ECSA (~120 m² g⁻¹ Pt) were obtained, while better performance for CC at higher current densities is due to its lower resistance and higher porosity. Pt deposited on a very thin GDL (90 μ m) or GDL having high PTFE content (\geq 30 %) or containing MPL, consist of non-uniform particles distributed unevenly on the GDL surfaces, resulting in low ECSA (\leq 120 m² g⁻¹ Pt) and FC performances ($i\leq$ 210 mA cm⁻²). Pt electrodeposition on the CC having low PTFE content (10 %) produced small and uniform Pt particles distributed evenly throughout the GDL surfaces resulting in highest ECSA (193 m² g⁻¹ Pt). The same phenomenon was also observed for the two-layered GDL, which is attributed to the absence of the hydrophobic sublayer in the post-treatment of the GDL. It was concluded that selection of GDL as the fuel cell electrode is crucial when Pt catalyst is prepared by electrodeposition.

Egetenmeyer *et al.* [64] investigated electrodeposition of cathode catalyst layer using the plasma process. At different catalyst loadings and plasma durations, nanostructured Pt and Pt₃Co cathodes were prepared with varying quantity of ionomer and its distribution in the cathode catalyst layer (CCL). There was an increase of ECSA in comparison with the untreated substrate. ECSA increased with increase in the plasma treatment duration up to $23.1~\text{m}^2~\text{g}^{-1}$ (highest) after 15 min plasma treatment, which is indicative of the deposition of smaller Pt particles on the electrode. Summarized results for the above category are given in Table 6.

Parameter/Variable/Method Pt Loading, mg cm⁻² PtUt, % Ref. **TFCL** 63.6 45.4 0.4 [52] **GDE** 77.8 Nafion® loading 0.2 115 [53] Optimum Nafion® content 0.25 648 cm² 52 [54] Thickness of CL 0.256 91.1 77.9 [55] Thermal reduction(ScCO₂) 173 0.028 74 [56] 0.05 106.10 [57] dc-sputtering parameters dc-magnetron sputtering parameters 47.09 cm² 93.62 [58] Effect of PTFE on electro spun /electro sprayed MEA 0.094 81 [59] Platinum loading 14 126.5 [60] Pore size on OMC/FDC-15 2 70.2 [61] Solvent effect (NMP) 0.2 52.2 [62] Effect of GDL thickness 0.25 193 [63] -Plasma process 0.3 23.1 [64]

Table 6. Optimization of catalyst parameters (PEMFC cathode)

Improving the performance of Pt support materials

The selection of appropriate support materials plays a key role in enhancing the overall performance of PEMFC and DMFC. Characteristics of good support material include presence of surface functional groups that promote catalyst-support interaction, mesoporous structure which improves triple phase boundary (TPB), good electrical conductivity and electrochemical stability, high surface area and corrosion resistance. Typically, conductive and porous membranes are known to possess above mentioned features and are therefore preferred as support materials for Pt catalyst [44].

Existing research reveals that use of carbon-based support with various structural and morphological properties improved stability and electrocatalytic activity of catalyst. In addition, mass transfer and electronic conductivity in CL are also found to be enhanced at carbon supports. Some of the novel carbon-based support materials investigated so far are carbon nanofibers (CNF), ordered mesoporous carbons, carbon aerogels, carbon nanohorns, carbon nanocoils and carbon nanotubes (CNT) [44].

In this connection, Zhao *et al.* [65] demonstrated that nearly 100 % of Pt can be exposed to catalytic activity by using gold nanoparticles as Pt catalyst support (AuPt). ECSA measurements were carried out on Vulcan XC-72 CB samples by varying Pt and Au ratio. Prominent enhancement of ECSA and Pt utilization was observed when Pt/Au ratio becomes lower than 0.2. Further decrease of Pt/Au ratio to 0.05 or less, makes ECSA and PtUt to increase up to 100 %. This approach ensured uniform dispersion of Pt particles and prevented pocketing in the micropores of supported material, making thus Pt particles efficient for ORR.

Kongkanand *et al.* [66] and Orfanidi *et al.* [67] elucidated use of carbon nanotubes (SWCNT) and (MWCNT) as Pt catalyst supports. Pt particles supported on SWCNT showed lower ECSA (17.8 $\rm m^2 g^{-1}$) than the commercial carbon support (33.5 $\rm m^2 g^{-1}$) with 10 mV shift in the onset potential for ORR. They inferred that the commercially available Pt has better distribution of Pt nanoparticles than the one developed in the lab with SWCNT. Pt supported on MWCNT, however, showed improved ECSA of 78.4 $\rm m^2 \, g^{-1}$ with 84 % PtUt. Higher ECSA and better catalytic utilization were attributed to uniform dispersion and narrow particle size distribution (2.5 to 4 nm).

Instead of using pure SWCNT, Zhu *et al.* [68] used a mixture of SWCNT and carbon nanofibers (CNF) at 1:3 (SF13) and 1:5 (SF15) ratios (Bucky paper) to prepare a novel catalyst. They observed reduced ECSA due to larger Pt particle size (6 nm) than of commercial catalyst support (2 nm). However, PtUt

of 88 % and 84 % for SF13, SF15 were observed which was ascribed to availability of the catalyst particles at electrolytic and electronic pathways of the Bucky paper electrodes.

Kou *et al.* [69] investigated the properties of functionalized graphene sheets (FGS) as the cathode catalyst support, mostly because of higher conductivity, high surface area and low manufacturing cost with unique graphitized basal plane structure. Results revealed higher initial ECSA (109 $\text{m}^2\,\text{g}^{-1}$) with improved stability when compared to the commercial catalyst (E-TEK, 75 $\text{m}^2\,\text{g}^{-1}$). This was attributed to smaller Pt particle size of 2 nm and less extent of Pt nanoparticles agglomeration on FGS.

Salernitano *et al.* [70] used the controlled plasma improved chemical vapour deposition (CVD) technique to deposit Pt nanofibers on a support made from carbon nano fibers (CNF). Electrodes were prepared with different structures of CNF, by changing the orientation of graphene layers in relation to the fiber axis. This resulted in availability of large number of active sites for catalyst nanoparticles. Due to the controlled morphology grown of graphite paper, they found higher ECSA (225 $\text{m}^2\,\text{g}^{-1}$) with improved PtUt at reduced Pt loading (0.018 mg cm^{-2}).

Huang *et al.* [71] used conductive titanium oxide as Pt catalyst support and investigated Pt/TiO₂ durability and stability using in-house potential cyclic experiments. Although initially, the Pt/TiO₂ (31.2 $\rm m^2\,g^{-1}$) showed less ECSA than Pt/C (56.4 $\rm m^2\,g^{-1}$), it continued to remain stable even after 4000 cycles with minimum loss in ECSA. On the contrary, Pt/C showed no activity after 2000 potential cycles owing to Pt dissolution, carbon corrosion and Pt particles sintering. ECSA was calculated after 2500 cycles and observed larger ECSA for Pt/TiO₂ than Pt/C catalyst.

Song *et al.* [72] developed the novel compound carbon supported Pt catalyst (Pt/CCS) by introducing ultra-fine porous carbon fibre (UPCF) powder to commercial Pt catalyst as a second carbon support. Partially supported Pt catalyst JM-40 catalyst with particle size 3.4 nm was combined with UPCF. Using CV measurements, it was observed that Pt/CCS-20 showed the highest PtUt with ECSA 71.9 $\rm m^2\,g^{-1}$.

Sanli *et al.* [73] used reduced graphene oxide (rGO) and carbon black hybrid material as Pt support and fabricated a novel cathode structure for PEMFC. Using electrospray technique, they synthesized platinum/reduced graphene oxide (Pt/r-GO) electrocatalyst and platinum/reduced graphene oxide/Vulcan XC-72, Pt/r-GO/VXC-72, hybrid electrocatalyst with 50 wt% r-GO. Comparing the results with air-sprayed electrode, it was observed that Pt supported on the hybrid support (Pt/r-GO/Vulcan XC-72) showed higher PtUt efficiency with relatively low Pt loading. This enhancement of the electro-sprayed hybrid electrode was credited to facile proton and oxygen transport to the catalytic sites, what resulted from electrode morphology and hybrid support structure. Thus, efficient diffusion of reactant gases to the catalytic sites was achieved.

Singh *et al.* [74] used carbon aerogel which was synthesized by impregnating Pt nano particles using the microwave assisted polyol process. Performance and stability were investigated, and results compared with those for commercially available Pt/C (JM-20) having the same Pt loading. ECSA of 73 and 56 m² g⁻¹ for Pt/CA and commercial JM-20, respectively were obtained. It was concluded that good utilization ratio of 82 % could be due to the conducting and mesoporous CA support which has significant role in improving Pt activity and Pt utilization.

Lori *et al.* [75] employed the modified polymer-assisted deposition (mPAD) technique and synthesized molybdenum carbide (Mo₂C) nano-crystallites without free carbon and used them as the catalyst support, showing ECSA of 28.4 m² g⁻¹. The reason for low ECSA was attributed to formation of aggregates during deposition, making Pt particles inaccessible for reactions.

Ignaszak et al. [76] studied titanium carbide (TiC) and core shelled TiC@TiO₂ material as catalyst supports for Pt and Pt₃Pd alloy (Pt/TiC, Pt₃Pd/TiC, Pt₃Pd/TiC@TiO₂) for ORR activities. They observed

close values of ECSA (40, 41 and 37 $\text{m}^2\,\text{g}^{-1}$) for all three catalysts with no significant difference in electrochemical features. However, $Pt_3Pd/TiC@TiO_2$ retained its activity after 500 cycles, while significant loss of activity was noticed for Pt/TiC and Pt_3Pd/TiC .

To overcome the drawbacks of carbon supports of PEMFC electrodes, Lobato *et al.* [77] prepared MEAs with two non-carbonaceous catalyst supports, SiC and SiCTiC, for PEMFC cathode side and compared the electrochemical performance with carbonaceous support. They observed that catalyst supported on novel materials (Pt/SiC, Pt/SiCTiC) showed excellent electrochemical stability towards environmental corrosion, what was attributed to higher catalyst particle size. Also, at the end of 400 cycles, less ECSA degradation of 19.7 % for Pt/SiC and 17.01 for Pt/SiCTiC was observed when compared to commercial (31.09 %) and homemade (29.82 %) catalysts.

In an effort to find better alternative to carbon support for PEMFC catalyst, Shahgaldi *et al.* [78] synthesized a novel nano composite, titanium encapsulated in carbon nanosperes and carbon titanium core shell structures as cathode catalyst supports, using simple and less costly hydrothermal method. They prepared 10 % and 20 % TiO_2 encapsulated carbon (EC-10, EC-20) and core shell structures (CS-10, CS-20). The electrochemical study revealed that 10 % TiO_2 samples (EC-10, CS-10) showed higher ECSA (414 and 440 m² g⁻¹) than EC-20, CS-20 (280 and 180 m² g⁻¹), suggesting the effect of TiO_2 amount on the active surface area.

Using a new synthesis method, Borchardt *et al.* [79] prepared Pt metal containing silicon carbide derived carbon (CDC-Pt). They reported high ECSA (66 m² g⁻¹) for the synthesized catalyst than conventional Pt/C catalyst and concluded that the deposition of Pt nanoparticle onto carbon matrix provided long term stability with superior corrosion stability. Summarized results for the above category are given in Table 7.

Table 7. Carbonaceous and non-carbonaceous electrocatalysts support materials (PEMFC cathode)

Catalyst support	Pt Loading,mg cm ⁻²	ECSA, m ² g ⁻¹	PtUt, %	Ref.
Gold Nanoparticles(AuPts)	0.012	234.1	99.5	[65]
Single Wall Carbon Nanotubes(SWCNT)	0.014	17.8		[66]
Multiwalled Carbon Nanotubes(MWCNT)	0.005	78.4	84	[67]
Buckypaper	0.09, 0.14	43.3, 39.2	88, 84	[68]
Functionalized graphene sheets(FGS)	20 wt%	109		[69]
CarbonNanoFibers (CNF)	0.3	225		[70]
Titanium oxide	0.4	31.2		[71]
Ultra Porous Carbon Fiber (UPCF)	0.35	71.9	87.2	[72]
Pt/rGO/CB (H75) (hybrid support)	0.5	102		[73]
Carbon Aerogel(Pt/CA)	0.4	73	-	[74]
Molybdenum Carbide(Pt/Mo ₂ C)	0.096	28.4	-	[75]
TiC, TiC@TiO₂(Pt-TiC, Pt₃Pd-TiC-TiO₂)	0.048	40, 36	-	[76]
SiC, SiCTiC (Pt/Sic, Pt/SiCTiC)	0.6	13.36, 13.20		[77]
TiO ₂ , C-TiO ₂ (Pt/TiO ₂ ,Pt/C-TiO ₂)	0.1	414, 440		[78]
Si –CDC (Silicon carbide derived carbon)	12 wt%	66		[79]

Developing Pt metallic alloy and Pt-free catalysts

Pt metal is alloyed with other elements to decrease the overall cost of electrodes. Several studies have been performed to obtain nearly equivalent or better catalytic activity through the introduction of Pt based binary systems such as Pt-Ni, Pt-Fe, and Pt-Co by varying the proportion of Pt and the alloying metal. In addition, the performance of some Pt free catalysts has also been explored [80,81].

Using simple chemical reduction method, Wu *et al.* [82] prepared 20 wt% Pt and nickel (Ni) catalyst with XC-72 conducting furnace black (PtNi/XC-72) and graphene (PtNi/graphene) as carbon supports. From results of chemical characterization, they found that ECSA of catalyst samples are in the following order: Pt/XC-72 < PtNi/graphene < PtNi/XC-72.

Owing to their special electrical properties, PtNi/XC-72 and PtNi/graphene electrodes showed better catalytic activity towards oxygen reduction when compared with Pt/XC-72. PtNi/graphene showed better performance than PtNi/XC-72. Due to enhanced catalyst carbon interaction and high graphite component, graphene has the potential to provide much higher durability than XC-72.

Sahoo *et al.* [83] synthesized doped porous carbon (DPC) with nitrogen and sulphur in a simple and green one-pot process from ionic liquid as the sole source precursor and used as the non-Pt cathode catalyst in PEMFC. The results of half-cell and full cell studies were compared with Pt decorated DPC (Pt/DPC). The ECSA for Pt/DPC and commercial Pt/C after ignoring the role of electric double layer formed between electrode and electrolyte, were 46.88 and 112.34 m² g⁻¹ with Pt utilization efficiency 98.2 % and 60.2 %, respectively. The even distribution of Pt nanoparticles over high surface area and porous support of doped carbon material is stated as a reason for 2.5 times higher ECSA for Pt/DPC when compared to commercial Pt/C.

Wang *et al.* [84] synthesized a variety of Pt–Ni alloy catalysts by potentiostatic electrodeposition. They use an orthogonal array to optimize deposition parameters. Particularly, the electrochemical performance of Pt–Ni alloy catalysts was optimized by dealloying treatment experiment conducted at 0.35 V, 20 min at 50 °C. The results indicated that the deposition time has the most significant impact on the performance of Pt–Ni alloy catalysts. The prepared sample (Pt-Ni) showed the highest ECSA value of 81.7 m² g⁻¹ with the catalyst loading of 0.329 mg cm⁻² (Pt loading of 0.3 mg cm⁻², Ni loading of 0.029 mg cm⁻²). Pt–Ni catalysts were dealloyed by rapid potential cycling, which resulted in a significant refinement of morphology and enhancement of electrocatalytic activity. The sample with low Ni atomic ratio was not suitable for the rapid dealloying treatment.

Pt–Cu (platinum copper alloy) has been studied as a catalytically active material with high surface area, porous platinum structure and hydrogenation promoting property [85].

Bele et al. [86] demonstrated the application of stable and highly active PtCu₃ nanoparticles on the carbon support. The Pt-skin PtCu₃ alloy catalyst was fabricated with core shell nanoparticles having intermetallic ordered shell at a disordered core that is tightly embedded into a carbon support. Consistent ECSA of about 45 m² g⁻¹ is reported with utilization much higher than those already reported in the literature for 3 nm Pt nanoparticles on high surface area carbon supported electrodes. The thermal annealing enables Pt-skin and intermetallic orderings, which are favorable for enhanced activity. The stability is attributed to the firm embedding of Pt-Cu into a heterogeneous carbon matrix caused by the partial oxidation and xerogelation.

Mani *et al.* [87] proposed the technique of surface dealloying as an effective strategy to modify the surface electrocatalaytic properties of platinum. The copper (Cu) surface atoms are dealloyed from $Pt_{25}Cu_{75}$ alloy precursor compound by electrochemical dissolution (voltammetric dealloying to prepare the active catalyst phase). This novel catalyst yielded an ECSA of 75 m² g⁻¹.

Hong *et al.* [88] fabricated a novel electrode, Pd/C@Pt_{skin} (C-U), with electrospun structure by using electrospinning and under potential deposition (UPD) techniques. By in situ deposition of Pt on the surface of Pd-NP in the electrospun Pd/C catalyst layer, they observed that almost all Pt shells become accessible for reactant gases and TPB is optimized with Pt loading of 19 mg cm⁻². The C-U electrode delivered higher peak power density (0.62 W cm⁻²) than conventional electrode (0.55 W cm⁻²) at Pt loading of 100 mg cm⁻². Owing to the nearly 5-fold Pt loading, the conventional electrode showed

better performance than C-U electrode at low current density, however at high current density there was a significant loss of voltage. This was due to the increased oxygen transfer resistance close to Pt surface. Summarized results for the above category are given in Table 8.

Pt metallic alloy & Pt free metal Pt loading, mg cm⁻² ECSA, m² g⁻¹ PtUt, % References PtNi/XC-72 0.2 [82] 93 Pt/DPC 0.2 112 98 [83] Pt- Ni alloy 0.3 81 [84] 0.025 45 Pt-CU₃ [86] 75 Pt₂₅Cu₇₅ 0.169 [87] 92.3 C-U electrode 330 [88]

Table 8. Developing Pt metallic alloy and Pt-free catalysts

Optimization approaches for DMFC cathode

Some approaches for optimizing Pt utilization in DMFC cathode are described below.

Reducing Pt loading and decreasing Pt particle size

Wang *et al.* [89] observed that addition of NaOH to aqueous Nafion® solution suppressed aggregation of large particles and led to smaller agglomerate particle size with uniform distribution of Pt elements in the cathode catalyst layer. Further, they obtained improved ECSA (13.94 m² g⁻¹) and better performance in DMFC.

To enhance Pt utilization, You *et al.* [90] adopted multi step reduction, Pt/C-nR (n = number of reduction steps), to synthesize Pt catalyst with ultra-high Pt loading up to 85 %. CV results revealed that Pt/C-2R catalyst exhibited higher PtUt of 90 % when compared to Pt/C-1R (60 %) with the same Pt loading. Although Pt particles size appears to be larger for Pt/C-1R than Pt/C-nR, the stacked microstructure in Pt/C-1R is stated to favor higher PtUt.

Wang et al. [91] investigated electrochemical oxidation of methanol and reduction of oxygen on the commercial Pt/C catalyst. High catalytic current was observed for ORR with ECSA of 41 m^2g^{-1} .

To improve DMFC performance, Pu *et al.* [92] utilized fabricated Pt nanorod assemblies in double layered cathode with a catalyst loading of 1.0 and 2.0 mg cm⁻² and observed significant increase in ECSA (35.5 m² g⁻¹) and catalyst utilization. The improvement in performance is attributed to the reduction of charge transfer resistance in DMFC, enabling more efficient Pt loading and improving performance of MEA. The increased ECSA is attributed to the reduced size of Pt particles, loose construction of Pt nanorods and embedding of nanorods in the catalyst layer.

Optimization of catalyst parameters

Krishnamurthy et al. [93] studied the performance of DMFC by varying the content of Nafion® in anode CL while keeping it constant on cathode. The optimized results showed the highest catalyst utilization of 65 % at 0.8 Nafion® to carbon (N/C) ratio. Further increase of Nafion® content was reported to result in pore blocking of the catalyst layer which leads to decrease in performance of DMFC.

Krishnamurthy *et al.* [94] studied the influence of PTFE content of anode and cathode CLs on DMFC performance. They examined 5, 10, 20, 30 % PTFE content in cathode CL with anode having constant PTFE content of 20 %. They observed the highest catalyst utilization of 65.54 % for 20 % PTFE and concluded that 20 % PTFE content in the cathode catalyst layer resulted in the maximal catalyst utilization. They also concluded that further increase in PTFE content to 30 % leads to the

blocking of pores of CL, thus reducing oxygen transportation and water removal. The same authors [95] also studied the catalyst utilization by varying Nafion® content. 20 % Pt/C, 40 % Pt/C and platinum black were used as cathode catalysts and the Nafion® content was optimized for each. Based on CV results, the highest value of catalyst utilization of 65 % for 33 % constant Nafion® content with 40 % Pt/C catalyst layer was obtained. No significant influence of Nafion® content on platinum black catalyst was also observed.

Matar *et al.* [96] investigated the effect of thickness of cathode catalyst on DMFC performance. They considered 8.4 μ m thickness layers as standard/base thickness for both anode and cathode with same Pt loadings. Two additional cathode catalyst layers with 19 and 44 μ m were examined. The authors observed decrease of ECSA as thickness of cathode catalyst layer increased and found higher ECSA of 282.88 cm² mg⁻¹ for the standard/base case (8.4 μ m).

Using citrate stabilized method, Jiang et al. [97] prepared 60 % Pt/C catalyst by varying carbon supports and reductants (Pt/XC-72, Pt/BP2000, Pt/XC-72R). They observed that Pt/BP2000 support resulted in higher ECSA (66.46 $\rm m^2~g^{-1}$) with improved catalyst utilization. The difference in performance was attributed to the addition of chloroplatinic acid solution to citrate which contributed to formation of small Pt particles corresponding to large specific surface area with high ECSA and catalytic activity.

Moore *et al.* [98] investigated catalytic activity of DMFC in terms of morphology of porous cathode catalyst substrate. They synthesized three electrocatalysts, *i.e.* Pt/C-Celatum (a macro porous carbon substrate), Pt/CMK-3 (a mesoporous carbon substrate), and Pt/Vulcan XC-72 (a micro porous carbon substrate). After CV studies, they observed major variation between active surface area and total surface area for Nafion® impregnated sample (Pt/C-Celatum). It was concluded that the difference is due to reduced contact between Nafion® electrolyte and catalyst surface, blockage of the pores, and poor accessibility of protons between crystalline platinum and carbon substrate, which all led to low Pt utilization.

Zhao *et al.* [99] employed an electrochemical technique to investigate the influence of Nafion® ionomer content (10, 20, 30, 40, and 50 wt%) catalyst layers on the cathode performance. They found the highest ECSA (27 m² g⁻¹) and catalyst utilization (40 %) at 30 wt% Nafion® content with less difference between the highest and lowest ECSA and concluded that Nafion® content has less effect on ECSA and PtUt in 10-50 wt% range. Figure 8 illustrates the effect of Nafion® content on ECSA and Pt catalyst utilization.

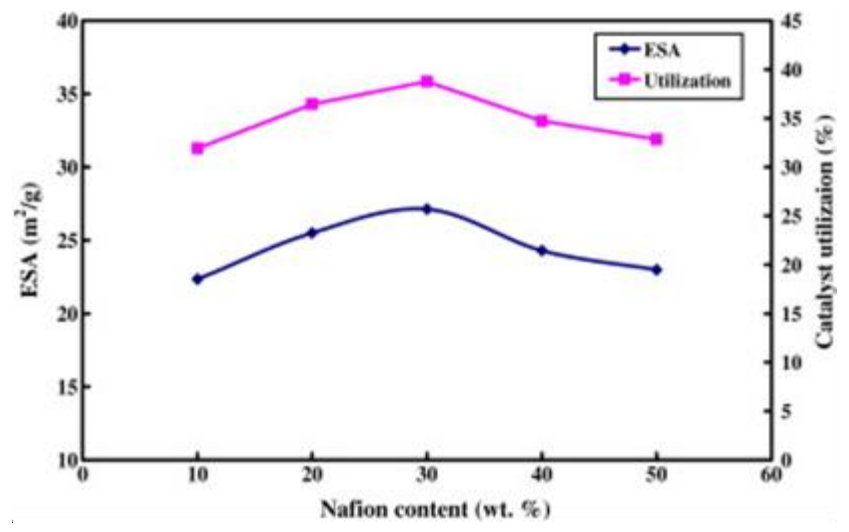


Figure 8. Effect of Nafion® content on Pt utilization and ECSA (marked as ESA on the graph).

Reproduced from [99] with permission from Elsevier

Using various novel catalyst support materials

Wang et al. [100] fabricated DMFC cathode using high surface area SWCNT (Pt/SWCNT) to increase the triple phase boundary sites. Pt/SWCNT was prepared using ion exchange (IE) method and the performance with borohydride (BH) synthesis method was compared. They observed improved Pt utilization and concluded that entire catalyst particles were loaded on SWCNT support, being well dispersed (by IE method) and electrochemically active.

Chen *et al.* [101] used microwave digestion modified carbon nanotubes (CNT) on CC as the catalyst support. Larger ECSA than the others were found, which is attributed to higher Pt dispersion and uniform distribution of Pt nanoparticles.

Yaldagard *et al.* [102] studied the performance of Pt electrocatalyst supported on the protonated polyaniline (PANI) coated tungsten carbide (WC) nano composite and compared the results with the commercial Pt/C electrocatalyst. High Pt utilization of 77 % compared to the commercial one was found, and this improvement was attributed to the synergic effect between Pt nanoparticles and WC.

Jafri *et al.* [103] synthesized nitrogen doped graphene to support Pt catalyst. They used MWCNT spacer to remove face to face agglomeration, what cleaned graphene sheets. Two types of samples, Pt/NGA800+MWCNT, Pt/NG180+MWCNT, were prepared using thermal solid state and hydrothermal methods and compared the results with samples without MWCNT spacer (Pt/NGA800, Pt/NG180). The authors observed 10 % improvement in ECSA and 55 and 54 % Pt utilization and concluded that the addition of MWCNT spacer provided good accessibility to the catalyst active site and nitrogen doped CNT, what resulted in decomposition of reactive intermediates like H_2O_2 into O_2 during ORR.

Algere *et al.* [104] investigated sulfurized carbon xerogels (S-CXG) as the support material for Pt. The highest catalytic activity was observed for Pt/CXG-3S (3 wt% sulphur content) because of right balance of high ECSA (59.0 $\rm m^2\,g^{-1}$) and good intrinsic activity. It was found that Pt/CXG-3S exhibited better catalytic activity than Pt/CXG without sulfurization or Vulcan.

Tesfu *et al.* [105] investigated the use of mesoporous structured hollow graphitized carbon spheres (HGS) as DMFC cathode catalyst support material in 100-150 °C temperature range. Pt/HGS catalyst showed improved ECSA and double layer capacity values which is attributed to higher accessibility of Pt particles. However, large decrease in ECSA (60 % compared to 14 % for Pt/Vulcan) was observed at thermal treatment beyond 850 °C. They inferred that this does not correlate with increased particle size and concluded that during thermal treatment, the decomposition of HGS carbon structure resulted in the blockage of pores, making Pt active sites inaccessible to the electrolyte.

Developing Pt metallic alloy and Pt-free catalysts

Hosseini *et al.* [106] synthesized Ni/Pt/C electrocatalyst using sodium borohydride as the reducing agent and sodium dodecyl sulphate (SDS) as a structure directing agent. This electrode exhibited improved catalytic activity than NiPt/C catalyst. ECSA of 41 % (Ni/Pt/C) and 16.8 $\rm m^2\,g^{-1}$ (NiPt/C), respectively, were recorded. Core shell structure of the prepared catalyst was stated as the reason for the increased ECSA and current density. Summarized results for the above category are given in Table 9.

GDE/structure/support/membrane/ parameters Pt loading, mg cm⁻² ECSA, m² g⁻¹ PtUt, % Ref. Reducing platinum loading and decreasing Pt size 13.94 [89] Effect of Nafion® ionomer aggregation 6.3 Multi Reduction method Pt(76)/C-1R /Pt(76)/C-2R 2.0 60.2 /65.3 68 / 90 [90] **PtNT** 41 [91] Double layered catalyst based MEA 1.0, 2.0 35.5, 34.3 [92] **Optimization of catalyst parameters** Nafion® to carbon (N/C) ratio 2.0 [93] 6 Effect of Polytetrafluoroethylene(PTFE) 2.0 57.0 65.54 [94] Effect of Nafion® content 40 wt% 67.03 65.12 [95] [96] Cathode catalyst layer thickness 1 28.3 Citrate-stabilized method with different reductants 2.8 66.46 [97] and carbon supports (Pt/BP2000) Effect of the cathode catalyst substrate morphology 1 33.4 25.1 % [98] (Pt/Vulcan XC-72) 2 [99] Influence of ionomer content(30 % Nafion®) 28 40 % Using various novel catalyst support materials 129.6 cm² [100] Pt/SWCNT 11.8 wt% 90 % Pt/MWCNT 0.3 23.9 cm² 25.1 % [101] Pt/PANI/WC/C 20.46 [102] 77 % Nitrogen doped graphene with MWCNT spacer 0.42 47 55 % [103] (Pt/NG1800+MWCNT) [104] Carbon Xerogels (CXG) 20 wt% 59.0 HGS [105] 2

Table 9. Platinum utilization for DMFC cathode

Optimization approaches for DMFC anode

Some approaches to optimizing Pt utilization in DMFC anode are given below.

Optimization of catalyst parameters

Liang *et al.* [107] electrochemically deposited Pt nanowires into partial layer of nano Nafion® membrane and formed Pt nanowire network. CV tests showed large ECSA for Pt Nafion® integrated electrodes than conventional E-TEK electrode. Initial results revealed higher ECSA for Pt-Nafion® integrated electrode and a low rate of methanol. Utilization of methanol during the discharge of cell and increased membrane tortuosity are attributed as reasons for enhancement of the catalytic activity.

Scibioh *et al.* [108] explored the ionomer coating (1, 2, 5 wt%) on Ketjen Black EC 300JD (EC), Vulcan XC-72R (VC) and Black Pearls 2000C (BP) carbon supports with different surface area and pore characteristics. They observed better performance for EC5 (Ketjen Black EC 300JD coated with 5 wt% Nafion®) due to extension of TPB, resulting from the improved interaction between catalyst particles and ionomer.

Pu *et al.* [109] employed a thermal imprint technology to prepare passive DMFC using Nafion® 115 membrane on the anode side. The anode catalyst utilization was found to be improved with improved ECSA, which is credited to the additionally increased roughness factor of membrane. They concluded that catalyst utilization at the anode can be improved by using patterned membranes H_4 , H_6 , H_{10} , with pore depths of 4, 6, 10 μ m and roughness factors 2.7, 4.6, 5.4 and observed the highest ECSA for H_{10} membrane.

Kaplan *et al.* [110] studied platinum utilization on methanol-oxidation surface by varying Pt:Ru surface composition. Carbon-supported catalysts with iridium-nickel cores and varying atomic-ratio platinum ruthenium shells ($Pt_{25}Ru_{75}$ to $Pt_{80}Ru_{20}$) were synthesized. The ECSA values obtained for the studied catalysts were 50 m² g_{PtRul}⁻¹ for the commercial catalyst, 35 m²g_{PtRul}⁻¹ for $Pt_{13}Ru_{22}$, 28 m² g_{PtRul}⁻¹

for $Pt_{16}Ru_{14}$, 27 m² g_{PtRulr}^{-1} for $Pt_{23}Ru_{9}$, and 27 m² g_{PtRulr}^{-1} for $Pt_{28}Ru_{7}$. The highest mass activity was obtained for $Pt_{13}Ru_{22}$ despite its 23 % lower surface activity compared to $Pt_{16}Ru_{14}$. This was explained by better Pt utilization of $Pt_{13}Ru_{22}$ compared to $Pt_{16}Ru_{14}$. This result demonstrated higher platinum utilization of the core shell structure and possible reduction of Pt loading with use of core—shell catalysts. The authors stated that further improvement can be achieved by enhancing Pt utilization with the highest surface activity and optimal PtRu ratio. This can be done by reducing Pt wt% while adjusting ruthenium wt% accordingly, in order to maintain the favorable surface Pt/Ru ratio.

Lin et al. [111] used a newly developed active screen plasma (ASP) technique to examine the effect of temperature and treatment duration on the growth of Pt nanowires on the GDL surface. They observed that starting from 100 °C temperature onwards, ECSA increased expressively, showing a maximum at 150 °C, and decreased before further increase of temperatures between 180 and 210 °C. The ECSA for samples treated at 150 °C was observed to be 65 % higher when compared with untreated one, indicating the influence of temperature on Pt nanowire growth.

Alcaide *et al.* [112] studied the influence of solvent on the catalyst inks for active layer manufacturing in DMFC applications. Two types of solvents, 2-propanol (IPA) and n-butyl acetate (NBA), have been used. The ECSA determined by CO stripping were 52.4 and 47.3 m² g⁻¹, *i.e.* about 11 % greater ECSA was found for NBA than IPA. Results indicate that the ECSA of CL formulated with NBA was higher than that formulated with IPA. This clearly indicates that secondary pores in the catalyst formulated with NBA make accessible a greater surface area of the catalyst.

Using various novel catalyst support materials

Han *et al.* [113] tested the performance of DMFC anode with three different support materials. They prepared Pt-Ru electrocatalyst with acetylene black, Vulcan XC-72 and Ketjin Black EC-300J as carbon supports. They found small particle size, good dispersion and high methanol oxidation activity for Ketjin Black carbon support with 80 wt% Pt content, thus leading to higher ECSA and better Pt utilization. Pt-Ru supported on acetylene black has the lowest activity because of large clusters of nanoparticles caused by agglomeration. In contrast, Pt-Ru supported on Ketjen Black having better dispersion, exhibited three-fold increase in catalytic activity when compared to P-Ru/acetylene black.

Sun *et al.* [114] synthesized OMC-FT, OMC-F ordered mesoporous carbon with varying pore framework. Higher ECSA and good stability was observed for OMC-FT/Pt (62.96 $\rm m^2\,g^{-1}$) than OMCs-F/Pt (54.36 $\rm m^2\,g^{-1}$). Uniform dispersion of Pt nanoparticles resulted from high surface area and increased meso-porosity lead to high Pt utilization.

To avoid the waste of noble catalysts, Carmo *et al.* [115] used nitric acid incorporated carbon black support to prepare Pt/Ru electrocatalyst (PtRu/C-HNO₃). They observed better nano particle distribution on the catalyst support with high affinity and more exposed area of Ru towards species containing oxygen, leading to better ECSA of $104 \text{ m}^2\text{ g}^{-1}$ with better Pt utilization.

Luo *et al.* [116] prepared a Pt-Nafion® high performance catalyst carbon support functionalized by perflourosulfonic acid and compared the results with Pt/O-C and Pt-Nafion®/C catalysts. They observed 30 % higher ECSA of 104.9 mg cm⁻² for Pt-Nafion®/C catalyst when compared to Pt/O-C. The presence of Nafion® leads to higher dispersion of Pt nanoparticles and increased ECSA.

Liu *et al.* [117] used multi walled carbon nanotubes doped with phosphorous (P-MWCNT) as the catalyst support and prepared Pt/P-MWCNT electrode for DMFC. Improved Pt particles dispersion with increased intrinsic activity resulting in high Pt utilization was observed. This was attributed to change of charge density of P-MWCNT, leading to better interfacial interaction between surfaces of Pt and P-MWCNT.

Sun *et al.* [118] designed and synthesized 1D open Pt structures with porous surface. Using polyelectrolyte-modified FeOOH nanorods as a template, they prepared hollow Pt nanotubes (PtNT). Employing the electrostatic attraction-based layer-by-layer assembly process, the self-supporting porous electrode was synthesized. ECSA of $19.6 \, \mathrm{m^2 \, g^{-1}}$ was observed for this electrode when compared to $16.8 \, \mathrm{m^2 \, g^{-1}}$ of Pt black catalyst. In spite of similar structure and composition of these electrodes, the increased ECSA was attributed to 1D porous structure of the prepared electrode.

Using chemical interfacial method, Gharibi *et al.* [119] prepared a composite of polyaniline (PANI) fiber doped with para-toluenesulfonic acid (PTSA) and fabricated the vulcan-polyaniline composite, C-PANI-PTSA. Pt electrocatalyst was deposited on the composite with different ratios (10, 15, 20, 25, 30 wt%), optimized and compared with Pt/C electrocatalyst. They found high ECSA (120.5 m² g⁻¹) for Pt/C-20 % PANI-PTSA electrocatalyst. C-PANI-PTSA composite exhibited better dispersion of Pt particles resulting in increased ECSA.

For depositing Pt nanoparticles, Li *et al.* [120] prepared a hybrid support $Ti_xS_{n1-x}O_2$ -C *via* thermal method with substitution of Ti^{4+} by Sn^{4+} in TiO_2 lattice and observed improved Pt utilization with increased ECSA (68.9 m² g⁻¹) compared to the commercial catalyst.

Patel et al. [121] used the complexed sol-gel (CSG) process to synthesize Pt/Ru/TiN anode catalyst with titanium nitride (TiN) as the support. Higher ECSA of 59 $\rm m^2\,g^{-1}$ than the commercial catalyst was observed with uniform dispersion of Pt/Ru on the support. It was stated that the CSG process resulted in generation of the nanocrystalline Pt/Ru on the support.

Zhang *et al.* [122] used nitrogen-doped carbon nanotubes (CN_x-NTs) as the catalyst support material. They were prepared by carbonization of PPy-NT which were synthesized using methyl orange as a structure-guiding agent. ECSA values observed for these catalysts are 44.4 m² g⁻¹ (Pt/CN_x-NTs-600), 55.9 m² g⁻¹ (Pt/CN_x-NTs-700), 94.0 m² g⁻¹ (Pt/CN_x-NTs-800) and 71.2 m² g⁻¹ (Pt/CN_x-NTs-900). The highest catalytic activity of Pt/CN_x-NTs-800 catalyst is attributed to the optimal proportion of N-5, N-6 and N-Q.

Gao *et al.* [123] used graphene/Vulcan XC-72 carbon as the catalyst support and prepared platinum/graphene/Vulcan XC-72 (Pt/Gr-C) catalyst. Graphene oxide (GO) and H_2 PtCl₆ were simultaneously reduced in ethylene glycol. Then, through ultra-sonication in aqueous solution, low-cost Vulcan XC-72 carbon was incorporated between graphene sheets. ECSA values of 37.9 m² g⁻¹ (Pt/C), 41.8 m² g⁻¹ (Pt/Gr) and 50.5 m² g⁻¹ (Pt/Gr-C), respectively were obtained. The best result for Pt/Gr-C was attributed to the inhibition effect of Vulcan XC-72 carbon sphere on the overlap of graphene and smaller particle size.

To increase the methanol oxidation activity of Pt catalyst, Jeon *et al.* [124] developed Pt/WC/C catalyst and analyzed electrochemical properties. CO-stripping studies revealed ECSA of 3.8 m 2 g $^{-1}$ for Pt/WC/C catalyst and 5.9 m 2 g $^{-1}$ for the conventional Pt/C. Higher ECSA (7.5 m 2 g $^{-1}$) was recorded for Pt/WC/C and not much different ECSA was observed for Pt/C (5.6 m 2 g $^{-1}$) when hydrogen adsorption method was used. Difference in ECSA observed by two methods was due to H $^+$ spill-over at the synthesized Pt/WC/C catalyst. Further, from CO stripping studies the reduced potential of 0.68 V for the synthesized catalyst Pt/WC/C than Pt/C (0.8 V) was found, indicating improved Pt/WC/C activity towards CO electro-oxidation.

Developing Pt metallic alloy and Pt-free catalysts

Giorgi et al. [125] deposited PtAu bimetallic nanoparticles on carbon nano fibers (CNF) directly grown on graphite paper and observed three times increase in the performance than for the commercial carbon support electrode having Pt utilization of 11 %. The augmented catalytic action of this

electrode when compared to PtRu catalyst was attributed to increased utilization of catalyst particles, which leads to superior ability towards methanol oxidation. The specific morphology of platelet CNF reduces amalgamation and regulates a robust foundation of catalyst nanoparticles on the substrate. In addition, the surface of the nanofibers is encompassed by functional groups which enable better oxidation, leading to the reduction of carbon-based species like CO that are accumulated on the electrode. Thereby Pt poisoning during cell operation is reduced and stability is enhanced.

Jang *et al.* [126] deposited Pt-Au alloy nanoparticles on graphene to prepare three-dimensional graphene electrodes (3D-GR/PtAu). Using the spraying and evaporation technique, Pt-Au alloy is deposited on colloidal graphene by employing the aerosol process. The ECSA (92 to 325 m² g⁻¹) values were found to increase with decrease in graphene oxide concentration (0.5 to 0.1 wt%). The highest ECSA of 325 m² g⁻¹ obtained for this electrode was relatively higher than for two-dimensional graphene electrode (2D-GR/PtAu) and commercially available Pt/C catalyst. This is attributed to increased active reaction sites, resulting in greater ability towards methanol oxidation.

Chang et al. [127-130] demonstrated anode catalyst for DMFC methanol electro oxidation using Ni_2P , CoP promoters. They synthesized $Pt-Ni_2P$, Pt-CoP and Pt-CoP and Pt-CoP by Co-depositing Ni_2P , CoP promoters with Pt and Pt-CoP and Pt-CoP and Pt-CoP and Pt-CoP and Pt-CoP promoters by varying the amount of promoters (10, 20 30, 40 and 50 %). From H-adsorption and CO stripping measurements, they observed maximum ECSA for 30 % loading promoter for $Pt-Ni_2P$, Pt-CoP catalyst and 40 % loading of promoter for Pt-CoP and Pt-CoP, respectively. The CV results are shown in Figure 9. The enhanced results were attributed to electron transfer between catalyst promoters and Pt-CoP and Pt-CoP results are summarized in Table 10.

Table 10. Platinum utilization analysis for DMFC anode

GDE/structure/support/membrane/parameters	Pt loading, mg cm ⁻²	ECSA, m ² g ⁻¹	Ref.
Nano-Nafion® membrane	4	11.5	[107]
Ionomer coating (5 wt%)	40 wt%	63.0	[108]
Roughness Factor(RF)	1.0	45.8	[109]
Atomic ratio	0.7	35	[110]
Plasma treatment conditions	-	25.8	[111]
Effect of solvent:	0.8	52.4	[112]
P-Ru/Ketjen Blank	5	45.63	[113]
Ordered mesoporous carbon	20 wt%	6296	[114]
Nitric acid functionalized CB/Vulcan XC72R-HNO ₃	20 wt%	104	[115]
Nafion® functionalized CB (Pt/Nafion®-C)	20 mg	104.9	[116]
Phosphorous doped CNT(Pt/P-MWCNT)	-	78.9	[117]
1D open - Pt structures with porous surface(PtNTs)	0.028	19.6	[118]
Pt/C-PANI-PTSA	0.1	120	[119]
SnO ₂ -TiO ₂	1	68.9	[120]
Nanostructures TiN	0.3	59	[121]
Pt/CNx-NTS-800	5.3 wt%	94.0	[122]
Pt/Gr-C	0.019	50.5	[123]
Pt/WC/C	-	3.8	[124]
Platelet Carbon Nano fiber grown on graphite paper.	0.011	59	[125]
3D-GR/PtAu	20 wt%	325	[126]
Pt-Ni ₂ P-30 %	5	69	[127]
PtRu-Ni ₂ P-40 %	2	113	[128]
Pt-CoP-30 %	0.3	81	[129]
PtRu-CoP-40 %	2	116	[130]

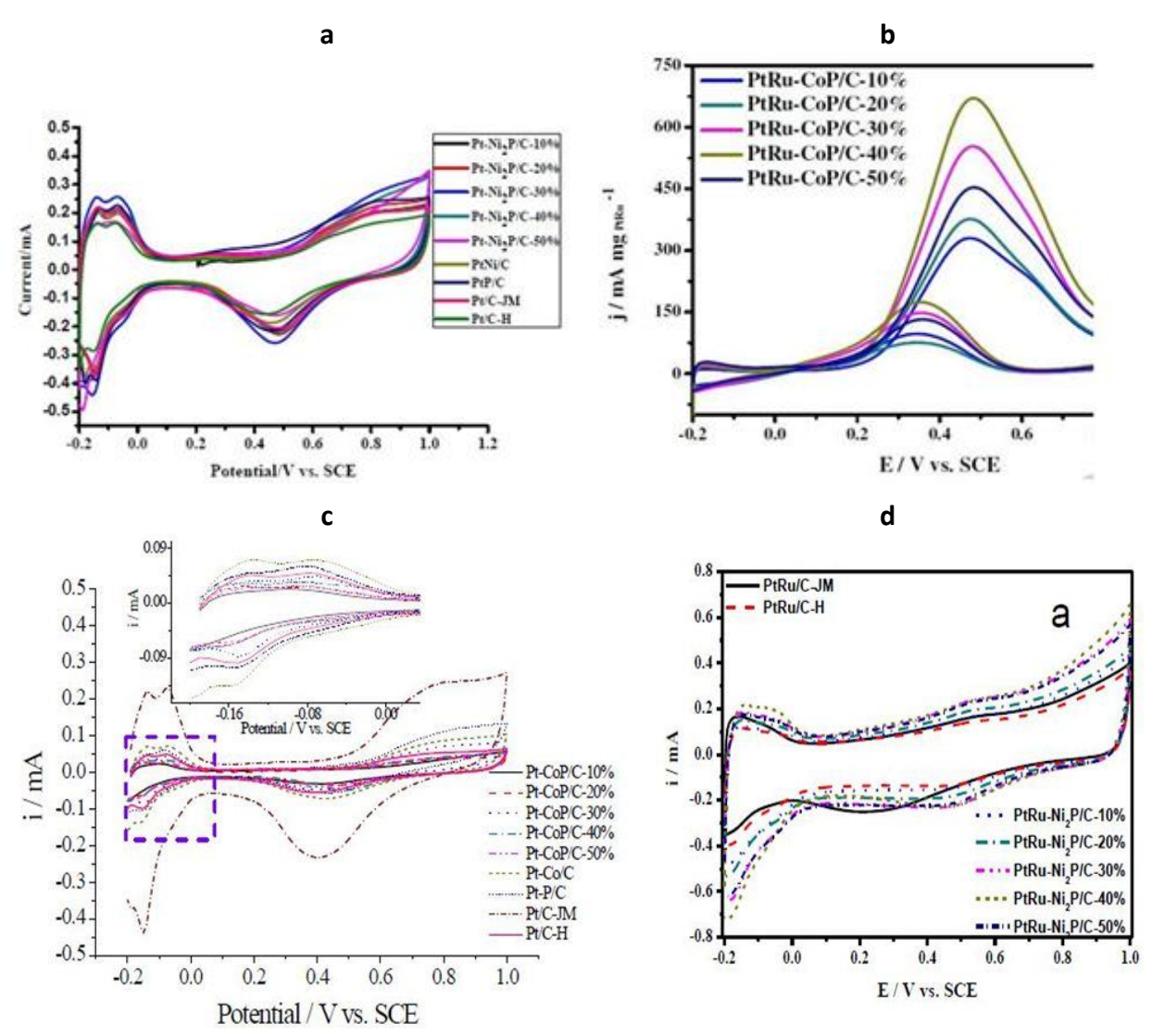


Figure 9. Cyclic voltammograms of (a) Pt-Ni₂P (b) PtRu-CoP/C (c) Pt-CoP/C (d) PtRu-Ni₂P for varying amount of promoters (10, 20, 30, 40 and 50 %).

Conclusion

This review has summarized various approaches adopted by researches over the past two decades to enhance Pt utilization efficiency and thereby reduce cost and address various other technical barriers for PEMFC's and DMFC's to become commercially viable. It is established that catalysis is a surface phenomenon on electrodes, where catalyst activity is largely governed by the dispersion of particles, particle size and the exposed percentage of particles available in the catalyst layer. For this reason, and in order to reduce Pt loading, it is essential that efforts must be made to use all Pt particles during reaction. Reducing particle size can therefore be seen as the primary focus of research so far in the area of catalyst utilization.

It is well known that the exposed percentage of the catalyst available for catalytic activity is the reciprocal of particle size. This means that reducing the particle size to below 1 nm levels may lead to 100 % Pt utilization. However, research revealed that the porous structure of the carbon support with the pore size at approximately 2 nm is a hindrance. That is, reduction of Pt particle size below 2 nm lowers its specific activity and results in the pocketing of the particles inside the porous structure of the carbon support, rendering them inaccessible for catalyst reaction. Further, the behavior of metal particles smaller than 1 nm display greater interaction with the carbon support in deviation of their normal conventional behavior thereby reducing their participation in electroactivity.

Nevertheless, the recent progress in catalyst utilization research has brought down the effective particle size of platinum-based catalyst to about 2-4 nm range and the percentage of exposed Pt particles to the range of 20-50 %. This has been achieved through the following means:

- Increasing of TPB, where electrolyte, electrode and fuel gas come into contact with each other, by optimizing the composition of the catalyst layer and catalyst distribution.
- Attainment of reduced mass transport losses by controlling pore structure and hydrophobicity especially at high current density of CL to provide more electrochemical reaction area with improved gas and liquid transport pathways.
- Reducing of the interfacial resistance by tailoring CL and GDL, and between CL and membrane interfacial structures
- Designing novel methods for ordered CL preparation.

As it was established that reducing the particle size may not result in optimizing catalyst utilization, other viable alternatives need to be explored. In addition to the use of Pt and Pt alloy as a catalyst, efforts are also being carried out to investigate the application of non-Pt alloys as catalysts to reduce the overall cost of the fuel cell.

Also, it is worth mentioning here that recent research indicates stability or the life span of PEMFC as the most important factor, irrespective of Pt loading per area. This means that as long as high Pt loading contributes to increase in stability, life span and the overall effectiveness of the fuel cell, a reduction of Pt loading should not be prioritized. Nevertheless, development of Pt electrocatalyst with low Pt loading will continue to stay in the focus of active research.

NOMENCLATURE

1D	one dimensional	HD-EG	homogeneous deposition of ethylene glycol
ASP	active screen plasma	HGS	hollow graphitized carbon spheres
AST	accelerated stress test	IE	ion-exchange
AuPt	gold nanoparticles supporting Pt	IPA	isopropyl alcohol
ВН	borohydride	LSV	linear sweep voltammetry
BP	black pearl	MEA	membrane electrode assembly
CA	carbon aerogels	mPAD	modified polymer-assisted deposition
СВ	carbon black	MPL	microporous layer
CCL	cathode catalyst layer	MWCNT	multiwalled carbon nanotubes
CCS	catalyst coated substrate	N/C	Nafion® carbon ratio
CC	carbon cloth	$NaBH_4$	sodium borohydride
CCS-20	compound carbon support	NCS	novel cathode structure
CL	catalyst layer	NDCL	novel double catalyst layer
CMK	a family of mesoporous material	NMP	N-Methyl-2-pyrrolidoone
CMPL	carbon microporous layer	OMC	ordered mesoporous carbon
CNF	carbon nanofibers	ORR	oxygen reduction reaction
CNT	carbon nanotubes	PEMFC	proton exchange membrane fuel cell
CO_{ad}	adsorbed carbon monoxide	PGM	platinum group metal
CP	carbon paper	PLD	pulse laser deposition technique
CTAB	centyl trimethyl ammonia bromide	PPT	pulse plating technique
CV	cyclic voltammetry	PtUt	platinum utilization
CVD	chemical vapor deposition	PTFE	poly tetra flouro ethylene
CXG	carbon xerogels	PtNP	platinum nanoparticles
DCL	double catalyst layer	PtNT	platinum nanotubes
DC	direct current	PTSA	para sulfonic acid
DMFC	direct methanol fuel cell	rGO	reduced graphene oxide
DPC	doped porous carbon	ScCO ₂	super critical carbon dioxide
E/E	electrospinning and electrospraying	SCL	single catalyst layer

ECSA	electrochemical active surface area	SDS	sodium dodecyl sulphate
EG	ethylene glycol	SENS	surface enriched nanosized
FGS	functionalized graphene sheets	SWCNT	single walled carbon nanotubes
GDE	gas diffusion electrode	TCS	traditional catalyst structure
GDL	gas diffusion layer	TFCL	thin film catalyst layer
GO	graphene oxide	TPB	triple phase boundary
Gr	graphene	UPCF	ultrafine porous carbon fibre
GSA	geometrical specific surface area	HUPD	hydrogen under potential deposition

References

- [1] C. Berger, Handbook of Fuel Cell Technology, Prentice-Hall, NJ, United States, 1968.
- [2] T. Zhao, C. Xu, Fuel cells: direct methanol fuel cell: overview performance and operational conditions, J. Garche, Oxford: Elsevier, Amsterdam, 2009, p.381–389.
- [3] S. J. Peighambardoust, S. Rowshanzamir, M. Amjadi, *International Journal of Hydrogen Energy* **35** (2010)9349-84.
- [4] V. Mehta, J. S. Cooper, *Journal of Power Sources* **114** (2003) 32-53.
- [5] K. V. Schaller, C. Gruber, Fuel Cells Bulletin 3 (2000) 9-13.
- [6] F. Panik, Journal of Power Sources **71** (1998) 36-8.
- [7] K. Sopian, W. R. Daud, Renewable Energy 31 (2006) 719-27.
- [8] S. Litster, G. McLean, Journal of Power Sources 130 (2004) 61-76.
- [9] Z. Liu, L. Ma, J. Zhang, K. Hongsirikarn, J. G. Goodwin, *Catalysis Reviews* **55** (2013) 255-88.
- [10] I.E. Stephens, A. S. Bondarenko, U. Grønbjerg, J. Rossmeisl, I. Chorkendorff, *Energy and Environmental Science* **5** (2012) 6744-62.
- [11] U.S. Dept. of Energy. Fuel cell hand book, 7th ed., West Virginia: Office of Fossil Fuel, *National Energy Technology Laboratory*; October 2000.
- [12] De Frank Bruijn, G.J. Janssen, *PEM fuel cell materials: Costs, performance and durability.* Springer, New York, 2013, p. 249-303.
- [13] A.Lavacchi, H. Miller, F. Vizza, *Nanotechnology in electrocatalysis for energy*, Springer, New York, 2013.
- [14] M. S. Wilson, S. Gottesfeld, *Journal Applied Electrochemistry* **22**(1992) 1-7.
- [15] C.H. Hsu, C.C. Wan, Journal of Power Sources (2003) 268-73.
- [16] G. S. Kumar, M. Raja, S. Parthasarathy, Electrochimica Acta 40 (1995) 285-90.
- [17] D. Thompsett, Catalysts for the proton exchange membrane fuel cell, *Fuel cell technology handbook*. 2003.
- [18] Y. Yi, B. D. Lee, S. K. Kim, D. H. Jung, E.M. Jung, S. M. Hwang, S. Y. Choi, D. H. Peck, *Journal of Electrochemical Science* **11** (2016) 5909-23
- [19] J. Zeng, J.Y. Lee, W. Zhou, *Applied Catalysis A: General* **308** (2006) 99-104.
- [20] U.A. Paulus, Z. Veziridis, B. Schnyder, M. Kuhnke, G.G. Scherer, A. J. Wokaun, *Journal of Electroanalytical Chemistry* **541** (2003) 77-91.
- [21] M. Łukaszewski, M. Soszko, A. Czerwiński, *International Journal of Electrochemical Science* **11** (2016) 4442-69.
- [22] T. Binninger, E. Fabbri, R. Kötz, T.j. Schmidt, Journal Electrochemical Society 61 (2014) H121-8.
- [23] A. Pozio, M. De Francesco, A. Cemmi , F. Cardellini, L. Giorgi, *Journal of Power Sources* **105** (2002) 13-9.
- [24] M. A. Watanabe, S.Motoo, *Journal of Electroanalytical Chemistry and Interfacial Electrochemistry* **60** (1975) 267-73.
- [25] H. A. Gasteiger, W.Gu, R. Makharia, M. F. Mathias, B. Sompalli, Beginning-of-life MEA performance—efficiency loss contributions, *Handbook of fuel cells* 2003.
- [26] T. Vidaković, M. Christov, K. Sundmacher, Electrochimica Acta 18 (2007) 5606-13.
- [27] D. F. Van der Vliet, C. Wang, D. Li, A. P. Paulikas, J. Greeley, R. B. Rankin, D. Strmcnik, D. Tripkovic, N. M. Markovic, V. R. Stamenkovic, *Angewandte Chemie* **124** (2012) 3193-6.
- [28] S. Gamburzev, C. Boyer, A.J. Appleby, Fuel Cells Bulletin 2 (1999) 6-8.

- [29] S. Martin, J.L. Castillo, *International Journal of Hydrogen Energy* **35** (2010) 10446–10451.
- [30] S. Martin, P. L. Garcia-Ybarra, J. L. Castillo, Journal of Power Sources 195 (2010) 2443-9.
- [31] S. Martin, B. Martinez-Vazquez, P.L. Garcia-Ybarra, J.L. Castillo, *Journal of Power Sources* **229** (2013) 179–184.
- [32] X. Wang, F.W. Richey, K.H. Wujcik, Y. A. Elabd, Journal of Power Sources 264 (2014) 42–48.
- [33] S.M. Alia, G. Zhang, D. Kisailus, D. Li, S. Gu, K. Jensen, Y. Yan, *Advanced Functional Materials* **20** (2010) 3742-3746
- [34] H. Su, T. Jao, O. Barron, B.G. Pollet, S. Pasupathi, *Journal of Power Sources* **267** (2014) 155–159.
- [35] Y. Nabil, S. Cavaliere, I. A. Harkness, J. D. Sharman, D. J. Jones, J. Rozière, *Journal of Power Sources* **363** (2017) 20-26.
- [36] Y. Nabil-Moreau, S. Cavaliere, I. Harkness, G. Hards, J. Sharman, D. J. Jones, J. Rozière, *ECS Transactions* **69** (2015) 1221-1226.
- [37] A. Esmaeilifar, S. Rowshanzamir, M.H. Eikani, E. Ghazanfari, Energy 35 (2010) 3941-57.
- [38] A. Smirnova, U. Kitkamthorn, M. Aindow, T. Lemi, Journal of Power Sources 179 (2008) 532–540.
- [39] B. Fang, N.K. Chaudhari, M. Kim, J.H. Kim, J. Yu, *Journal of American Chemical Society* **131** (2009) 15330–15338.
- [40] W. Mróz, B. Budner, W. Tokarz, P. Piela, M.L. Korwin-Pawlowski, *Journal of Power Sources* **273** (2015) 885–893.
- [41] U. Rost, R. Muntean, G. Marginean, C. Merino, R. Diez, N. Vaszilcsin, M. Brodmann, *International Journal of Electrochemical Science* **11** (2016) 9110–9122.
- [42] R. H. Huang, W.K. Chao, R. S. Yu, K. L. Hsueh, F. S. Shieu, Journal of Power Sources 205 (2012) 93–99.
- [43] H. Lv, S. Mu, N.Cheng, M. Pan, Applied Catalysis B: Environmental 100 (2010) 190-196.
- [44] S. Sharma, B.G.Pollet, *Journal of Power Sources* **208** (2012) 96-119.
- [45] H. Su, S. Liao, Y. Wu, *Journal of Power Sources* **195** (2010) 3477–3480.
- [46] Y. Qiu, H. Zhang, H. Zhong, F. Zhang, *International Journal of Hydrogen Energy* **38** (2013) 5836–5844.
- [47] G.S. Avcioglu, B. Ficicilar, A. Bayrakceken, I. Eroglu, *International Journal of Hydrogen Energy* **40** (2015) 7720–7731.
- [48] M. Breitwieser, M. Klingele, B. Britton, S. Holdcroft, R. Zengerle, S. Thiele, *Electrochemistry Communications* **60** (2015) 168-71.
- [49] D. Kaplan, M. Goor, M. Alon, S. Tsizin, L. Burstein, Y. Rosenberg, I. Popov, E. Peled, *Journal of Power Sources* **306** (2016) 219–225.
- [50] G.Y. Chen, C. Wang, Y.J. Lei, J. Zhang, Z. Mao, Z.Q. Mao, J.W. Guo, J. Li, M. Ouyang, *International Journal of Hydrogen Energy* **42** (2017) 29960–29965.
- [51] M. Yaldagard, M. Jahanshah, N. Seghatoleslami, *World Journal of Nano Science and Engineering* **3** (2014) 121.
- [52] X. Cheng, B. Yi, M. Han, J. Zhang, Y. Qiao, J. Yu, *Journal of Power Sources* **79** (1999) 75–81.
- [53] E. Antolini, L. Giorgi, A. Pozio, E. Passalacqua, *Journal of Power Sources* **77** (1999) 136–142.
- [54] G. Sasikumar, J.W. Ihm, H. Ryu, *Journal of Power Sources* **132** (2004) 11–17.
- [55] J. Jiang, B. Yi, Journal of Electroanalytical Chemistry **577** (2005) 107–115.
- [56] A. Bayrakceken, A. Smirnova, U. Kitkamthorn, M. Aindow, L. Turker, I. Eroğlu, C. Erkey, *Chemical Engineering Communications* **196** (2009) 194–203.
- [57] A. Khan, B.K. Nath, J. Chutia, *Electrochimica Acta* **146** (2014) 171–177.
- [58] E. Slavcheva, G. Ganske, G. Topalov, W. Mokwa, U. Schnakenberg, *Applied Surface Science* **255** (2009) 6479–6486.
- [59] X. Wang, F.W. Richey, K.H. Wujcik, R. Ventura, K. Mattson, Y.A. Elabd, *Electrochimica Acta* **139** (2014) 217–224.
- [60] J. Speder, A. Zana, I. Spanos, J.J.K. Kirkensgaard, K. Mortensen, M. Hanzlik, M. Arenz, *Journal of Power Sources* **261** (2014) 14–22.
- [61] G. Zhao, T.S. Zhao, J. Xu, Z. Lin, X. Yan, *International Journal of Hydrogen Energy* **42** (2017) 3325–3334.
- [62] T.H. Kim, J.Y. Yi, C.Y. Jung, E. Jeong, S.C. Yi, *International Journal of Hydrogen Energy* **42** (2017) 478–485.
- [63] C. Ruengkit, N. Tantavichet, *Thin Solid Films* **636** (2017) 116–126.



- [64] A. Egetenmeyer, I. Radev, D. Durneata, M. Baumgärtner, V. Peinecke, H. Natter, R. Hempelmann, International Journal of Hydrogen Energy **42** (2017) 13649–13660.
- [65] D. Zhao, B. Q. Xu, Angewandte Chemie International Edition 45 (2006) 4955-4959.
- [66] A. Kongkanand, S. Kuwabata, G. Girishkumar, P. Kamat, Langmuir 22 (2006) 2392–2396.
- [67] A. Orfanidi, M.K. Daletou, S.G. Neophytides, *Applied Catalysis B: Environmental* **106** (2011) 379–389.
- [68] W. Zhu, D. Ku, J.P. Zheng, Z. Liang, B. Wang, C. Zhang, S. Walsh, G. Au, E.J. Plichta, *Electrochimica Acta* **55** (2010) 2555–2560.
- [69] R. Kou, Y. Shao, D. Wang, M.H. Engelhard, J.H. Kwak, J. Wang, V. V. Viswanathan, C. Wang, Y. Lin, Y. Wang, I.A. Aksay, J. Liu, *Electrochemistry Communications* **11** (2009) 954–957.
- [70] E. Salernitano, L. Giorgi, T. Dikonimos, *International Journal of Hydrogen Energy* **39** (2014) 15005–15016.
- [71] S. Huang, P. Ganesan, B.N. Popov, Applied Catalysis B: Environmental 102 (2011) 71–77.
- [72] J. Song, G. Li, J. Qiao, *Electrochimica Acta* **177** (2015) 174-180.
- [73] L. I. Sanli, V. Bayram, S. Ghobadi, N. Duzen, S A Gursel, *International Journal of Hydrogen Energy* **42** (2017) 1085–1092.
- [74] R. Singh, M.K. Singh, S. Bhartiya, A. Singh, D.K. Kohli, P.C. Ghosh, S. Meenakshi, P.K. Gupta, *International Journal of Hydrogen Energy* **42** (2017) 11110–11117.
- [75] O. Lori, S. Gonen, L. Elbaz, Journal of Electrochemical Society 164 (2017) F825–F830.
- [76] A. Ignaszak, C. Song, W. Zhu, J. Zhang, A. Bauer, R. Baker, V. Neburchilov, S. Ye, S. Campbell. *Electrochimica Acta* **69** (2012) 397-405.
- [77] J.Lobato, H. Zamora, J. Plaza, P. Cañizares, M. A. Rodrigo, *Applied Catalysis B: Environmental* **198** (2016) 516-524.
- [78] S. Shahgaldi, J. Hamelin, Fuel **150** (2015) 645-655.
- [79] L. Borchardt, F. Hasché, M. R. Lohe, M. Oschatz, F. Schmidt, E. Kockrick, C. Ziegler, T. Lescouet, B. Büchner, D. Farrusseng, *Carbon* **50** (2012) 1870.
- [80] H.A.Gasteiger, S.S. Kocha, B. Sompalli, F.T. Wagner, *Applied Catalysis B: Environmental* **56** (2005) 9-35.
- [81] B. Wang, Journal of Power Sources **152** (2005) 1-5.
- [82] H. Wu, D. Wexler, H. Liu, *Material Chemistry Physics* **136** (2012) 845–849.
- [83] M. Sahoo, S. Ramaprabhu, Energy 119 (2017) 1075–1083.
- [84] C. Wang, Z. Lin Chen, A. Wen Tao, H. Zhang, *Journal of Electrochemical Energy Conversion and Storage* **13** (2016) 21001.
- [85] S. Koh, N. Hahn, C. Yu, P. Strasser, Journal of Electrochemical Society 12 (2008) B1281-8.
- [86] M. Bele, P. Jovanovič, A. Pavlišič, B. Jozinović, M. Zorko, A. Rečnik, E. Chernyshova, S. Hočevar, N. Hodnik, M. Gaberšček, *Chemical Communications* **50** (2014) 13124-6.
- [87] P. Mani, R. Srivastava, P. Strasser, Journal of Physical Chemistry C 112 (2008) 2770-8.
- [88] S. Hong, M. Hou, H. Zhang, Y. Jiang, Z. Shao, B. Yi, *Electrochimica Acta* **245** (2017) 403–409.
- [89] S. Wang, G. Sun, Z. Wu, Q. Xin, Journal of Power Sources 165 (2007) 128–133.
- [90] D.J. You, K. Kwon, S.H. Joo, J.H. Kim, J.M. Kim, C. Pak, H. Chang, *International Journal of Hydrogen Energy* **37** (2012) 6880–6885.
- [91] Z.F. Wang, L. Shi, G.Z. Gou, A.P. Fan, C. Xu, L. Zhang, In Advanced Materials and Structural Engineering: *Proceedings of the International Conference on Advanced Materials and Engineering Structural Technology (ICAMEST 2015)*, April 25-26, 2015, Qingdao, China, p. 167. CRC Press, 2016.
- [92] L. Pu, H. Zhang, T. Yuan, Z. Zou, L. Zou, X.-M. Li, H. Yang, *Journal of Power Sources* **276** (2015) 95–101.
- [93] B. Krishnamurthy, S. Deepalochani, K.S. Dhathathreyan, Fuel Cells 8 (2008) 404–409.
- [94] B. Krishnamurthy, S. Deepalochani, *International Journal of Hydrogen Energy* **34** (2009) 446–452.
- [95] B. Krishnamurthy, S. Deepalochani, *Journal of Electrochemical Society* **4** (2009) 386–395.
- [96] S. Matar, H. Liu, *Electrochimica Acta* **56** (2010) 600–606.
- [97] Q. Jiang, Z. Peng, X. Xie, K. Du, G. Hu, Y. Liu, *Transactions of Nonferrous Metals Society of China* **21** (2011) 127–132.
- [98] A.D. Moore, S.M. Holmes, E.P.L. Roberts, RSC Advances 2 (2012) 1669–1674.
- [99] X. Zhao, W. Li, Y. Fu, A. Manthiram, International Journal of Hydrogen Energy 37 (2012) 9845-9852.

- [100] J.J. Wang, G.P. Yin, J. Zhang, Z.B. Wang, Y.Z. Gao, *Electrochimica Acta* **52** (2007) 7042–7050.
- [101] C. Chen, C. Chen, F. Chuang, Electrochemistry Communications 9 (2007) 159–163.
- [102] M. Yaldagard, M. Jahanshahi, N. Seghatoleslami, *Applied Surface Science* **317** (2014) 496–504.
- [103] R.I. Jafri, N. Rajalakshmi, K.S. Dhathathreyan, S. Ramaprabhu, *International Journal of Hydrogen Energy* **40** (2015) 4337–4348.
- [104] C. Alegre, D. Sebastián, M.E. Gálvez, R. Moliner, M.J. Lázaro, *Applied Catalysis B: Environmental* **192** (2016) 260–267.
- [105] T. Tesfu-Zeru, M. Sakthivel, J.F. Drillet, Applied Catalysis B: Environmental 204 (2017) 173–184.
- [106] M.G. Hosseini, R. Mahmoodi, *International Journal of Hydrogen Energy* **42** (2017) 10363–10375.
- [107] Z.X. Liang, T.S. Zhao, *Journal of Physical Chemistry* **111** (2007) 8128–8134.
- [108] M.A. Scibioh, I. Oh, T. Lim, S. Hong, H.Y. Ha, Applied Catalysis B: Environmental 77 (2008) 373-385.
- [109] L. Pu, J. Jiang, T. Yuan, J. Chai, H. Zhang, Z. Zou, X.M. Li, H. Yang, *Applied Surface Science* **327** (2015) 205–212.
- [110] D. Kaplan, L. Burstein, I. Popov, E. Peled, *Journal of Electrochemical Society* **163** (2016) F1004–F1010.
- [111] K. Lin, Y. Lu, S. Du, X. Li, H. Dong, International Journal of Hydrogen Energy 41 (2016) 7622–7630.
- [112] F. Alcaide, G. Álvarez, P.L. Cabot, R. Genova-Koleva, H.J. Grande, O. Miguel, *Electrochimica Acta* **231** (2017) 529–538.
- [113] K. Han, J. Lee, H. Kim, *Electrochimica Acta* **52** (2006) 1697–1702.
- [114] Z.-P. Sun, X.-G. Zhang, Y.-Y. Liang, H. Tong, R.L. Xue, S.D. Yang, H.-L. Li, *Journal of Electroanalytical Chemistry* **633** (2009) 1–6.
- [115] M. Carmo, M. Linardi, Applied Catalysis A: General 355 (2009) 132–138.
- [116] F. Luo, S. Liao, D. Chen, *Journal of Energy Chemistry* **22** (2013) 87–92.
- [117] Z. Liu, Q. Shi, F. Peng, H. Wang, R. Zhang, H. Yu, *Electrochemistry Communications* **16** (2012) 73–76.
- [118] H. Sun, L. Qi, X. Jiang, G. Fu, L. Xu, D. Sun, Z. Gu, Y. Tang, New Journal of Chemistry 41 (2017).
- [119] H. Gharibi, M. Amani, H. Pahlavanzadeh, M. Kazemeini, Electrochimica Acta 97 (2013) 216–225.
- [120] Y. Li, C. Liu, Y. Liu, B. Feng, L. Li, H. Pan, W. Kellogg, D. Higgins, G. Wu, *Journal of Power Sources* **286** (2015) 354–361.
- [121] P.P. Patel, M.K. Datta, P.H. Jampani, D. Hong, J.A. Poston, A. Manivannan, P.N. Kumta, *Journal of Power Sources* **293** (2015) 437–446.
- [122] L. M. Zhang, X. L. Sui, L. Zhao, J.J. Zhang, D. M. Gu, Z. B. Wang, *Carbon* **108** (2016) 561–567.
- [123] H. Gao, L. He, Y. Zhang, S. Zhang, L. Wang, *Ionics (Kiel)* **23** (2017) 435–442.
- [124] M. K. Jeon, K. R. Lee, W. S. Lee, H. Daimon, A. Nakahara, S. I. Woo, *Journal of Power Sources* **185** (2008) 927-931.
- [125] L. Giorgi, E. Salernitano, T. D. Makris, S. Gagliardi, V. Contini, M. De Francesco, *International Journal of Hydrogen Energy* **39** (2014) 21601–21612.
- [126] H. D. Jang, S. K. Kim, H. Chang, J. Choi, B. Cho, E. Hee, J. Choi Huang, Carbon 93 (2015) 869-877.
- [127] J. Chang, L. Feng, C. Liu, W. Xing, X. Hu, Energy & Environmental Science 7 (2014) 1628-1632.
- [128] J. Chang, L. Feng, C. Liu, W. Xing, ChemSusChem 8 (2015) 3340-3347.
- [129] J. Chang, L. Feng, K. Jiang, H. Xue, W. B. Cai, C. Liu, W. Xing, *Journal of Materials Chemistry* A **47** (2016) 18607-18613.
- [130] L. Feng, K. Li, J. Chang, C. Liu, W. Xing, *Nano Energy* **15** (2015) 462-9.

©2019 by the authors; licensee IAPC, Zagreb, Croatia. This article is an open-access article distributed under the terms and conditions of the Creative Commons Attribution license (http://creativecommons.org/licenses/by/4.0/)



Open Access: ISSN 1847-9286

www.jESE-online.org

Original scientific paper

Parametric modeling of microbial fuel cells

Amandeep Singh and Balaji Krishnamurthy[™]

Department of Chemical Engineering, BITS Pilani, Hyderabad 500078, India

Corresponding author: [™]balaji.krishb1@gmail.com

Received: February 27, 2019; Revised: March 27, 2019; Accepted: April 2, 2019

Abstract

Microbial fuel cells use bacteria to generate electrical energy and are used for lower power density applications. This paper studies the effect of operational parameters on the performance of a microbial fuel cell. The effect of length of the anode compartment, inlet acetate concentration, acetate flow rate, temperature, thickness of the membrane and bio-film conductivity on the performance of the fuel cell is modeled. The thickness of the membrane is found to play a very limiting role in affecting the performance of the fuel cell. However, the length of the anode compartment, acetate flow rate and bio-film conductivity are found to play a significant role in the performance of the fuel cell. Model results are compared with experimental data and found to compare well.

Keywords

Microbial fuel cell; hydrogen; bio-film; acetate; carbon dioxide; model

Introduction

Microbial fuel cells (MFCs) are multiphase systems involving biological and electrochemical processes to generate energy. These fuel cells convert chemical energy to electrical energy by the action of microorganisms. Most MFC's are constructed using a bio-anode, bio-cathode and a membrane separating two compartments. MFCs can be divided into two categories; mediated and unmediated. A mediated MFC uses a chemical (mediator) that transfers electrons from the bacteria in the cell to the anode. Unmediated MFC uses electrochemically active bacteria to transfer electrons directly to the anode. MFCs have started to find their usage in wastewater treatment. Modeling the effect of operational and design parameters on the performance of MFCs is critical for enhancing the performance of these fuel cells.

The MFC performance expressed in terms of the polarization curve is affected by several factors, including rates of fuel oxidation, resistance of the circuit, size of the anode compartment, transport of protons through the membrane to the cathode, membrane thickness (resistance), oxygen supply, and the reduction reactions at the cathode. Mathematical models help in studying the effect of

these operational parameters on the performance of MFC. Quite a few models exist in the literature which studied the effect of operational parameters on the performance of MFC. The models which were developed to study MFC behavior can be primarily divided to anode based models and full cell models (which are focusing on both the anode and cathode).

Anode based models

Zhang and Halme [1] have developed one-dimensional anode model based on double chamber configuration. Picioreanu and Scott [2] have developed a two-dimensional model to understand the anode microbial activity. The authors studied the relation between the growing bio-film thickness and the current output. Marcus *et al.* [3] have proposed one-dimensional dynamic conduction based model to study the performance of MFC. The model postulates that conductivity of the bio-film is the major factor in a MFC performance. In both above references, the authors postulated that anode is the limiting factor in a MFC performance. Merkey and Choop [4] created a two-dimensional model to study the relationship between power output and the geometry of the cell. The model simulates the effect of bristle anodes and the way they should be placed in a grid and act on the energy output. Sedaqatvand and Mardanpoura [5] extended Marcus's model with a genetic algorithm which sought to minimize the difference between simulated and experimental data. Jayasinghe and Madhavan [6] simulated an MFC anode using a respiring bio-film. While the active bio-film invests the energy arising from the oxidation of the substrate, the respiring zone is in charge of energy conservation at the anode surface. Pinto *et al.* [7] have modeled the anode of a MFC using different degradation mechanisms for decomposition of acetate substrate.

Models focused both on anode and cathode

Oliviera et al. [8] have developed 1-d mathematical model to study the temperature variation in a MFC. The authors also studied the effect of bio-film thickness on the MFC performance. Cheng et al. [9] have developed a mathematical model to simulate the power loss and the potential drop caused by ohmic resistance of the carbon mesh. Zeng et al. [10] have developed a mathematical model for a two-chamber MFC which studies the dynamic behavior of MFC. The authors suggested that the cathodic reaction is the most significant limiting factor in MFCs. Cai and Liu [11] have studied effects of bio-film porosity and external resistance on the performance of a MFC. The authors postulated that at the startup phase, bio-film porosity plays a crucial role in electricity generation. However, at the steady phase, bio-film porosity plays no role in electricity generation. Mardanpour et al. [12] have studied the performance of a MFC as a function of bacterial transport parameters, bacteria activity, substrate variation, etc. The authors postulated that as the hydraulic diameter of the microchannel decreases, the power generation of the microfluidic MFC increases. Ou and Mench [13] have studied the effect of species diffusion and electrical migration on the performance of a MFC. The authors postulated that the electric field migration has a minimal impact on the performance of MFC. Sobieszuk et al. [14] have studied influence of operational parameters on the MFC performance. The authors have shown that the hydraulic retention time is the most important parameter affecting the effectiveness of MFCs. Yao and Li [15] have developed twodimensional model to study the MFC performance. The authors postulated that the electrical conductivity of the bio-film plays an important role in the MFC performance. Xia at al. [16] wrote a comprehensive review on MFCs. The authors qualified various models describing MFCs as the mechanism based models, bulk liquid models, electrochemical models, bio-film models, electrical models and application based models. Gadkari and Sadhukhan [17] presented a review on the mathematical models describing bio-electrochemical systems. Along with reviewing the conventional models for a study of bio-electrochemical systems, the authors have also reviewed new models such as microbial electrolysis cell, microbial electro-synthesis and microbial desalination cell. Capadaglio *et al.* [18] developed a mathematical model to study the application of MFC in wastewater treatment. The authors have reviewed the reactor configuration, electrochemical and microbiological characterization and operational schemes in the simulation of the MFC usage in wastewater treatment. While the above mentioned models already reported in the currently available and MFC related literature, give an overall perspective about the modeling work, we are primarily focused on developing of an anode model to study the effect of design and operational parameters on the performance of a MFC.

The focus of this paper is to study the effect of operational parameters on the performance of the MFC seen through a polarization curve (cell voltage vs. current density) properties. The decrease in the fuel cell voltage is due to over-potential losses due to activation, ohmic losses and concentration polarization. Concentration polarization losses occur at high current densities due to mass transport limitations. Ohmic losses are primarily seen in the middle of the current density range. These are losses due to the resistance of the membrane, bio-film, etc. Activation losses are usually seen at the beginning of the polarization curve where over-potential losses take place to enable the reaction to happen. Therefore, the objective of this paper is to study the effect of operational parameters of MFC on polarization curves and thereby on the fuel cell performance.

Model development

MFC can be considered as a reactor which transfers the chemical energy stored in an organic substrate into electricity due to the activity of enzymes/organisms. A schematic representation of the MFC is shown in Figure 1 (marks are explained within Nomenclature section). The fuel cell consists of an anode chamber with an electron current collector, a polymer electrolyte membrane and a cathode chamber with an electron current collector. The anolyte fuel, acetate reacts at the anode side with the bacteria to produce carbon dioxide and hydrogen ions. The carbon dioxide moves to the anode exit, while hydrogen ions diffuse across the membrane to the cathode. On the cathode side, the oxygen ions react with hydrogen to form water which is removed from the cathode.

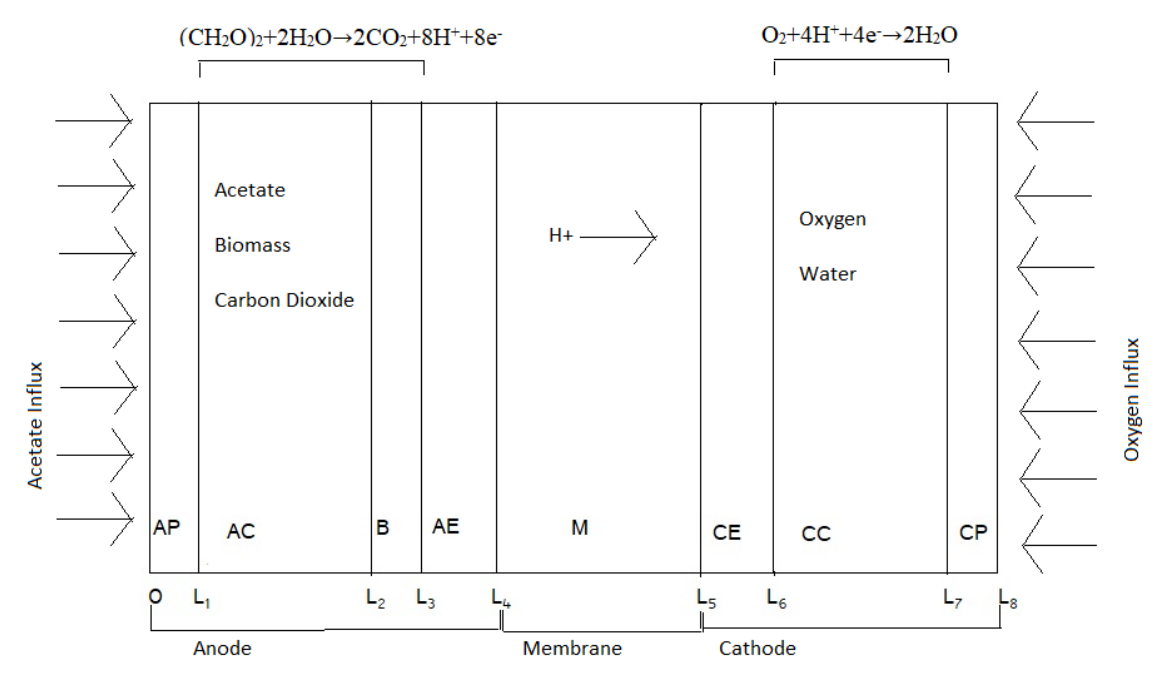


Figure 1. Schematic of a microbial fuel cell (MFC)

The transfer of electrons to the anode occurs by two mechanisms; a mediated electron transfer-MET and direct electron transfer-DET. The anode and cathode reactions containing acetate as the substrate [1] are given by:

$$(CH_2O)_2 + 2H_2O \rightarrow 2CO_2 + 8H^+ + 8e^-$$
 (1)

$$O_2 + 4H^+ + 4e^- \rightarrow 2H_2O$$
 (2)

The overall reaction is given by:

$$(CH_2O)_2 + O_2 \rightarrow 2CO_2 + 2H_2O$$
 (3)

Assumptions

1. Kinetics of the reactions on the anode is represented by Tafel and Monod equations. The Monod equation is typically given by:

$$\mu = \mu_{\text{max}} \frac{S}{K_{\text{S}} + S} \tag{4}$$

where μ is the specific growth rate of the microorganisms, μ_{max} is the maximum specific growth rate of the microorganisms, S is the concentration of the limiting substrate for growth and K_S is the half velocity constant. The Monod equation describes substrate oxidation and microorganism growth. The units of μ , S and K_S are time⁻¹, (mol/volume) and (mass/volume), respectively.

2. The oxygen reduction reaction at the cathode is governed by Tafel equation given by:

$$E - E_{\text{eq}} = \frac{RT}{(1 - \alpha)nF} \ln \frac{i}{i_0} \tag{5}$$

where i and i_0 are the current and exchange current densities for the oxygen reduction reaction.

- 3. The thickness of the bio-film is considered to be constant during simulations. This means that the overall rate of microbial growth through substrate utilization and the overall rate of bio mass loss are in equilibrium.
 - 4. The transport of reactant species through the film is considered as one dimensional.
- 5. The effect of convection in the transport of reactant species in the bio-film and to the electrodes is neglected. The transport of reactant species in the bio-film and to electrodes is assumed to be diffusion, what means that Fick's diffusion laws can be used to evaluate the transport of these species.
- 6. Only hydrogen ions are considered to be transported across the membrane. Carbon dioxide, acetate, oxygen and water are assumed not transported across the membrane.
- 7. Anode and cathode compartments are modeled as a continuous stirred tank reactor—CSTR. This means that mass transport equations are primarily developed from CSTR equations. The mass balance at the anode takes into account rates of reaction in the anode compartment, bio-film and at the electrode.
- 8. The carbon dioxide is considered to be dissolved in solution. Hence the effect of CO₂ in the gas phase is considered negligible.

Model equations

Given that the anode compartment is modeled as CSTR, the transient mass balance equation is given by:

$$\frac{\mathrm{d}m}{\mathrm{d}t} = m_{\mathrm{in}} - m_{\mathrm{out}} + m_{\mathrm{rxn}} \tag{6}$$

In Eq. (4), m_{rxn} represents the mass of reacting species, while m_{in} and m_{out} represent the mass of species entering and leaving the system.

The mass balance of acetate is given by [10]:

$$\frac{\mathrm{d}c_{\mathrm{a}}}{\mathrm{d}t} = \frac{q}{V^{\mathrm{AC}}}(c_{\mathrm{a}}^{\mathrm{0}} - c_{\mathrm{a}}^{\mathrm{AC}}) - r_{\mathrm{a}} \tag{7}$$

The reaction rate of acetate oxidation (degradation) in the anode compartment defined by Eq. (1) is given by:

$$r_{\rm a} = k \exp\left(\frac{\alpha_{\rm a} \eta_{\rm a} F}{RT}\right) \left(\frac{c_{\rm a}^{\rm AC}}{K_{\rm g} + c_{\rm a}^{\rm AC}}\right) c_{\rm x} \tag{8}$$

In Eq. (6), k represents the rate constant, c_a^{AC} represents the concentration of the acetate in the anode compartment and c_x represents the concentration of the bio-mass in the anode compartment. η_a represents the anodic over-potential and K_a represents the half velocity rate constant for acetate.

The transient equations for the acetate mass balance in the anode compartment is obtained by inserting eq. (6) into eq. (5):

$$\frac{dc_a}{dt} = \frac{q}{V^{\text{AC}}} (c_a^0 - c_a^{\text{AC}}) - k \exp\left(\frac{\alpha_a \eta_a F}{RT}\right) \left(\frac{c_a^{\text{AC}}}{K_a + c_a^{\text{AC}}}\right) c_x \tag{9}$$

The first \(\frac{1}{2}\)erm on the right hand side represents the mass flux of acetate in the anode compartment and the second term represents the reaction rate of acetate in the anode compartment. The reaction of acetate to form CO₂ is a bio-electrochemical reaction; the electrochemical part of the reaction is dealt with Tafel equation and the bio-chemical reaction is dealt with Monod equation.

The acetate flux in the bio-film layer can be written as:

$$N_{\rm A} = -D_{\rm A}^{\rm B} \frac{\mathrm{d}c_{\rm ab}}{\mathrm{d}x} \tag{10}$$

Eq. (8) assumes that the transport of acetate ions in the bio-film is a result of diffusive flux. The acetate ions are not $\frac{1}{2}$ charged species (effects of potential are neglected) and the convective flux is neglected. The transient differential mass balance equation for any species is given by:

$$\frac{\partial c_{\rm a}}{\partial t} = -\frac{\mathrm{d}N_{\rm a}}{\mathrm{d}x} - r \tag{11}$$

where the right side part represents the flux term and the reaction term.

Following Eq. (9), the transient equation for acetate mass balance in the bio-film is given by:

$$\frac{\mathrm{d}c_{\mathrm{ab}}}{\mathrm{d}t} = D_{\mathrm{A}}^{\mathrm{B}} \frac{\mathrm{d}^{2}c_{\mathrm{ab}}}{\mathrm{d}x^{2}} - k \exp\left(\frac{\alpha_{\mathrm{a}}\eta_{\mathrm{a}}F}{RT}\right) \left(\frac{c_{\mathrm{a}}^{\mathrm{AC}}}{K_{\mathrm{a}} + c_{\mathrm{a}}^{\mathrm{AC}}}\right) c_{\mathrm{x}}$$
(12)

Transport equations for the cathode

The oxygen mass balance in the cathode compartment is given by [1]:

$$\frac{dc_{O_2}}{dt} = \frac{q^{CF}}{A^{CC}} \left(c_{O_2^0} - c_{O_2}^{CC} \right) + D_{O_2} \frac{d^2 c_{O_2}}{dx^2}$$
(13)

The equation for the cell potential is given by [1]:

$$V_{\text{cell}} = E_{\text{cell}} - \eta_{\text{a}} - \eta_{\text{c}} - I_{\text{cell}} R_{\text{cell}}$$

$$\tag{14}$$

In Eq. (12), η_a and η_c are anode and cathode over-potentials and the last term refers to the ohmic loss due to the membrane resistance.

The membrane resistance R_{cell} [8] is given by:

$$R_{\text{cell}} = \frac{T^{\text{M}}}{\sigma} \tag{15}$$

In Eq. (13), $T^{\rm M}$ is the membrane thickness and σ is the ionic conductivity of the membrane. The concentration of the acetate at the anode electrode/membrane interphase and the concentration of the oxygen at the cathode electrode/membrane interphase are assumed to be zero.

Numerical solution

For analysis of different parameters, it is necessary to choose a method that is efficient and provides high convergence. The partial derivatives terms were transformed into algebraic terms using central difference and transient PDE were converted into transient ODE. They were then solved using MATLAB function ODE15s.

Simple 1-D mesh was used and it was made enough fine that convergence is achieved. Optimal node number was calculated on the basis of order of length involved by trial and error.

Results and discussion

Anode compartment length

Figure 2 shows a time variation of the cell current density for different anode compartment lengths varying from 0.1 to 0.025 m. It is seen that the cell current density increases with increasing length of the anode compartment (if the area is kept constant, this indicates an increasing volume of the anode compartment). For a given constant feed, Figure 2 indicates that the length of the anode compartment plays a key role in the performance of the MFC.

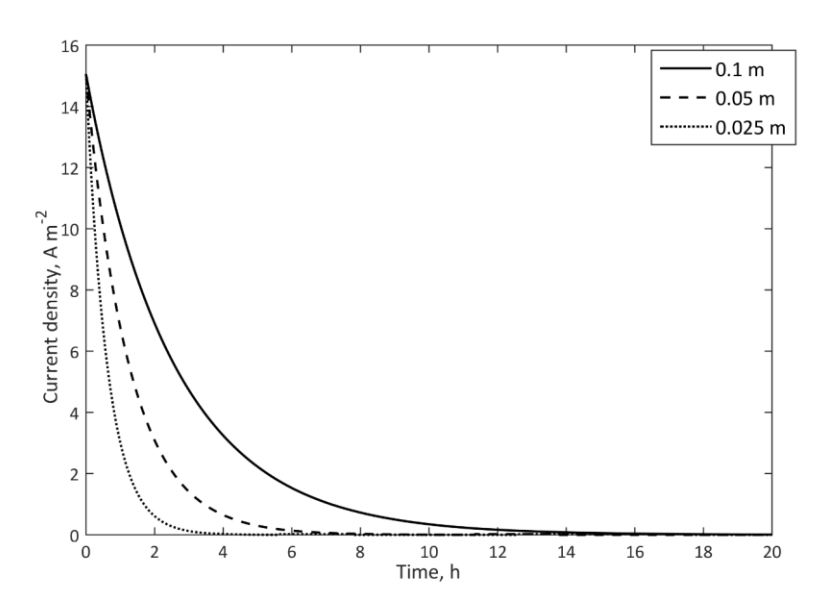


Figure 2. Time variation of current density for different lengths of anode compartment

A higher length of the anode compartment indicates a higher reactor volume which drives the reaction rate. This decreases the activation over-potential, what is seen through the highest current density observed when the anode compartment thickness is 0.1 m. However, a large reactor volume also ensures that the concentration polarization is lower (at high current densities). This implies that when the anode compartment length is higher, presence of the excess reactant ensures that current

can be drawn at extended time values. Lorant *et al.* [19] have studied the effect of the cathode to anode surface ratio on the performance of MFC. The authors predicted that with increasing cathode/anode surface area, the power density of a MFC increases, indicating that the oxygen reduction reaction is the rate limiting step in a MFC. Very little work has been done on understanding the effect of the anode surface area on the overall performance of a MFC. However, our results indicate that the anode surface area plays a significant role in the MFC performance. Table 1 indicates the list of parameters used for simulation.

2.25×10 ⁻⁵ m ³ h ⁻¹
5.5×10 ⁻⁵ m ³
1.56 mol m ⁻³
0.207 mol m ⁻³ h ⁻¹
0.051
303 K
303 K
0.592 mol m ⁻³
0.4 mol m ⁻³
$5 \times 10^{-4} \text{m}^2$
$(0.21 \times P)/(R \times T) \text{ mol m}^{-3}$
1.11×10 ⁻³ m ³ h ⁻¹
0.44
0.77 V
3.6 S m ⁻¹
1.778×10 ⁻⁴ m

Table 1. Table of model parameters taken from [8,10] for simulating graphs in Figures 2-9

Membrane film thickness

Figures 3 and 4 show polarization curves of MFC for different membrane film thicknesses. It can be seen from Figure 3 that the membrane film thickness makes a very small impact on the performance of the fuel cell.

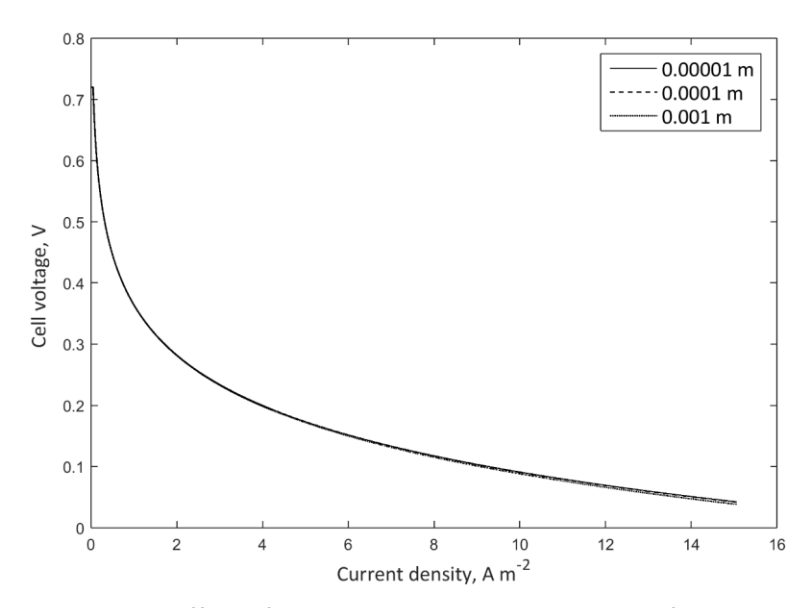


Figure 3. Effect of membrane thickness on MFC performance

Figure 4 shows the effect of the membrane film thickness in the high current density area. It is seen that the membrane film thickness (ohmic resistance) plays a marginal role in the high current density region. The relationship between membrane resistance and membrane thickness is given by

Eq. (13), which shows that the ohmic resistance due to the membrane is defined as the ratio of the thickness of the membrane to the ionic conductivity of the membrane. Figures 3 and 4 indicate that if the ionic conductivity of the membrane is kept constant, the performance of the microbial fuel cell has little dependence on the thickness of the membrane. Consequently, keeping the thickness of the membrane constant, varying the ionic conductivity of the membrane has little effect on the performance of the fuel cell. This indicates that the transport of hydrogen ions through the membrane is more dependent on other factors like concentration flux of hydrogen ions, potential gradient across the cell and the diffusion coefficient of hydrogen ions.

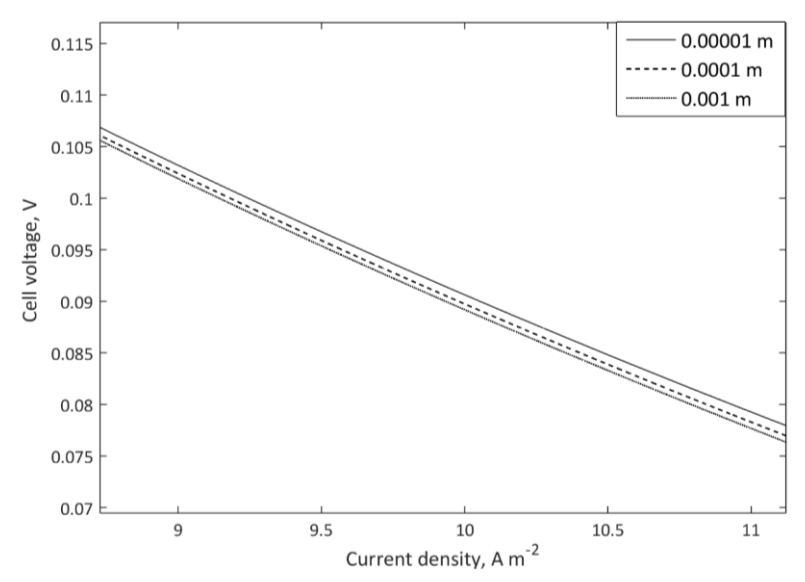


Figure 4. Effect of membrane thickness on MFC performance

Bio-film conductivity

Figure 5 shows the effect of bio-film conductivity on the performance of MFC. The figure indicates that the performance of a microbial fuel cell is affected very strongly by the bio-film conductivity. Whereas no effect of bio-film conductivity is observed on the activation part of the polarization curve, there seems to be a pronounced effect of bio-film conductivity in the high current density region of the polarization curve. Malvankar et al. [20] have suggested that extra cellular electron transfer via conductive bio-film is the most efficient mechanism for high current density MFCs. Increased bio-film conductivity lowers the resistance for electron transfer between the bio-film and the anode. It was also suggested that electron donor mass transfer resistance becomes significant at higher bio-film conductivity. The same authors [20] have further stated that the observed metallic like conductivity is associated with a network of microbial nanowires coursing through the bio-film. Some experimental studies [21-23] have indicated that the bio-film conductivity does not play a major role in affecting the current density in a microbial fuel cell while other studies [20,24] suggested otherwise. An earlier modeling study [13] has indicated that the bio-film conductivity plays a major role in affecting the fuel cell current density. According to Yao et al. [25], the conductivity of the bio-film directly affects a distribution of the solid potential. The authors postulated that the slope of the solid potential of the bio-film decreases with increase in conductivity which causes electrons to move more easily to the electrode surface. On the other hand, the liquid potential is a function of the bio-electrochemical reaction rate and increases with bio-film conductivity. Thus, increasing the bio-film conductivity increases the overall rate of the bioelectrochemical reaction, leading to increase in performance of MFC, particularly in high current density regions.

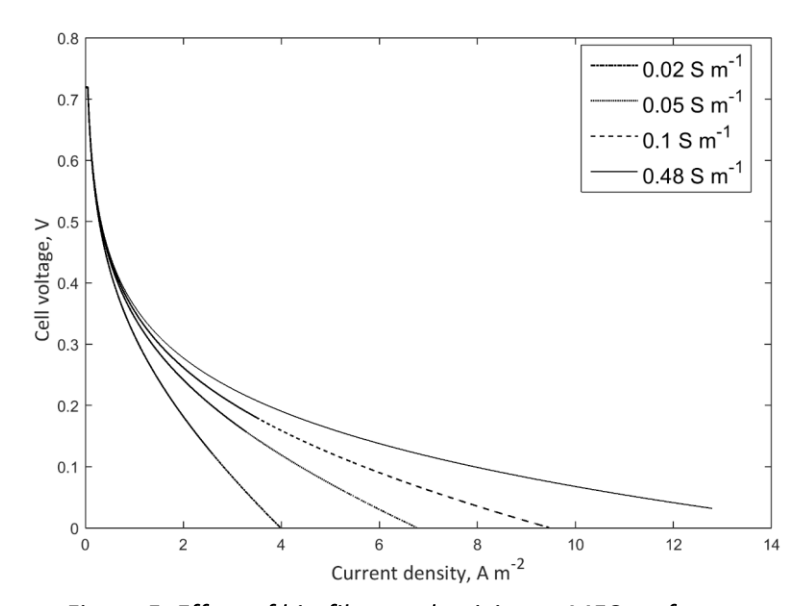


Figure 5. Effect of bio-film conductivity on MFC performance

Effect of temperature

Figure 6 shows that the performance of MFC is affected strongly by temperature. Increasing of temperature not only drives up anodic and cathodic reaction rates, but also increases diffusion of hydrogen ions to the cathode, increasing thus the cathodic reaction rates and leading to significant improvement of MFC performance.

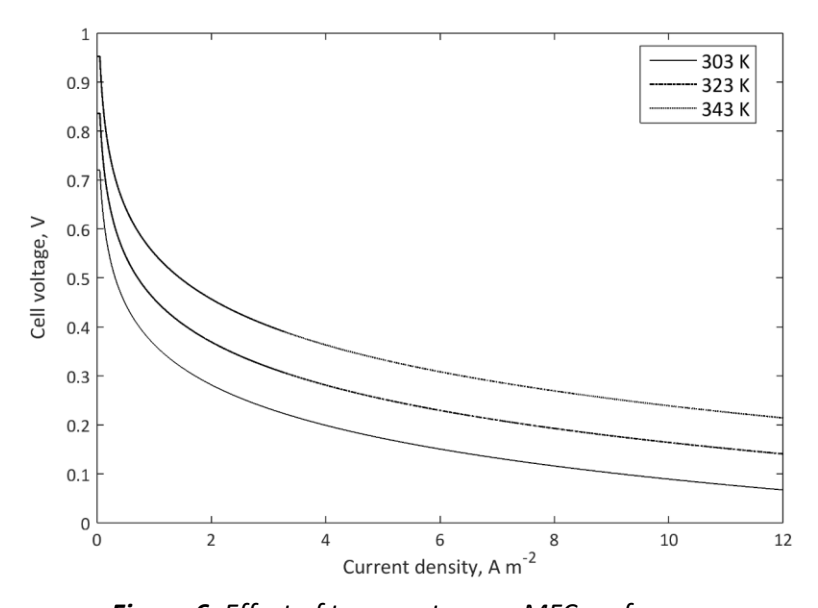


Figure 6. Effect of temperature on MFC performance

It seems that temperature shows somewhat higher impact in the lower current density region where the activation over-potential plays a major role, than in the higher current density region of the polarization curve. This has already been expected, since temperature plays a major role in affecting the rate constant and hence the rate of the reaction. Behera *et al.* [26] postulated that the internal resistance of MFC is the highest when the temperature is at 20 °C, than progressively decreases with increasing temperature up to 40 °C, and does not change much after 40 °C. However, our simulation results indicate that the performance of MFC increases with temperature beyond 40 °C. Since the effect of temperature affects other factors, including reaction rates at the anode and

cathode, it is very difficult to quantify the effect of temperature on the internal resistance of the cell using our simulation model.

Effect of anode surface area

Figure 7 shows the variation of current density for different inlet acetate concentrations, while Figure 8 shows the variation of current density at constant acetate concentration, but different anode surface areas. Combining these two graphs helps us to understand few results.

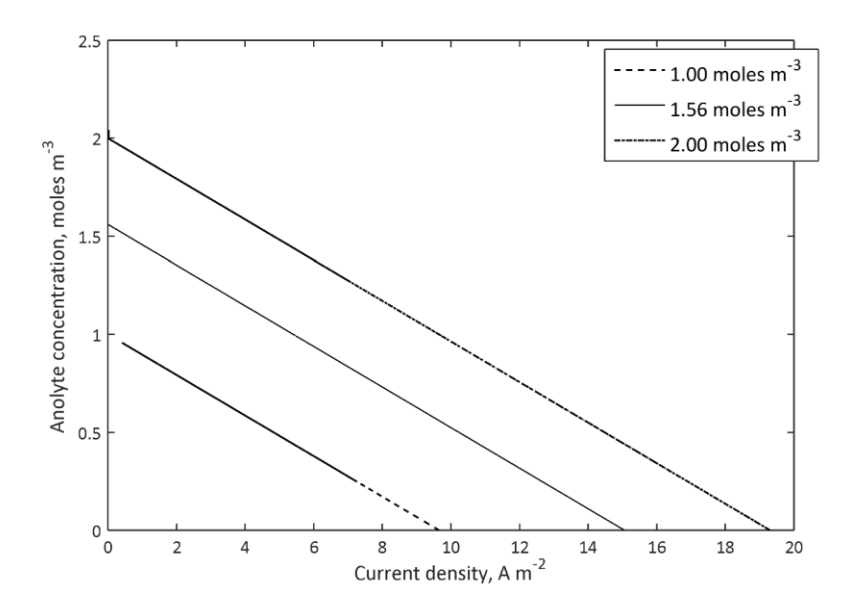


Figure 7. Effect of analyte concentration on MFC performance

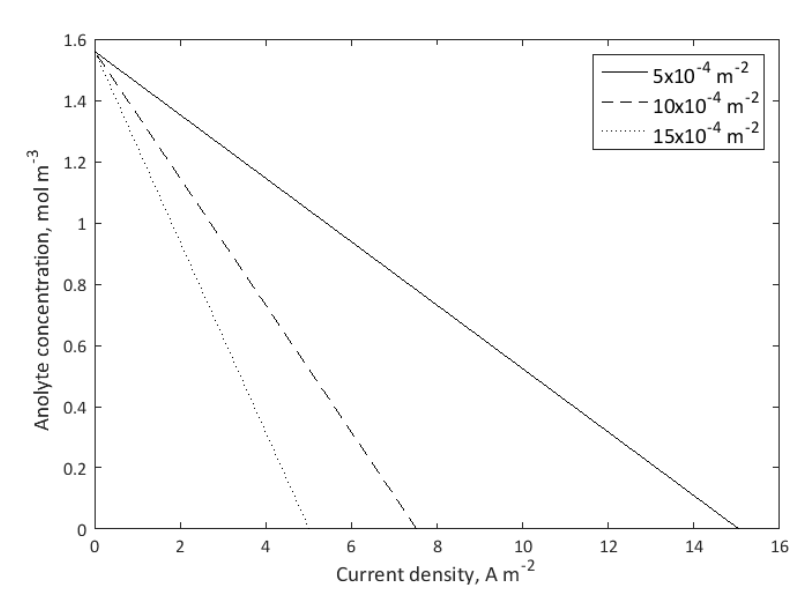


Figure 8. Effect of anode surface area on MFC performance

The inlet acetate concentration plays a significant role in the low current density region. This indicates that the concentration of the acetate plays significant role in lowering the activation overpotential at the anode side (since we are looking at acetate concentration only, the cathodic reaction is not taken into account). Figure 8 shows the variation of current density as a function of anode surface area for the given acetate concentration. The resulting graphs indicate that the area of the anode surface plays a major role in driving the current density in the high current density

region (ohmic and concentration polarization regions). This indicates that a higher anode surface area really enhances the current in the mass transfer limited regions, possibly due to higher reaction rates. Depending on the application of the microbial fuel cell, the fuel cell needs to be designed accordingly. Very little data is available on the effect of acetate concentration on the performance of MFC. Lorant *et al.* [19] proposed that efficiency of MFC can be fairly high at lower concentrations of acetate (what means that the power will not deteriorate rapidly at lower concentrations). Our simulation results indicate a similar effect.

Comparison of modeling results with experimental data

Figure 9 shows the comparison of modeling results with experimental data [8,10]. The parameters used for data fitting are summarized in Table 1. The following parameters were considered in simulations: temperature, inlet acetate concentration, anode flow rate, cathode flow rate, volume of the anode compartment and membrane thickness. The simulation results seem to capture experimental trends very well. However, a certain discrepancy between the simulation results and the experimental data can be observed. This could be due to certain assumptions made in the model. The assumption of constant bio-film thickness is one factor which could affect simulation results, as well as neglecting the effect of convection on the performance of MFC. Although the effect of these assumptions could not be quantified, they could definitely affect the performance of a MFC.

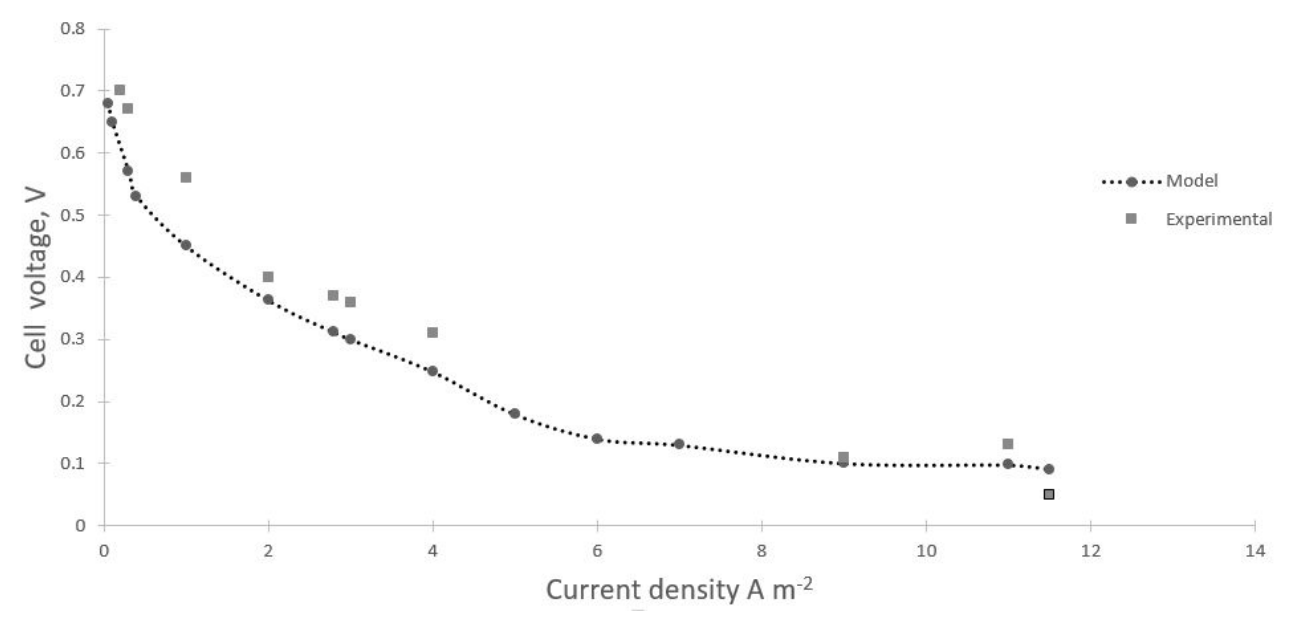


Figure 9. Comparison of simulation results with experimental data

Conclusion

A mathematical model is developed to study effects of operational parameters on the performance of a microbial fuel cell. The effect of thickness of the anode compartment, membrane resistance, bio-film conductivity and inlet concentration of the acetate on the performance of the microbial fuel cell is studied. The membrane thickness and resistance are found to have minimal effect of the MFC performance. However, bio-film conductivity is found to have a significant impact on the polarization curve, particularly in the high current density region. Increasing the area of the anode compartment seems to have a significant impact on the polarization curve in the high current region (mass transport limited region). Model results are compared with experimental data and found to compare well.

Nomenclature

۸.	an ada aan nankaan k
AC	anode compartment
AE	anode electrode
AP	anode acrylic plate
В	bio-film
CC	cathode compartment
CE	cathode electrode
СР	cathode acrylic plate
V_{AC}	volume of the anode compartment, m ³
N _A	flux of acetate in the bio-film layer, mol m ⁻² s ⁻¹
$D_A{}^B$	diffusivity of the acetate in the bio film layer, m ²
A ^{CC}	area of the cathode compartment, m ² s ⁻¹
C a	concentration of acetate in the anode compartment, mol m ⁻³
c_A^0	concentration of acetate at the entrance to the anode compartment, mol m ⁻³
c a ^{AC}	concentration of acetate at the exit of the anode compartment, mol m ⁻³
C ab	concentration of acetate in the bio-film, mol m ⁻³
$c_{a}{}^{AB}$	concentration of acetate at the bio-film/AE interface, mol m ⁻³
<i>c</i> _{O2}	concentration of oxygen in the cathode compartment, mol m ⁻³
$c_{0_2}{}^{0}$	concentration of oxygen at the CP/CC interface, mol m ⁻³
c_{02}^{CC}	concentration of oxygen at the CC/CE interface, mol m ⁻³
C _X	concentration of bio-mass in the anode compartment, mol m ⁻³
F	Faraday constant, 94 485, C mol ⁻¹
K	rate constant of the reaction, mol m ⁻³ h ⁻¹ .
K_{A}	half velocity rate constant for acetate, mol m ⁻³
R	gas constant, 8.314 J mol ⁻¹ K ⁻¹
R_{cell}	cell resistance due to membrane, Ω
T	temperature, Kelvin
V	volume, m ³
V_{cell}	cell voltage, V
T_0	wall temperature on anode side, K
T_{C}	wall temperature on cathode, K
q	flow rate, m ³ h ⁻¹
T_{M}	membrane thickness, m
\mathcal{T}^{AF}	temperature of the anode stream
\mathcal{T}^{CF}	temperature of the cathode stream
A^{s}	surface area of membrane, m ²
Ε	applied potential, V
E_{eq}	standard potential of the redox reaction (V)
$lpha_{a}$	anodic transfer coefficient
$lpha_{c}$	cathodic transfer coefficient
σ	ionic conductivity of membrane, S m ⁻¹
η_{a}	anode overpotential, V
•	

Acknowledgements: We wish to acknowledge BITS Pilani, Hyderabad for their help in publishing this article.



 η_{c}

cathode overpotential, V

References

- [1] X. C. Zhang, A. Halme, *Biotechnology Letters* **17** (1995) 809-814.
- [2] C. Picoreanu, K. Scott, Water Research 41 (2007) 2921-2940.
- [3] A. K. Marcus, C. I. Torres, B. E. Rittmann, *Biotechnology and Bioengineering* **98** (2007) 1171-1182.
- [4] B.V. Merkey, D. L.Chopp, Bulletin of Mathematical Biology 74 (2012) 834-857.
- [5] R. Sedaqatvand, M. M. Mardanpoura, Bioresource Technology 146 (2013) 247-253.
- [6] N. Jayasinghe, R. Madhavan, BioTechnology Journal 10 (2014) 1350-1361.
- [7] R. P. Pinto, B. Srinivasan, M. F Maneul, B. Tattarskosky, *Bioresource Technology* **101** (2010) 5256-5265.
- [8] V. B. Oliviera, M. Simoes, L. F. Melo, A. M. F. R. Pinto, *Energy* **61** (2013) 463-471.
- [9] S. Cheng, B. Wang, Y. Wang, *Bioresource Technology* **147** (2013) 332-337.
- [10] Y. Zeng, Y. F. Choo, B. H. Kim, P. Wu, Journal of Power Sources 195 (2010) 79-89.
- [11] W. Cai, Hong Liu, Chemical Engineering Journal **333** (2018) 672-582.
- [12] M.M.Mardanpour, S.Yaghmaei, M.Kalantar, *Journal of Power Sources* **342** (2017) 1017-1031.
- [13] S. Ou, M. M. Mench, Journal of Power Sources **314** (2016) 49-57.
- [14] P. Sobieszuk, A. Jaraszewicz, L. Makowski, *Journal of Power Sources* **371** (2017) 178-187.
- [15] S. Yao, X. Y. Li, *Electrochimica Acta* **212** (2016) 201-211.
- [16] C. Xia, D. Zhang, W. Pedrycz, Y. Zhu, Y. Gao, *Journal of Power Sources* **373** (2018) 119-131.
- [17] S.Gadkari, S. Gu, J. Sadhukhan, *Chemical Engineering Journal* **343** (2018) 303-316.
- [18] A. Capadaglio, D. Cecconet, D. Molognoni, *Processes* **5 (4)** (2017) 73-78.
- [19] B. Lorant, M.Loka, G. M.Tardy, Energy (IYCE), (2015) 1-7.
- [20] N. Malvankar, M. Tuominen, D. Lovely, *Energy and Environmental Science* **5** (2012) 5790-5796.
- [21] H. Richter, L. M. Tender, Energy and Environmental Science 2 (2009) 506-516.
- [22] C. I. Torres, A. K. Marcus, P. Parameswaran, B. E. Rittmann *Environmental Science and Technology* **42** (2008) 6593-6597.
- [23] Y. Liu, H. Kim, R. Franklin, D. R. Bond, Energy and Environmental Science 3 (2010) 1782-1788.
- [24] D. Pocaznoi, B. Erable, M.-L. Delia, A. Bergel, Energy and Environmental Science 5 (2012) 5287-5296.
- [25] S. Yao, L. He, B. Song, Y. Li, *Electrochimica Acta* **212** (2016) 201-211.
- [26] M. Behrera, P.S.Jana, M. M. Ghangrekar, Bioresource Technology 101 (2010) 1183-1189.